

NASA
Technical Paper 1628

AVRADCO
Technical Report 79-40

LOAN COPY: RETU
AFWL TECHNICAL
KIRTLAND AFB,



An Experimental Investigation of Two Large Annular Diffusers With Swirling and Distorted Inflow

William T. Eckert, James P. Johnston, Tad D. Simons,
Kenneth W. Mort, and V. Robert Page

FEBRUARY 1980

NASA





NASA
Technical Paper 1628

AVRADCOM
Technical Report 79-40

An Experimental Investigation of Two Large Annular Diffusers With Swirling and Distorted Inflow

William T. Eckert
*Aeromechanics Laboratory
AVRADCOM Research and Technology Laboratories
Ames Research Center, Moffett Field, California*

James P. Johnston and Tad D. Simons
*Stanford University
Stanford, California*

Kenneth W. Mort and V. Robert Page
*Ames Research Center
Moffett Field, California*



National Aeronautics
and Space Administration

Scientific and Technical
Information Office

1980

AN EXPERIMENTAL INVESTIGATION OF TWO LARGE ANNULAR DIFFUSERS WITH SWIRLING AND DISTORTED INFLOW

William T. Eckert,* James P. Johnston,† Tad D. Simons,‡
Kenneth W. Mort,‡ and V. Robert Page‡

Two annular diffusers downstream of a nacelle-mounted fan were tested for aerodynamic performance, measured in terms of two static pressure recovery parameters (one near the diffuser exit plane and one about three diameters downstream in the settling duct) in the presence of several inflow conditions. The two diffusers each had an inlet diameter of 1.84 m, an area ratio of 2.3, and an equivalent cone angle of 11.5° , but were distinguished by centerbodies of different lengths. The dependence of diffuser performance on various combinations of swirling, radially distorted, and/or azimuthally distorted inflow was examined. Swirling flow and distortions in the axial velocity profile in the annulus upstream of the diffuser inlet were caused by the intrinsic flow patterns downstream of a fan in a duct and by artificial intensification of the distortions. Azimuthal distortions or defects were generated by the addition of four artificial devices (screens and fences).

Pressure recovery data indicated beneficial effects of both radial distortion (for a limited range of distortion levels) and inflow swirl. Small amounts of azimuthal distortion created by the artificial devices produced only small effects on diffuser performance. A large artificial distortion device was required to produce enough azimuthal flow distortion to significantly degrade the diffuser static pressure recovery.

Because of the complexity of the flow field, the performance characteristics of diffusers with nonuniform inflow conditions are understood qualitatively in some cases but elude accurate, theoretical analysis. More study is needed, and careful testing of diffusers with various inflow conditions (especially swirl) can advance the state of the art (refs. 1 and 2). Recent experimental studies at Ames Research Center have provided additional data on the effects of various inflow characteristics on the aerodynamic performance of two particular diffuser geometries.

The recent NASA effort directed toward repowering and modifying the Ames 40- by 80-Foot Wind Tunnel (refs. 3 and 4) has encompassed many areas of experimental research, development, and optimization. In one study, the performance of the drive fan rotor/stator system and of the diffuser components of the fan nacelle were examined on a 0.15-scale model of the drive system proposed for the modified facility. The tests were conducted over the projected drive-system operating envelope and in the presence of various inflow distortions. The aerodynamic and acoustic results of the fan system portion of the study are summarized in references 5 and 6, respectively.

This report presents the diffuser characteristics resulting from the inflow patterns imposed during the rotor/stator testing. The fan nacelle diffuser was investigated because of its large contribution to the losses in the wind-tunnel circuit. The effects of swirl and distortion on diffuser performance were the primary area of concern in this study.

The following diffuser characteristics are presented for a range of entering flow patterns (radial variations of swirl angle and velocity): (1) the longitudinal variation of wall static pressure coefficient, (2) the distributions of static pressure coefficient and local velocity near the exit plane, and (3) the diffuser performance results expressed as the static pressure recovery coefficient, both near the exit plane and near the end of the downstream settling duct.

Data were collected at Reynolds numbers ranging from 0.7×10^6 to 2.6×10^6 . (Reynolds numbers were based on the 0.463-m (1.52-ft) annulus gap and on the mean flow speed at the diffuser inlet.) The entering flows (as measured at the survey station) included swirl angles between 0° and 14° , and effective area fractions that varied from case to case between 0.78 and 0.96. The azimuthal distortion, measured in terms of the ratio of local-radial-average and cross-sectional mean velocities, ranged from about 0.78 to 1.12.

The authors acknowledge the valuable assistance of Mr. Daniel J. Clasen of ARO, Inc., Ames Division, for his careful supervision of the model operation and data acquisition.

*Aeromechanics Laboratory, AVRADCOM Research and Technology Laboratories, Moffett Field, Calif. 94035.

†Mechanical Engineering Dept., Stanford University, Stanford, Calif. 94305.

‡NASA Ames Research Center, Moffett Field, Calif. 94035.

NOTATION

A	diffuser flow cross-section area, m^2 (ft^2)	V	axial flow velocity, m/sec (ft/sec)
AR	diffuser area ratio, $\frac{A_2}{A_1}$	VM	mean velocity in cross section near diffuser exit plane, m/sec (ft/sec)
C_p, CP	surface static pressure coefficient referenced to average static pressure near diffuser inlet and made dimensionless by mean dynamic pressure near diffuser inlet, $\frac{P - P_{ref}}{q_{1m}}$	w_s	local width of diffuser shell, m (ft)
D_s	inside diameter of annulus shell, m (ft)	X	centerline distance downstream from diffuser entrance, m (ft)
dA	element of diffuser cross-section area, m^2 (ft^2)	β	swirl angle of flow upstream of diffuser entrance, measured from duct centerline, deg
E	effective area fraction at the survey station and azimuth (a measure of flow radial uniformity), $\frac{V_a}{V_{max}}$	$\bar{\beta}_a$	average value of β_a for all survey azimuths at specified conditions, deg
\bar{E}	average value of E for all survey azimuths at specified conditions	δ	uncertainty in magnitude of parameter
H_s	local vertical height of diffuser shell, m (ft)	η_D	diffuser efficiency, $100 \frac{P_2 - P_1}{q_{1m}[1 - (1/AR^2)]}$, percent
L	centerline length of diffuser duct, m (ft)	θ	azimuthal angle locating the wall static pressure taps in the local cross section 0.3 m (1.0 ft) downstream of the diffuser exit, measured from vertical duct centerline (zero angle straight up), positive clockwise looking upstream, deg
\dot{m}	rate of mass flow through the duct, percent of design value	ξ	fan stagger angle, angle between duct centerline and blade chord line (complement of blade angle), measured at 3/4 radius, deg
P	local surface static pressure, N/m^2 (lb/ft^2)		
q	dynamic pressure of axial flow, $\frac{\rho V^2}{2}$, N/m^2 (lb/ft^2)	ρ	airflow density, kg/m^3 ($slugs/ft^3$)
$R_{c/b}$	maximum radius of diffuser centerbody, m (ft)	Subscripts	
R/RS	radial distance from centerline of annular duct, fraction of outer shell radius	a	mass-weighted average value of parameter at survey azimuth (see Glossary)
$r_{c/b}$	local radius of diffuser centerbody, m (ft)	e	area-weighted average value of parameter for conditions measured 0.3 m (1.0 ft) downstream of diffuser exit
r_s	local radius of corner fillet in diffuser, m (ft)	$i, 1-D$	ideal, one-dimensional flow

<i>m</i>	mean value of parameter from continuity considerations (see Glossary)
max	maximum value of parameter
ref	reference value of parameter, taken near diffuser inlet
<i>SD</i>	average condition measured near downstream end of settling duct, approximately three hydraulic diameters downstream of diffuser exit
theo max	theoretical maximum
1	condition at diffuser inlet plane
2	condition at diffuser exit plane
2θ	diffusion angle or equivalent cone angle, deg

MODEL CONFIGURATIONS

LUL	<u>L</u> ong (1.17 D_s) upstream contraction section, <u>U</u> niform annulus centerbody diameter, and <u>L</u> ong diffuser centerbody
LVL	<u>L</u> ong (1.17 D_s) upstream contraction section, <u>V</u> arying annulus centerbody diameter, and <u>L</u> ong diffuser centerbody
LVS	<u>L</u> ong (1.17 D_s) upstream contraction section, <u>V</u> arying annulus centerbody diameter, and <u>S</u> hort diffuser centerbody
SUL	<u>S</u> hort (0.67 D_s) upstream contraction section, <u>U</u> niform annulus centerbody diameter, and <u>L</u> ong diffuser centerbody

GLOSSARY

average:	mass-weighted average value of parameter calculated from the survey measurements at local azimuth
azimuthal distortion:	variation of local azimuth average velocity from mean velocity at duct station (quantified by V_a/V_m)

equivalent cone angle: included wall angle of a right cone with same inlet and exit areas,

$$2 \tan^{-1} \frac{\sqrt{A_2} - \sqrt{A_1}}{L\sqrt{\pi}}$$

first stall limit: condition vaguely dividing the regimes of steady, uniform, unstalled flow and unsteady, nonuniform flow with significant transitory stall (see ref. 1)

hydraulic diameter: $\frac{4 \text{ (flow area)}}{\text{outer perimeter}}$

mean: overall mean value at local cross section as calculated by continuity considerations from flow conditions at inlet of test apparatus (in metering station)

peak recovery: maximum static pressure recovery achieved as area ratio is varied at a constant ratio of axial length to inlet width (shown as the C_p^* line in fig. 15 of ref. 1); generally obtained when flow separation (stall) starts to occur as area ratio is increased

radial distortion: deviation from rectilinear uniformity of the radial profile of velocity at a given survey azimuth (quantified by $E = \frac{V_a}{V_{\max}}$)

static pressure recovery: rise in static pressure produced by diffusion process, $P_2 - P_1$, or $P_{SD} - P_1$, N/m² (lb/ft²)

station: longitudinal position in duct

MODEL AND APPARATUS

The overall configuration of the test apparatus is shown in figure 1. Figures 2 through 6 and tables 1 through 5 present additional details of the geometry and of the instrumentation locations.

Upstream Ducting

The ducting upstream of the diffuser, as shown in figure 1(c), consists of three parts: (1) an inlet bell-mouth and constant-area, square inlet duct, (2) a

contraction with shape transition from the inlet duct to the annulus, and (3) an annular duct containing the fan rotor/stator system, drive motor, centerbody, and support struts. The basic (i.e., "reference") aerodynamic design parameters of the drive fan system are summarized in table 1.

Figure 2(a) shows a portion of the inlet duct and the contraction sections. Two contraction duct lengths were tested: the short contraction was 0.67 throat diameters in length and the longer one was 1.17 diameters long; both had a contraction ratio of 1.68 and provided a linear variation of fillet radius from the square cross section of the inlet duct to the circular cross section. Figure 2(a) also shows the placement of the various distortion-generating devices described further in figure 2(b).

Figures 3(a) and 4(a) present the details of the nacelle annulus, including the survey location where swirl and velocity distributions and area-fraction data were measured. Figures 3(b) and 4(b) show the duct cross section at the survey location and the four azimuth positions (top, starboard, bottom, and port) around the duct where the radial surveys were made. Additional geometry, including details of the annulus and motor support struts, are given in table 2.

Diffusers

Two annular diffuser duct geometries were obtained by using the fixed outer shell with two different centerbodies.

The annular diffusers were preceded upstream by the constant-diameter annulus which had a length of 1.7 outer diameters. The diffuser shell cross-sectional shape changed uniformly (i.e., a linear variation of corner fillet radius) over the length from circular at the inlet to rectangular at the exit. The height-to-width ratio at the exit was about 1.1. (The geometry is shown in side view and in cross section in figure 5 with additional details in table 3.)

The two diffuser centerbodies were different primarily in their length (i.e., fineness ratio). Both centerbodies (with coordinates given in table 4) tapered gradually from maximum diameter at the diffuser inlet to terminate at zero diameter. The long centerbody extended to just downstream of the diffuser exit, while the short tail cone extended for only about 70% of the diffuser length. The area distributions through the two diffusers are given in table 5. The overall equivalent cone angle of 11.5° and

the overall area ratio of 2.3 were the same for both diffuser systems.

Downstream Ducting

Downstream of the diffuser exit was a constant-area, rectangular "tail pipe" or settling duct (fig. 1(c)) with a length of approximately three hydraulic diameters of the diffuser exit. For all configurations, the flow rate through the model was controlled by a pair of common-hinged doors forming a throttle wedge (shown in fig. 1(b)) at the end of the settling duct in the final exit from the test rig.

Instrumentation

All calculations and results were based on temperature and pressure data, taken as required. Temperature measurements were made with five thermocouple probes located at the test rig inlet face and three more probes midway through the constant-diameter annulus. The inlet thermocouple probes were located one at the center of each lip of the bellmouth and one on the flow centerline. The annulus thermocouple probes were located at the $3/4$ radius position, approximately evenly distributed around the cross section at a station just upstream of the motor support struts.

The pertinent pressure-measuring locations are shown in figures 1(c), 3, 4, and 5(a). There were five pressure data systems used: (1) surface pressure orifices around the inlet duct measured the mass flow, \dot{m} , through the calibrated bellmouth (fig. 1(c)); (2) a traversing, six-port survey probe (fig. 6), used at any of four azimuth positions (figs. 3(b) and 4(b)) in the annulus upstream of the diffuser inlet, measured swirl- and velocity-related parameters; (3) surface pressure orifices on the centerbodies and diffuser shell walls (shown schematically in fig. 1(c) and in detail in figs. 3(a), 4(a), and 5(a)) measured static pressure coefficient information; (4) total pressure rakes and static pressure surface orifices just downstream of the diffuser exit (located as shown in figs. 1(c) and 5(a)) were distributed to give equal-area measurements of the pressures and velocities near the diffuser exit plane; and (5) surface pressure orifices on the walls of the settling duct measured additional static pressure recovery information.

REDUCTION OF DATA

Data Sources and Handling

The diffuser performance parameters were determined from different sources in a variety of ways. The inflow swirl angle and velocity distributions were determined from the survey probe data taken at several discrete points across the annulus. The dynamic pressures and velocities at the diffuser inlet were mean values based on measurements taken near the calibrated bellmouth inlet, adjusted for area differences. The discrete local and mass-weighted-average velocities at the survey station were computed from total and static pressure measurements. Static pressure coefficients, based on data from wall static pressure taps, were referenced to the static pressure at the diffuser inlet (an interpolated value because no measurement was taken at exactly that location), and were made dimensionless by the mean dynamic pressure entering the diffuser.

Calibration and Accuracies

The flow through the inlet bellmouth was calibrated on a 0.305 m (1.0 ft) square scale model. The calibration was conducted using a precalibrated, standard ASME long-radius flow nozzle. The calibrated mass flow of the inlet was based on the static pressure drop at the throat and the temperature at the entrance. (All data presented here were taken above the critical Reynolds number of the bellmouth.)

The survey probe (fig. 6) was calibrated in the Ames 7- by 10-Foot Wind Tunnel (Number 1). The pressures were calibrated in terms of dimensionless pressure differences measured by the six-port, directional pitot-static probe. Total and static pressures were calibrated against a known standard. The flow angle was determined from an inclinometer for upright and inverted probe calibration runs. During testing operation, measured quantities were adjusted, using the calibrations, for angularity effects to give corrected values. (The radial flow angles were calibrated and measured but were small and are not reported.)

All pressure readings used to determine the calibrations and the various flow parameters were accurate to about ± 0.75 mm (± 0.03 in.) of vertical water column height. The survey probe installation errors did not exceed $\pm 0.5^\circ$. The effects of calibration, installation, and other errors and uncertainties for

the annulus flow data, determined by the methods of reference 7, are presented in figure 7(a) as functions of swirl angle. Figure 7(b) shows the uncertainties in the results of the static pressure coefficients and the diffuser exhaust velocity distributions.

The position of the survey probe was known to within about ± 3 mm (0.1 in.) or about $\pm 0.3\%$ of the shell radius ($\delta R/RS = 0.003$). The other pressure port locations were accurate to about ± 6 mm (± 0.3 in.).

Temperature measurements were made within $\pm 1.1^\circ\text{C}$ ($\pm 2^\circ\text{F}$) and the fan speed settings were accurate to about 2 rpm, or less than 0.2% of the nominal (design) value. The mass-flow rate was accurate to within 1% of the design value (see table 1).

TEST PROCEDURE

The 1.83-meter-diameter, low-speed fan used for the studies of references 5 and 6 was used as the generating device for the diffuser inflow conditions for this study. The fan system design conditions used as the "reference" here and in references 5 and 6 are those given in table 1. (These conditions were derived from the 300-knot maximum flow-speed design point for the high-speed test section of the modified Ames 40- by 80-Foot Wind Tunnel (refs. 3 and 4).)

The swirl imparted to the flow by the rotor/stator system varied with mass flow as did the radial uniformity of the velocity profile. (The swirl and uniformity effects were coupled and changed together as a result of fan loading.)

The mass flow, which controlled the swirl and uniformity, was in turn controlled by the throttle at the duct exit. All data were taken at the same fan rotational speed. Additional distortion was provided by the installation of upstream boundary-layer thickening devices.

The various condition parameters (mass-flow rate, inflow swirl angle, profile uniformity, and blockage) were held constant while data were taken by the survey probe at 10 to 20 discrete radial locations in a single azimuthal quadrant downstream of the stators. The survey apparatus was then moved to another azimuth position and the process repeated.

The model was configured in four selected combinations of six components. (The abbreviations used for the four configurations (LUL, LVL, LVS, and SUL) tested are defined at the end of the Notation section.) The components were a long or short contraction section, a uniform or varying annulus center-

body diameter, and a long or short diffuser centerbody. Each configuration was studied over a range of test conditions (fan stagger angle and/or amount of artificial distortion). Table 6 shows the configurations and test conditions used.

Most data were taken with the long contraction and long diffuser centerbody installed. However, these two components were changed for some tests to determine the effects of upstream duct geometry and of a second diffuser geometry. (When the diffuser centerbody was changed, the upstream annulus centerbody geometry was also changed (see fig. 4(a)).)

Two duct geometries were used as baselines for the various comparisons made. The configurations with the long contraction (fig. 2(a)), uniform annulus centerbody (fig. 3(a)), and long diffuser centerbody (fig. 5), designated LUL, were used as the reference for comparisons showing the effects of contraction length and azimuthal distortion. They were also used to show general diffuser performance trends and characteristics in the presence of swirling and/or radially distorted inflow. The same configuration, but with the varying-diameter annulus centerbody (fig. 4(a)) and designated LVL, was used as the baseline for showing the effects of diffuser centerbody length.

The inflow Reynolds numbers (based on annulus gap and mean flow speed at the diffuser inlet) varied from 0.7×10^6 to 2.6×10^6 , and swirl angles in the annulus ranged between 0° and 14° . As mass flow rate changed, the uniformity of the velocity profile, measured by effective area fraction, varied (not independent of swirl angle) from about 0.78 to about 0.96 because of the change in fan loading. The artificially generated inflow distortion varied from none ($V_a/V_m = 1.0$) to significant ($V_a/V_m = 0.78$ and 1.12) amounts.

The studies considered only steady-state diffuser performance characteristics. No attempt was made to determine the effects of gusts or oscillatory flows.

RESULTS

Annulus flow patterns upstream of the diffuser inlet and diffuser performance results are presented in figures 8 through 33, which are in turn indexed by configuration in table 6.

Configurations With Uniform Annulus Centerbody

Details of the experimental annulus flow distributions (without artificial azimuthal distortion) for the

LUL configuration are presented graphically in figures 8 and 9. The averaged inflow parameters based on these and similar additional data are summarized in figure 10. The corresponding duct wall static pressure distributions are plotted in figure 11. The cross-sectional distributions near the diffuser exit plane of exhaust velocity and pressure coefficient are shown in figures 12 and 13, respectively. The diffuser performance parameters are summarized in figure 14. Data summaries for the same configuration, but with the short contraction (configuration SUL), are presented in figure 15 for the annulus flow and in figure 16 for the diffuser performance.

The annulus flow patterns generated by the four distortion devices operating on the same LUL duct geometry are shown in figures 17 and 18. The resulting longitudinal distributions of wall pressure are given in figure 19. The related diffuser exhaust velocity distributions and pressure recovery data are plotted in figures 20 and 21, respectively.

Configurations With Varying Annulus Centerbody Diameter

The basic annulus flow data for the LVL configuration are shown in figures 22 and 23 and are summarized in figure 24. The longitudinal distributions of wall pressure are given in figure 25. Figures 26 and 27 show the cross-sectional distributions near the diffuser exit plane of the velocity and the wall pressure. The diffuser performance parameters are summarized in figure 28.

Summaries of the annulus flow data for the same configurations except with the short diffuser centerbody, configuration LVS, are presented in figure 29. The longitudinal distributions of wall pressure coefficient and the cross-sectional distributions (near the exhaust) of velocity and wall pressure coefficient are given in figures 30, 31 and 32, respectively. Figure 33 summarizes the resulting performance parameters.

ANALYSIS AND DISCUSSION

The major effects and trends which may be derived from these data are presented in figures 34 through 42. Table 7 provides an index to these figures.

Effect of Contraction Length

The effect of the contraction length on the diffuser inflow is shown in figure 34. The average swirl angle (fig. 34(a)) was virtually the same, through the range of mass-flow rate, for both contractions. However, the velocity profile, as measured by the average effective area fraction (fig. 34(b)), was more uniform for the longer, more gradual contraction. At the same time, the static pressure recovery near the exit plane (fig. 35(a)) was slightly better (i.e., higher) with the long contraction. However, in spite of this difference in the immediate pressure recovery, there was no significant change in the static pressure recovery downstream in the settling duct (fig. 35(b)).

General Diffuser Performance

The contraction effects data of figures 34 and 35 indicate that, for a given swirl angle, a more radially uniform entering flow produces a greater pressure recovery. This trend agrees in general with conclusions that may be deduced from some results found in the literature (e.g., see refs. 9–17, and fig. 36, derived from fig. 2 of ref. 13). However, the present results and those of Sovran and Klomp (ref. 1) plotted in figure 37 indicate there are limitations on this conclusion.

In particular, figure 37 shows two features of special interest: (1) the double-valued nature of the E versus C_{p_e} “parabola” with an apparent minimum around $\bar{E} = 0.92$ and (2) the shift in magnitude of C_{p_e} for the current data from that of Sovran and Klomp (ref. 1). The first aspect implies that, for a range of \bar{E} values below about 0.92, more radial distortion (lower \bar{E}) can give higher pressure recovery. The second aspect implies a lack of correlation between current and previous results. Both of these topics are discussed in appendix A; the conclusions and explanations are reasonably simple.

A parabolic or double-valued form of the E - C_{p_e} curve has not been generally described previously, despite the trend of the Sovran-Klomp data as shown in figure 37 and the trends shown in figure 34(a) of reference 18. However, depending on the nature of the velocity profile, the trend is real. Greater irregularity, more rapid variation across the duct, and certain defect locations cause decreases, even severe

decreases, in pressure recovery as shown in reference 13. But with “well-behaved” profiles as reported here and by other authors, the E - C_{p_e} curve can be double-valued with a real minimum. The shift in the E versus C_{p_e} curve, as discussed in appendix A, could have been the result of the mixing effect of the large-scale turbulence created at the diffuser inlet by the two large motor-support struts.

The general performance of the present diffuser, then, correlates with data of other authors and, in fact, extends and clarifies previous results.

Effects of Inlet Radial Distortion and Swirl Angle

The correlated data from the current test, showing the effects of swirl on the E versus C_{p_e} curve, are plotted in figure 37. The envelope of the curves for various constant $\bar{\beta}_a$ values generally follows the shape of the $\beta_a = 0$ curve. Figure 38 shows the effects of E on the β_a versus C_{p_e} curve in a different cross plot.

The trends and results shown for the static pressure recovery in figures 37 and 38 can be summarized into two major points. First, for the current LUL geometry and inflow patterns, the data suggest that two levels of distortion can produce the same static pressure recovery and that a minimum recovery occurs at about $\bar{E} = 0.92$. Second, at a constant distortion level, a minimum pressure recovery is suggested at about 5° of swirl. While additional recovery is limited, in the lower-swirl direction to zero swirl the limit in the higher direction was not attained but seemed to be greater than the value reached. References 2 and 9 support a trend showing that more swirl holds the greater potential for better diffuser performance. However, caution must be exercised in the use of swirl for increased diffuser performance.

Even though swirl has been shown to be advantageous in this study as in references 2 and 9, care must be exercised in the use of swirl in fan diffuser applications. Some residual swirl may (and probably will) remain downstream of the diffuser exit for cases of swirling flows at the inlet. Persisting swirl could cause unwanted flow distortions and poor flow quality in downstream components — especially critical in closed-circuit, wind-tunnel applications where turning vanes and honeycombs may not entirely remove the residual swirl before the flow reaches the test section. In addition, leaving residual swirl at a fan discharge means a loss in net axial fan thrust and

thus a loss in efficiency. Inevitably, some energy must be diverted and held in the swirling flow.

Effects of Distortion Devices

Figure 39 summarizes the effects of the four floor-mounted artificial distortion devices on the diffuser inflow characteristics. The data points for distortion types A and B are clustered around the curve for "undistorted" inflow, indicating negligible effects on inflow from these two devices. Distortion C produced somewhat more swirl at a given flow rate (as seen in fig. 39(a)), but no measurable differences in velocity profile uniformity for the limited data obtained (see fig. 39(b)). In contrast, distortion device D produced a significant variation in swirl and radial distortion between the two azimuth positions studied, indicating large azimuthal distortion.

The diffuser performance resulting from the four artificially distorted inflows is shown in figure 40. As expected, devices A and B produced only a small change in performance, suggesting a qualitative limit on azimuthal distortion without significant penalty. The type C device caused about a 3.8% reduction in static pressure recovery, but type D, the most severe azimuthal distortion, produced a decrease in static pressure recovery of about 6% (fig. 40(a)). This effect for the type D device showed up more dramatically as an 8% decrease in the final, downstream pressure recovery $C_{p_{SD}}$ in figure 40(b).

Pressure Distribution

A theoretical longitudinal distribution of pressure coefficient in the diffuser is presented in figure 41. This distribution was calculated assuming ideal isentropic flow. Figure 41 also shows the pressure coefficient at the diffuser exit as predicted by the relationships given in reference 8. These theoretical estimates are compared to the experimental results for azimuthally undistorted flow (configuration LUL).

From these curves, three results are clear. First, as is common, the experimental pressure recovery continued to increase into the downstream settling duct. Second, despite the simplicity of the approach of reference 8, the actual pressure recovery was predicted reasonably well. (The diffuser loss calculation approach of reference 8 was based on a collection of data from widely varying diffuser geometries which was reduced to a single, simple analysis technique.)

Third, some experimental results (e.g., as indicated in fig. 14(a)) show pressure recoveries greater than 0.8 for ideal incompressible flow.

The proper explanation of the latter result is discussed in detail in appendix B. The cause of the apparent "extra" pressure recovery is centered in the reference parameter chosen for the recovery coefficient and in the kinetic energy factor. This observation of C_p values greater than calculated for one-dimensional ideal flow is rare, but theoretically possible for nonuniform inflow conditions, as suggested in reference 1.

Effect of Diffuser Centerbody Length

Although the two diffusers with different centerbodies had the same overall diffusion angle and area ratio, the rate of diffusion in the upstream portion of the system was naturally greater with the short centerbody. The effects of this on performance are presented in figure 42. The parameters of exit and downstream (settling duct) static pressure recovery coefficients both show that the short centerbody significantly degraded performance, almost certainly because of the increased severity of flow separation in the more rapidly diffusing geometry. The full-length centerbody, with its more gradual area variation, gave the best performance.

CONCLUSIONS

Some conclusions about diffuser performance may be drawn concerning (1) the importance of upstream duct geometry, (2) the effects of azimuthally undistorted but radially nonuniform and swirling inflows, (3) the performance penalties for azimuthal flow distortions, and (4) the importance and effects of centerbody geometry.

It is clear that the geometry of the contraction used ahead of a fan and nacelle diffuser is important. The contraction geometry can affect the fan inflow, the resulting fan discharge flow, and therefore the diffuser inflow and performance. The results of this study show that, while the final performance level (as measured by the downstream (settling duct) static pressure recovery) may not be appreciably affected, the immediate pressure recovery at the diffuser exit may suffer. A gentle or long contraction duct produces better inflow to the fan than does an abrupt or short contraction. (Although more complex, the con-

traction design suggested in reference 8, one with cubic wall contours, should produce even better inflow than the long linear contraction used in this study.)

Even for azimuthally undistorted diffuser inflow, the rate of change of velocity profile across the annulus apparently can affect the static pressure recovery characteristics. For relatively gradual profile variations and for geometries similar to those reported here, entering radial velocity uniformities (\bar{E} values) near 90% and entering swirl angles less than 5° should be approached cautiously. Minimum performance (minimum static pressure recovery) was suggested at these conditions. Better performance was indicated for the diffuser in this study for the higher swirl angles and for either more or less inflow uniformity. Generally, swirl angles between 10° and 14° produced greater static pressure recovery. Swirl, being easier to achieve than "perfect" flow, may be more effective than area fraction in maximizing pressure recovery. However, for reasons of adverse, secondary downstream effects and "lost" energy, the relative merits of swirl, flow quality, and fan system efficiency must be evaluated for each application.

Artificial devices producing azimuthal distortion had qualitatively predictable effects on diffuser performance: the greater the distortion, the poorer the performance. However, a relatively large solid blockage (covering about 40% of the upstream duct area) was necessary to produce even a 6% decrease in exit static pressure recovery. This decrease was equivalent to an 8% reduction in the ultimate pressure recovery. (As suggested in reference 19, static pressure recovery measured in the downstream settling duct may be a more sensitive and accurate indicator of overall diffuser performance.) Azimuthal distortion tended to cause far more significant penalties in diffuser performance than did radial distortion of comparable magnitude. Maintenance of axial symmetry is important to the performance of annular diffusers.

Even for identical overall diffusion angles and area ratios, the rate of diffusion within the diffuser component affected its overall performance. The long centerbody produced higher static pressure recovery than the short one. Gradual diffusion (i.e., lower rates of diffusion at the beginning of the component, probably due to suppression of separation), gave better diffuser performance for this geometry.

Ames Research Center

National Aeronautics and Space Administration

Moffett Field, Calif. 94035, August 20, 1979

APPENDIX A

BASIC DIFFUSER PERFORMANCE CHARACTERISTICS

Figure 37 presents current data for the LUL configuration and similar zero-swirl data derived from reference 1 for static pressure recovery, C_{pe} , as a function of inlet effective area fraction \bar{E} . These data imply that: (1) C_{pe} is a double-valued function of \bar{E} with a minimum, for this geometry, at about $\bar{E} = 0.92$ and (2) the present data show uniformly higher levels of pressure recovery than do previous data, regardless of swirl angle.

The first implication raises doubts (as in refs. 9–17) as to whether greater uniformity (higher values of \bar{E}) always produces greater static pressure recovery. The second implication, the shift in C_{pe} levels, concerns whether the current data correlates with previous measurements. Both results are resolvable and contribute to the understanding of diffuser performance.

Static Pressure Recovery and Inflow Distortion

The lower parabolic line in figure 37 shows the effect of \bar{E} on diffusers whose geometries are near the first stall limit where peak values of C_p occur. It is based on the correlation line given in figure 24 of reference 1, derived from experiments on two-dimensional, conical, and annular diffusers without inlet swirl and with very low levels of turbulence at the inlet. (At zero inlet swirl, the geometry of the diffuser tested in this program would be near the peak recovery geometry typical of other annular diffusers as shown by the C_p^* line in fig. 15 of ref. 1).

This parabolic curve shows that, for no entering swirl, the diffuser pressure recovery is a double-valued function of effective area fraction \bar{E} . The pressure recovery coefficient may be improved from its minimum, at about $\bar{E} = 0.92$, by either an increase or a decrease in profile uniformity as expressed by the parameter \bar{E} . Thus, a given pressure recovery, based on the mean upstream dynamic pressure, may be achieved by two inflow distributions (two levels of uniformity) at zero entering swirl angle.

From references 13, 16, and 18, it is clear that the pressure recovery is dependent on the exact nature of the velocity profile, that is, the form, location, or

magnitude of the distortion. Figure 37 confirms that at least two distributions (two values of \bar{E}) can produce the same static pressure recovery. Reference 13 shows that the same value of \bar{E} can give two very different levels of pressure recovery.

Thus it can be inferred from the literature that in figure 37 the increase in C_{pe} as \bar{E} drops below 0.92 must be dependent on profile shape. At a given value of \bar{E} , the pressure recovery was improved in reference 13 (figs. 2 and 3) or not changed in reference 18 (fig. 34(c)) by changes in the profile shape. (In other words, \bar{E} is not a uniquely defining parameter for predicting pressure recovery.) It is therefore reasonable to predict that certain careful or fortuitous selections of the velocity profile will further improve static pressure recovery at the same value of \bar{E} . The data presented in figure 34(a) of reference 18 support this potential and the current data confirm it.

Strut Wakes and Increased Pressure Recovery

Initially, figure 37 may seem to imply disagreement in the magnitude of C_{pe} between the previous results of other authors and the current data. No zero-swirl curve was generated by the data collected in this study. However, if a set of data had been obtained at $\bar{\beta}_a = 0$, it is likely that it would have been observed, when plotted in figure 37, to be 0.05 to 0.03 points in C_{pe} higher than the reference $\bar{\beta}_a = 0^\circ$ curve. There are several reasons for believing this. First, the small shifts between curves of $\bar{\beta}_a \neq 0$ are not consistent with the large drop in C_{pe} to the $\bar{\beta}_a = 0^\circ$ curve. None of the other annular diffuser experiments that used inlet swirl showed discontinuous or sudden changes of the swirl effect between $\bar{\beta}_a = 3^\circ$ and 0° (see refs. 2, 14, and 15). Clearly they showed very small or zero changes in C_{pe} versus $\bar{\beta}_a$ until $\bar{\beta}_a$ exceeded 3° . The second and more physically appealing reason for believing that a “measured” $\bar{\beta}_a = 0$ curve would have to be higher on the graph of figure 37 is the mixing effect of the large-scale turbulence that may have been created at the diffuser inlet by the wakes behind the two large struts supporting the fan motor. The wakes and turbulence thus produced have in other cases been shown experimentally to cause increases in pressure recovery (refs. 16 and 17).

The benefits of wakes at the inlet are more apparent than real since they create a total pressure

loss penalty that must be charged to the overall performance of the diffuser. This penalty will appear far downstream after the mixing is complete, and the mixing loss will probably offset the small gain delivered by an increase in C_{pe} , namely, the estimated boost in C_{pe} by 0.03 to 0.05 points above the $\beta_a = 0$ curve in figure 37.

APPENDIX B

MAXIMUM THEORETICAL PRESSURE RECOVERY

Some current experimental results, such as those in figure 14(a) for configuration LUL, show pressure recoveries greater than 0.8 for ideal, incompressible flow shown in figure 41. The proper explanation of this result is known but often overlooked. The reference static and dynamic pressures, although they possess some uncertainty, do not appear to be sufficiently in error to account for the phenomenon of "extra" pressure recovery. However, the form of the equation for pressure recovery in figure 24 of reference 1 provides an understanding:

$$C_{pe} = \frac{1}{E^2} \left\{ \frac{1 - [(E/E_2)^2/AR^2]}{1 - (1/AR^2)} \right\}$$

Here, E_2 (usually less than \bar{E}) is the effective area fraction at the diffuser exit and AR is the diffuser area ratio. Clearly, the pressure recovery depends on the flow uniformity at each end of the diffuser and depends most strongly on the radial uniformity at the inlet (E). While the theoretical values in figure 41 were derived for uniform inflow ($\bar{E} = 1$), the experimental results arose from flows with greater radial distortion ($\bar{E} < 1$). Since the pressure recovery and the effective area fraction are inversely related as shown in the above equation, the nonuniform experimental inflows could be expected to produce larger indicated values of pressure recovery than the idealized, uniform (one-dimensional) theoretical inflow.

This observation has been demonstrated theoretically in reference 16, where the maximum theoretical pressure recovery of a diffuser with nonuniform inlet profile is larger than the ideal, one-dimensional recovery, $C_{pi,1-D} = 1 - (1/AR^2)$. For incompressible flow,

$$C_{p\text{theo max}} = C_{pi,1-D} + \left[\frac{1}{A_1} \int_{A_1} \left(\frac{V_1}{V_{1m}} \right)^3 dA \right]^{-1}$$

and the inlet kinetic energy factor is greater than unity so that $C_{p\text{theo max}}$ must exceed $C_{pi,1-D}$. As confirmed in reference 1, the actual observation of real C_p values greater than $C_{pi,1-D}$ is rare, but theoretically possible.

REFERENCES

1. Sovran, Gino; and Klomp, Edward D.: Experimentally Determined Optimum Geometries for Rectilinear Diffusers with Rectangular, Conical or Annular Cross-Section. *Fluid Mechanics of Internal Flow*, Gino Sovran, ed., Elsevier Publishing Company, 1967, pp. 270-319.
2. Srinath, T.: An Investigation of the Effects of Swirl on the Flow Regimes and Performance of Annular Diffusers With Equal Inner and Outer Cone Angles. M. S. Thesis, Univ. of Waterloo, Ontario, Canada, 1968.
3. Mort, Kenneth W.; Kelly, Mark W.; and Hickey, David H.: The Rationale and Design Features for the 40- by 80-/80- by 120-Foot Wind Tunnel. AGARD-CP-174, March 1976, pp. 9-1 to 9-5.
4. Mort, K. W.; Soderman, P. T.; and Eckert, W. T.: Improving Large-Scale Testing Capabilities by Modifying the 40- by 80-Foot Wind Tunnel. *J. Aircraft*, vol. 16, no. 8, Aug. 1979, pp. 571-575.
5. Page, V. Robert; Eckert, William T.; and Mort, Kenneth W.: An Aerodynamic Investigation of Two 1.83-Meter-Diameter Fan Systems Designed to Drive a Subsonic Wind Tunnel. NASA TM-73,175, 1977.
6. Soderman, Paul T.; and Page, V. Robert: Acoustic Performance of Two 1.83-Meter-Diameter Fans Designed for a Wind Tunnel Drive System. NASA TP-1008, 1977.
7. Kline, S. J.; and McClintock, F. A.: The Description of Uncertainties in Single Sample Experiments. *Mechanical Engineering*, vol. 75, no. 1, Jan. 1953, pp. 3-8.
8. Eckert, William T.; Mort, Kenneth W.; and Jope, Jean: Aerodynamic Design Guidelines and Computer Program for Estimation of Subsonic Wind Tunnel Performance. NASA TN D-8243, 1976.
9. Wallis, R. A.: *Axial Flow Fans*. Academic Press, 1961.
10. Stevens, S. J.: The Performance of Annular Diffusers. *Proc. Institution Mech. Engrs.*, vol. 182, pt. 3D, 1967-68, pp. 58-70.
11. Stevens, S. J.; and Markland, E.: The Effect of Inlet Conditions on the Performance of Two Annular Diffusers. ASME Paper 68-WA/FE-38, Dec. 1968.
12. Schwartz, Ira R.: Investigations of an Annular Diffuser-Fan Combination Handling Rotating Flow. NACA RM L9B28, 1949.
13. Johnston, I. H.: The Effect of Inlet Conditions on the Flow in Annular Diffusers. *Aero. Research Council Technical Rept.* 16,102, C.P. 178, 1954.
14. Howard, J. H. G.; Henseler, H. J.; and Thorton-Trump, A. B.: Performance and Flow Regimes for Annular Diffusers. ASME Paper 67-WA/FE-21, Nov. 1967.
15. Coladipietro, R.; Sridhar, K.; and Schneider, J. H.: Effects of Inlet Flow Conditions on the Performance of Equiangular Annular Diffusers. CSME Paper 73-84, 1974.
16. Wolf, S.; and Johnston, J. P.: Effects of Non-Uniform Inlet Velocity Profiles on Flow Regimes and Performance in Two-Dimensional Diffusers. *Trans. ASME, J. Basic Engineering*, vol. 91(D), no. 3, 1969, pp. 462-474.
17. Waitman, B. A.; Reneau, L. R.; and Kline, S. J.: Effects of Inlet Conditions on Performance of Two-Dimensional Diffusers. *Trans. ASME, J. Basic Engineering*, vol. 83(D), Sept. 1961, pp. 349-360.
18. Henry, John R.; Wood, Charles C.; and Wilbur, Stafford, W.: Summary of Subsonic-Diffuser Data. NACA RM L56F05, 1956.
19. Cockrell, D. J.; and Markland, E.: A Review of Incompressible Diffuser Flow. *Aircraft Engineering*, vol. 35, no. 10, Oct. 1963, pp. 286-292.

TABLE 1.— FAN DRIVE SYSTEM DESIGN PARAMETERS

System parameters	Design values	
	For configurations with uniform annulus centerbody diameter (see fig. 3)	For configurations with varying annulus centerbody diameter (see fig. 4)
Complete system:		
Hub-to-tip-diameter ratio	0.5	0.4375
Drive power, W (hp)	376.7×10^3 (505)	376.7×10^3 (505)
Total pressure rise (head), m (ft) of air	207.3 (680)	207.3 (680)
Weight flow, N/sec (lb/sec)	1632.5 (367)	1632.5 (367)
Rotor only:		
Number of blades	15	15
At 3/4 radius: Chord, cm (in.)	15.95 (6.28)	15.67 (6.17)
Maximum thickness, cm (in.)	1.60 (0.628)	1.57 (0.617)
Solidity $\left(\frac{\text{chord} \cdot \text{no. of blades}}{\text{circumference}} \right)$	0.554	0.546
Stagger angle, deg	40.8	43.6
Rotational speed (counterclockwise looking upstream), rpm	1200	1200
Tip speed, m/sec (ft/sec)	115 (377)	115 (377)
Stator only:		
Number of blades	23	23
Chord, cm (in.)	11.13 (4.38)	13.44 (5.29)
Maximum thickness, cm (in.)	1.11 (0.438)	1.49 (0.529)
At 3/4 radius:		
Solidity	0.594	0.717
Stagger angle, deg	4.28	8.00

TABLE 2.— ANNULUS GEOMETRY DETAILS

Quantity	Measurements	
	For configurations with uniform centerbody diameter (see fig. 3)	For configurations with varying centerbody diameter (see fig. 4)
Shell diameter, m (ft)	1.84 (6.03)	1.84 (6.03)
Centerbody diameters, m (ft):		
At inlet	.91 (3.00)	.80 (2.61)
At exit	.91 (3.00)	.91 (3.00)
Fan rotor and stator	(see table 1)	
Length, m (ft)	3.1 (10.3)	3.1 (10.3)
Motor support struts:		
Number	2	2
Chord, m (ft)	.91 (3.0)	.91 (3.00)
Maximum thickness, m (ft)	.084 (0.276)	.084 (0.276)
Thickness distribution	(see table below)	
Flow areas, m ² (ft ²):		
At inlet	1.996 (21.489)	2.155 (23.199)
Minimum at stators	1.877 (20.205)	1.977 (21.276)
Minimum at struts	1.918 (20.645)	1.918 (20.645)
At exit	2.001 (21.536)	2.001 (21.536)

Motor support struts	
Distance from leading edge, fraction of chord	Thickness, fraction of chord
0.007	0.018
.014	.026
.025	.034
.0625	.050
.101	.062
.175	.078
.25	.088
.351	.092
.5	.088
.701	.068
.800	.052
.95	.018
1.00	0

TABLE 3.— DIFFUSER GEOMETRY DETAILS

Entrance dimensions:	
Shell diameter, m (ft)	1.84 (6.03)
Centerbody diameter, m (ft)	.91 (2.99)
Hub-to-shell-diameter ratio	.496
Flow area, m ² (ft ²)	2.001 (21.536)
Exit dimensions:	
Shell height, m (ft)	2.21 (7.25)
Shell width, m (ft)	2.08 (6.83)
Long centerbody diameter, m (ft)	.06 (0.20)
Short centerbody diameter, m (ft)	0
Flow area	4.597 (49.486)
Lengths, m (ft):	
Shell	4.08 (13.38)
Long centerbody	4.11 (13.50)
Short centerbody	2.88 (9.45)
Area ratio	2.3
Equivalent cone angles, deg:	
Shell	8.16
Long centerbody	12.64
Short centerbody	17.98
Overall system	11.53

TABLE 4.— DIFFUSER CENTERBODY COORDINATES

Distance from diffuser entrance, fraction of diffuser length	Tail cone radius, fraction of radius at diffuser entrance	
	Long centerbody	Short centerbody
0	1.000	1.000
.05	.999	.966
.10	.997	.933
.15	.992	.899
.20	.983	.865
.25	.973	.830
.30	.960	.793
.35	.944	.754
.40	.925	.713
.45	.904	.665
.50	.878	.610
.55	.846	.542
.60	.810	.454
.625	.789	.398
.65	.772	.334
.675	.749	.252
.70	.728	.105
.706	.725	0
.75	.677	
.80	.617	
.85	.546	
.90	.457	
.925	.406	
.95	.340	
.975	.261	
1.00	.133	
1.01	0	

TABLE 5.— AREA DISTRIBUTIONS IN DIFFUSER

Position, fraction of diffuser length downstream of diffuser entrance	Diffuser areas, fraction of net flow area at diffuser entrance				
	Outer shell	Diffuser with long centerbody		Diffuser with short centerbody	
		Long centerbody blockage area	Net flow area	Short centerbody blockage area	Net flow area
0	1.326	0.326	1.000	0.326	1.000
.05	1.390	.325	1.065	.304	1.086
.10	1.452	.324	1.128	.284	1.168
.15	1.512	.321	1.191	.263	1.249
.20	1.571	.315	1.256	.244	1.327
.25	1.629	.309	1.320	.225	1.404
.30	1.685	.300	1.385	.205	1.480
.35	1.739	.291	1.448	.185	1.554
.40	1.791	.279	1.512	.166	1.625
.45	1.842	.266	1.576	.144	1.698
.50	1.892	.251	1.641	.121	1.771
.55	1.940	.233	1.707	.096	1.844
.60	1.986	.214	1.772	.067	1.919
.625	2.009	.203	1.806	.052	1.957
.65	2.031	.194	1.837	.036	1.995
.675	2.053	.183	1.870	.021	2.032
.70	2.074	.173	1.901	.004	2.070
.706	2.079	.171	1.908	0	2.079
.75	2.115	.149	1.966		2.115
.80	2.155	.124	2.031		2.155
.85	2.194	.097	2.097		2.194
.90	2.230	.068	2.162		2.230
.925	2.248	.054	2.194		2.248
.95	2.266	.038	2.228		2.266
.975	2.283	.022	2.261		2.283
1.00	2.299	.006	2.293		2.299
1.01	2.299	0	2.299		2.299

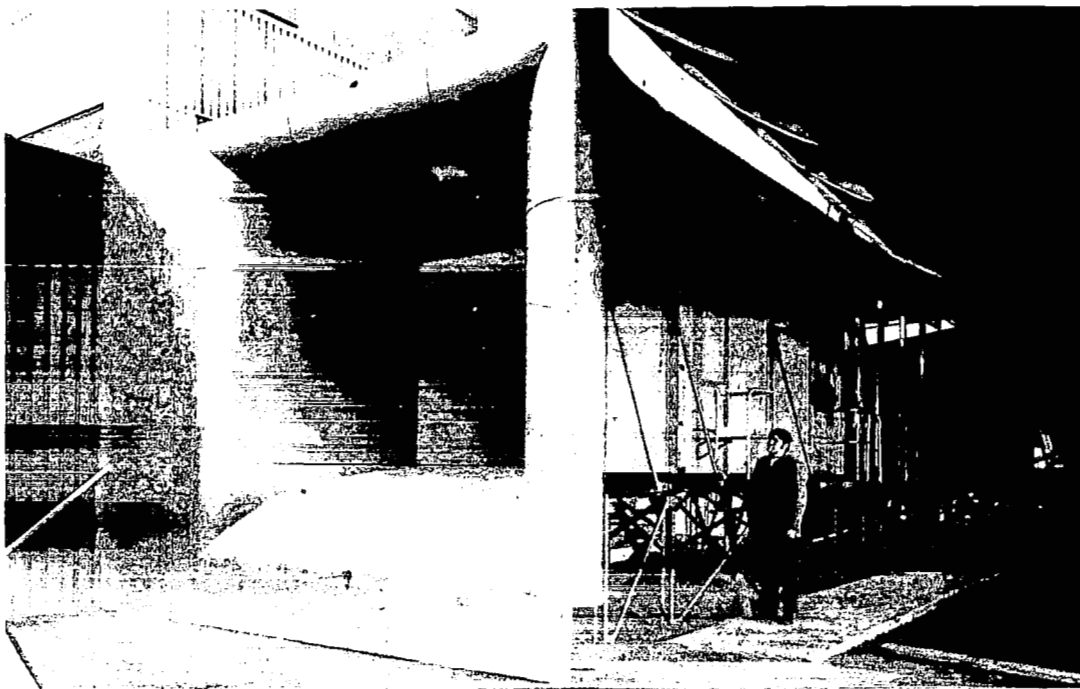
TABLE 6.— INDEX TO BASIC DATA FIGURES

Figure		Configuration				Test condition	
Number	Description	Abbreviation code	Contraction length	Annulus centerbody diameter	Diffuser centerbody length	Artificial distortion devices	ξ , deg
8	Annulus swirl-angle distributions	LUL	Long	Uniform	Long	None	40.8
9	Annulus velocity profiles						40.8
10	Annulus flow summary						Variable
11	Wall static pressure distributions						40.8
12	Velocity distributions at exit						40.8
13	Static pressure distributions at exit						Variable
14	Diffuser performance summary						
15	Annulus flow summary	SUL	Short				
16	Diffuser performance summary	SUL	Short				
17	Annulus swirl-angle distributions	LUL	Long			All	40.8
18	Annulus velocity profiles						
19	Wall static pressure distributions						
20	Velocity distributions at exit						
21	Static pressure distributions at exit						
22	Annulus swirl-angle distributions	LVL		Varying		None	43.2
23	Annulus velocity profiles						43.2
24	Annulus flow summary						Variable
25	Wall static pressure distributions						43.2
26	Velocity distributions at exit						43.2
27	Static pressure distributions at exit						43.2
28	Diffuser performance summary						Variable
29	Annulus flow summary	LVS			Short		43.1
30	Wall static pressure distributions						
31	Velocity distributions at exit						
32	Static pressure distributions at exit						
33	Diffuser performance summary						

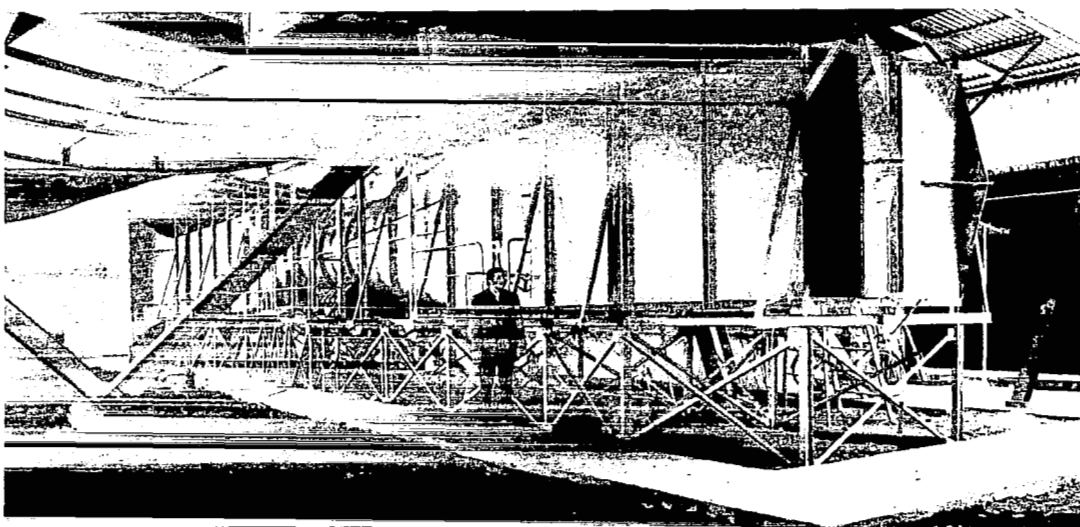
TABLE 7.— INDEX TO COMPARISON AND ANALYSIS FIGURES

Figure		Configuration				Test condition	
Number	Description	Abbreviation code(s)	Contraction length	Annulus centerbody diameter	Diffuser centerbody diameter	Artificial distortion devices	ξ , deg
34	Effect of contraction length on annulus flow	LUL and SUL	Both	Uniform	Long	None	40.8
35	Effect of contraction length on diffuser performance	LUL and SUL	↓	↓	↓	↓	↓
36	Effect of radial distortion on diffuser performance	---	As described for reference 9, figure 13.3				
37	Variation of early static pressure recovery with \bar{E} at constant $\bar{\beta}_a$	LUL	Long	Uniform	Long	None	Variable
38	Variation of early static pressure recovery with $\bar{\beta}_a$ at constant \bar{E}	LUL	Long	Uniform	Long	None	Variable
39	Effect of azimuthal distortion on annulus flow	↓	↓	↓	↓	All	40.8
40	Effect of azimuthal distortion on diffuser performance	↓	↓	↓	↓	All	40.8
41	Theoretical and experimental diffuser pressure distributions	↓	↓	↓	↓	None	40.8
42	Effect of diffuser centerbody length on diffuser performance	LVL and LVS	↓	Varying	Both	None	Approx. 43



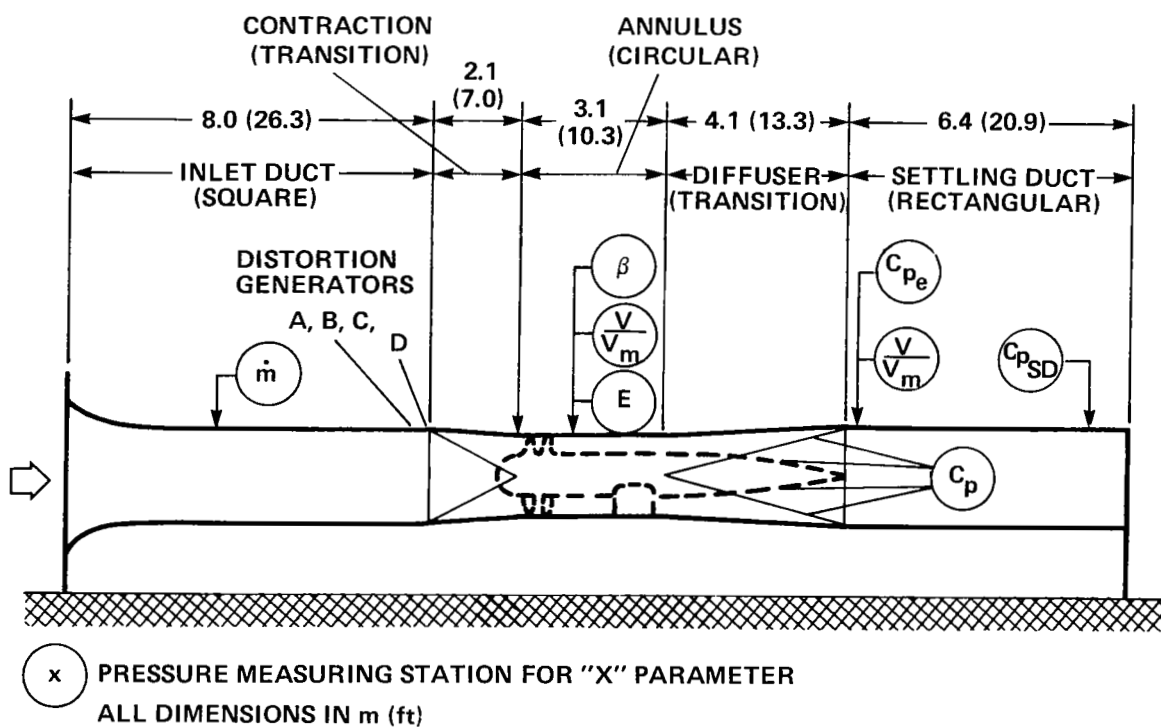


(a) View from the front quadrant.



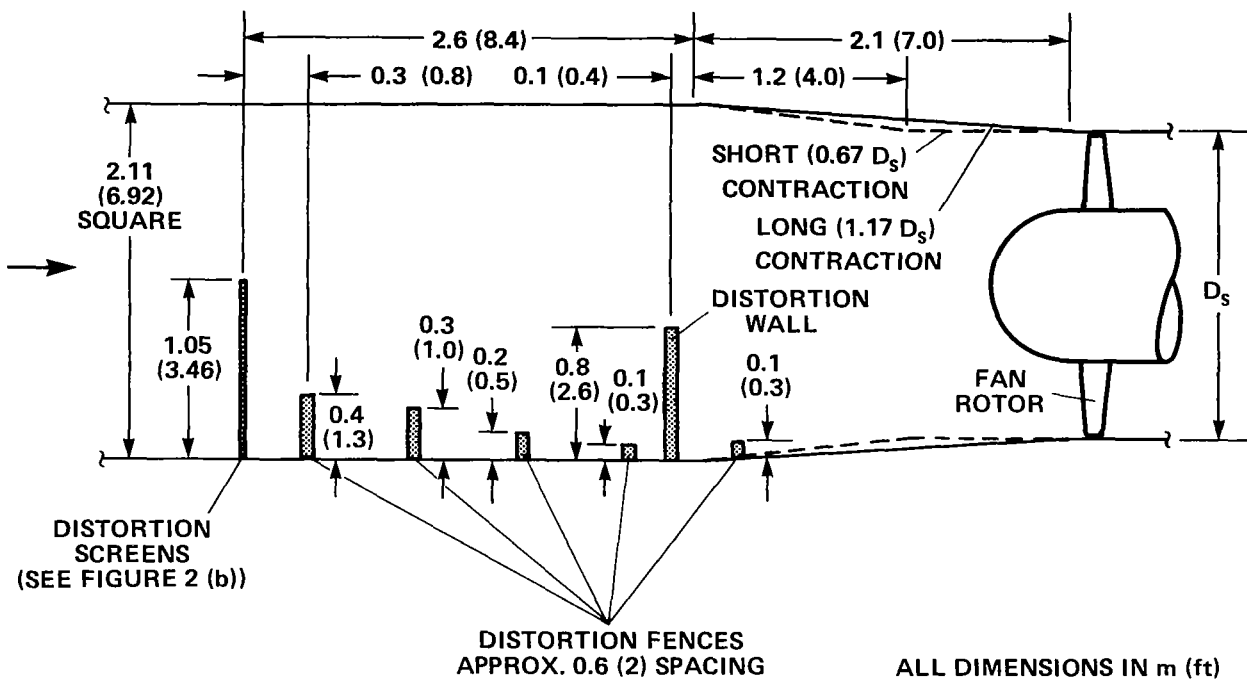
(b) View from the rear quadrant.

Figure 1.— Overall exterior views of test model and apparatus.



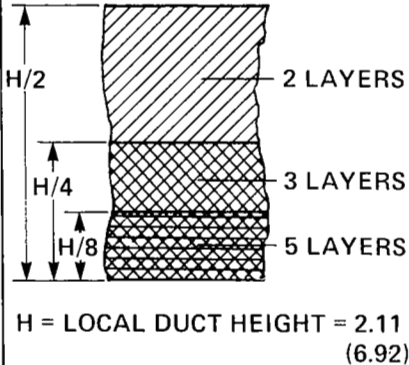
(c) Schematic of test apparatus with instrumentation locations.

Figure 1.— Concluded.



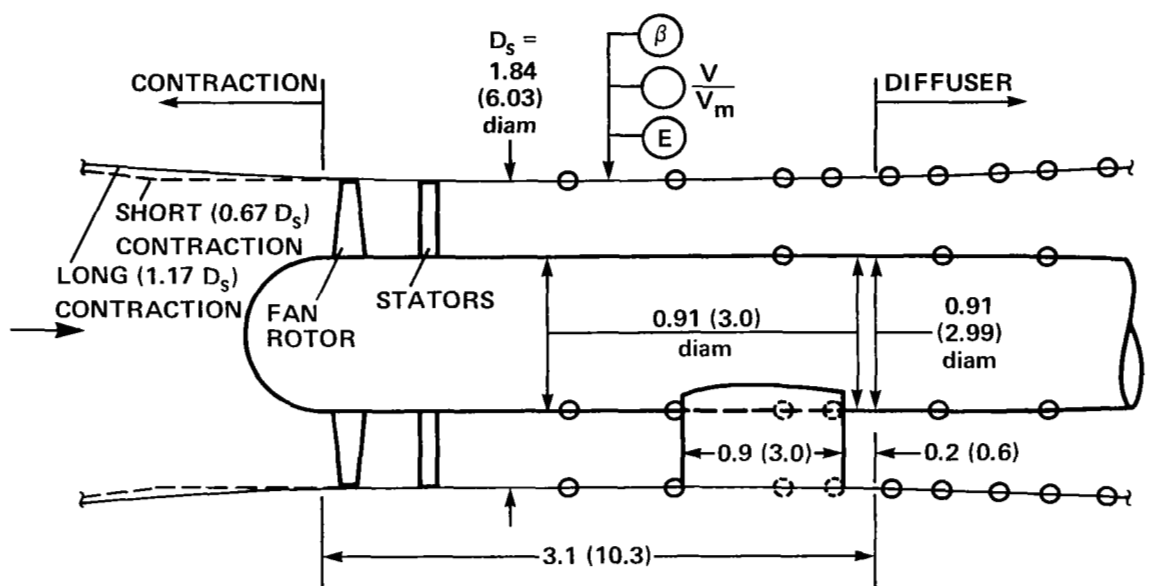
(a) Side view with distortion devices.

Figure 2.— Details of inlet duct and contraction sections.

DISTORTION TYPE		DETAILS OF DISTORTION GENERATOR		
DESIGNATION	MATERIAL	GEOMETRY	MAXIMUM HEIGHT FRACTION OF LOCAL DUCT HEIGHT	LOCATION, DISTANCE FORWARD OF CONTRACTION, FRACTION OF LOCAL DUCT HEIGHT
A	SCREENS (14 x 18 MESH)	 <p>H = LOCAL DUCT HEIGHT = 2.11 (6.92)</p>	0.5	1.21
B	SCREENS (14 x 18 MESH)	DOUBLE THAT OF "A"	0.5	1.21
C	SCREENS AND SOLID BARRIERS	DOUBLE THAT OF "A" + 5 FENCES (SEE FIGURE 2 (a))	0.5	DISTRIBUTED (SEE FIGURE 2 (a))
D	SOLID BARRIER	SOLID WALL (SEE FIGURE 2 (a))	0.4	0.06

(b) Definition and details of distortion devices.

Figure 2.— Concluded.

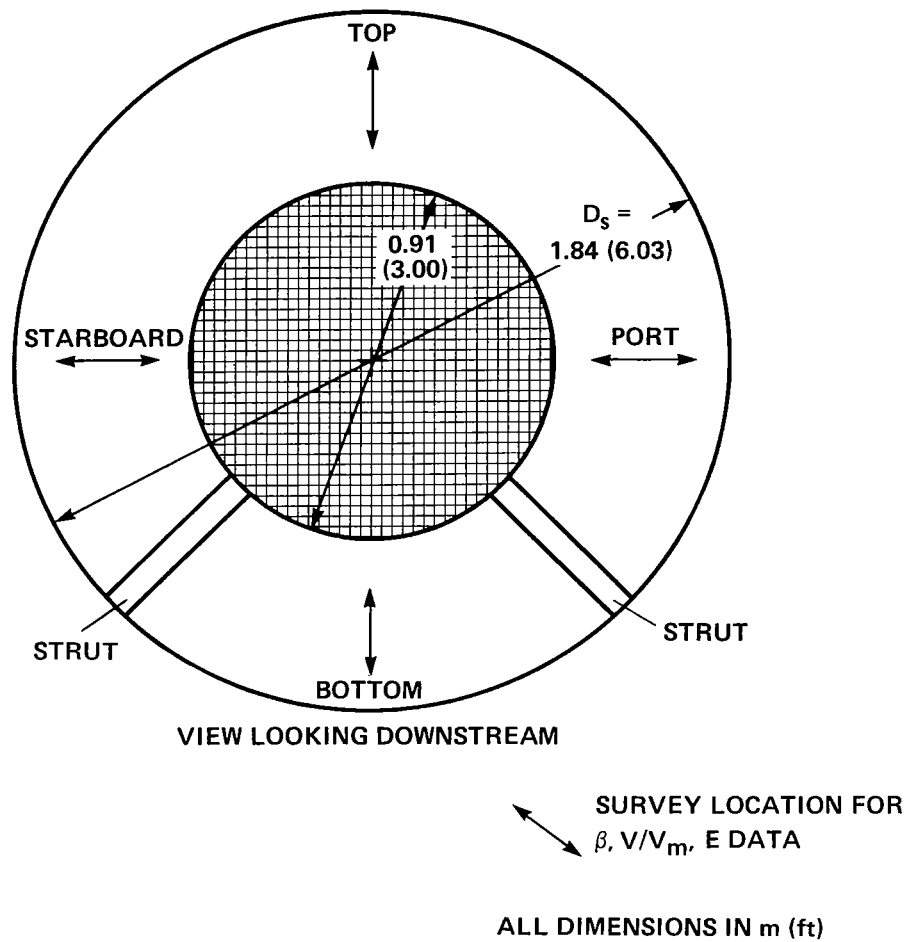


- (x) PRESSURE-SURVEY STATION FOR "X" PARAMETER (SEE FIGURE 3 (b))
- (o) PRESSURE TAP LOCATION FOR WALL STATIC PRESSURE COEFFICIENT DATA

ALL DIMENSIONS IN m (ft)

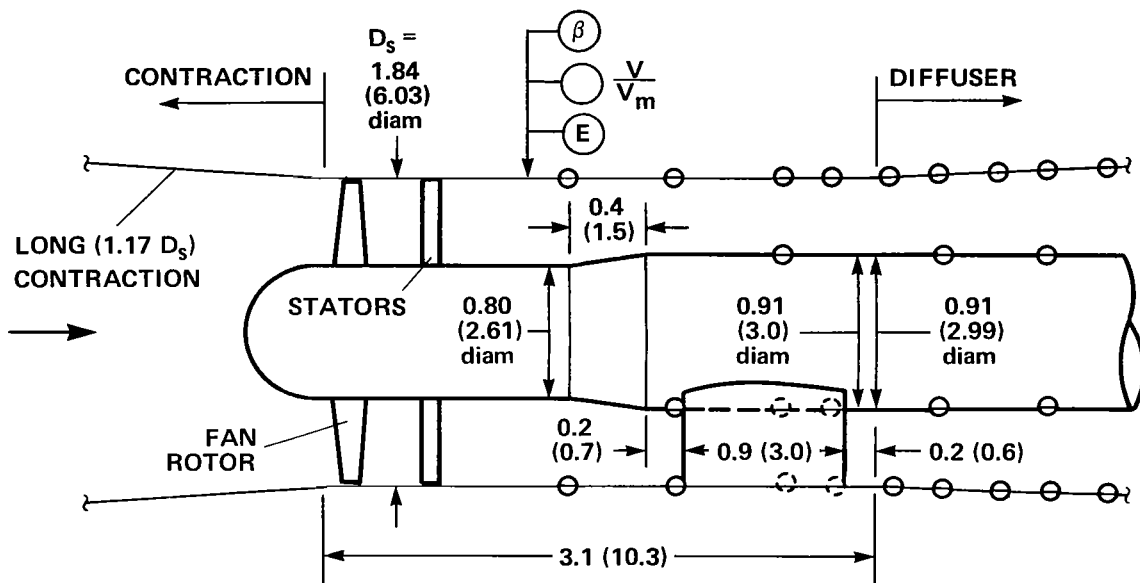
(a) Side view.

Figure 3.— Details of annulus component with uniform centerbody.



(b) Cross section at annulus survey location.

Figure 3.— Concluded.



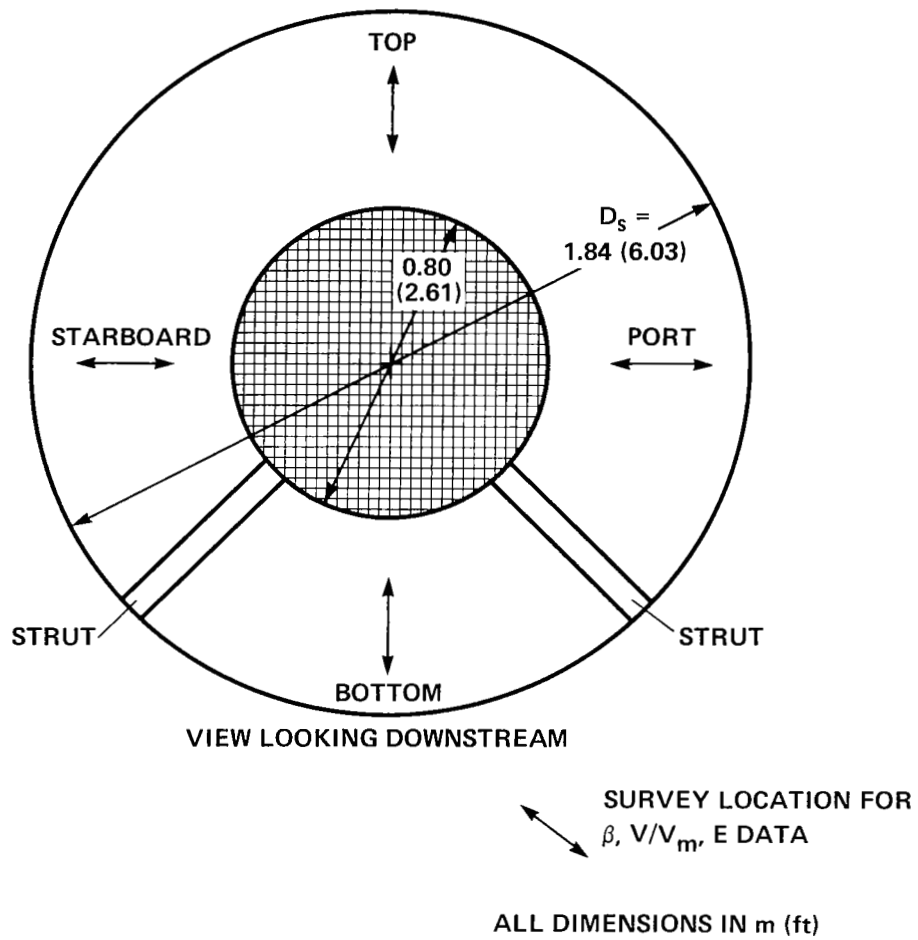
⊗ PRESSURE-SURVEY STATION FOR "X" PARAMETER (SEE FIGURE 4 (b))

○ SURFACE PRESSURE ORIFICE LOCATION FOR WALL STATIC PRESSURE COEFFICIENT DATA

ALL DIMENSIONS IN m (ft)

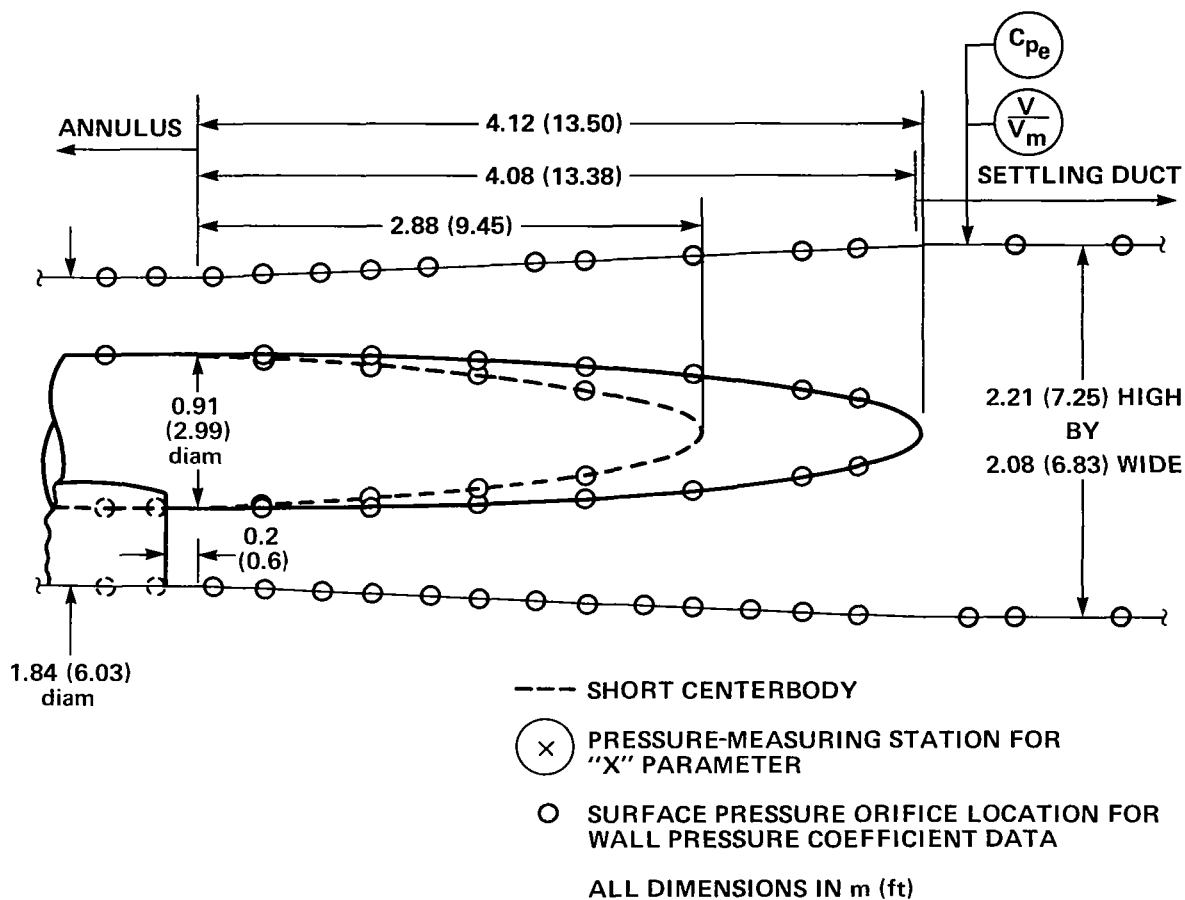
(a) Side view.

Figure 4.— Details of annulus component with varying centerbody diameter.



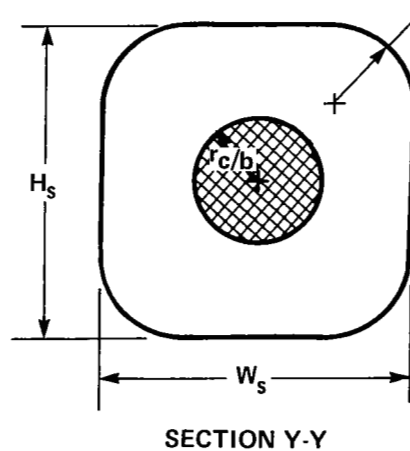
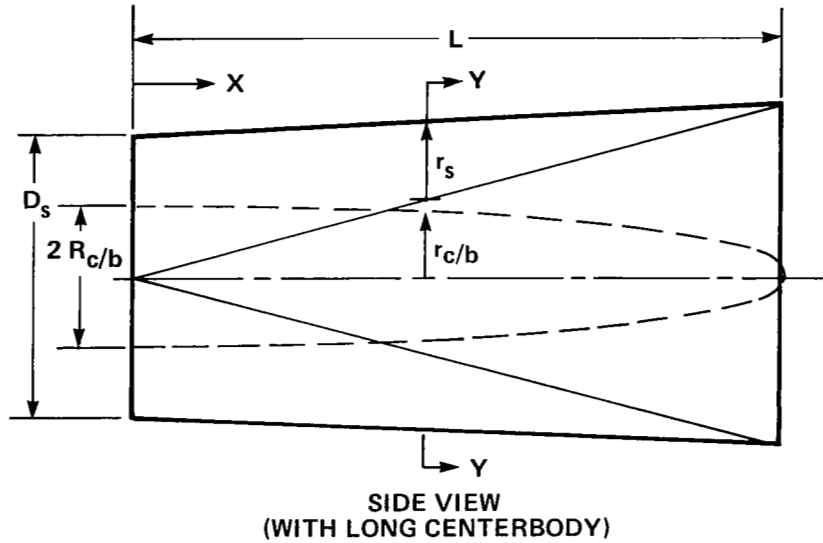
(b) Cross section at annulus survey location.

Figure 4.— Concluded.



(a) Side view.

Figure 5.— Diffuser geometries (with long and short centerbodies) and instrumentation locations.



$$D_s = 1.84 \text{ (6.03)}$$

$$L = 4.08 \text{ (13.38)}$$

$$R_{c/b} = 0.46 \text{ (1.50)}$$

$$r_{c/b} / R_{c/b} = \text{(SEE TABLE 4)}$$

$$r_s / D_s = \frac{1}{2} \left(1 - \frac{X}{L} \right)$$

$$H_s / D_s = 1 + 0.202 \left(\frac{X}{L} \right)$$

$$W_s / D_s = 1 + 0.133 \left(\frac{X}{L} \right)$$

ALL DIMENSIONS IN m (ft)

(b) Duct shape parameters.

Figure 5.— Concluded.

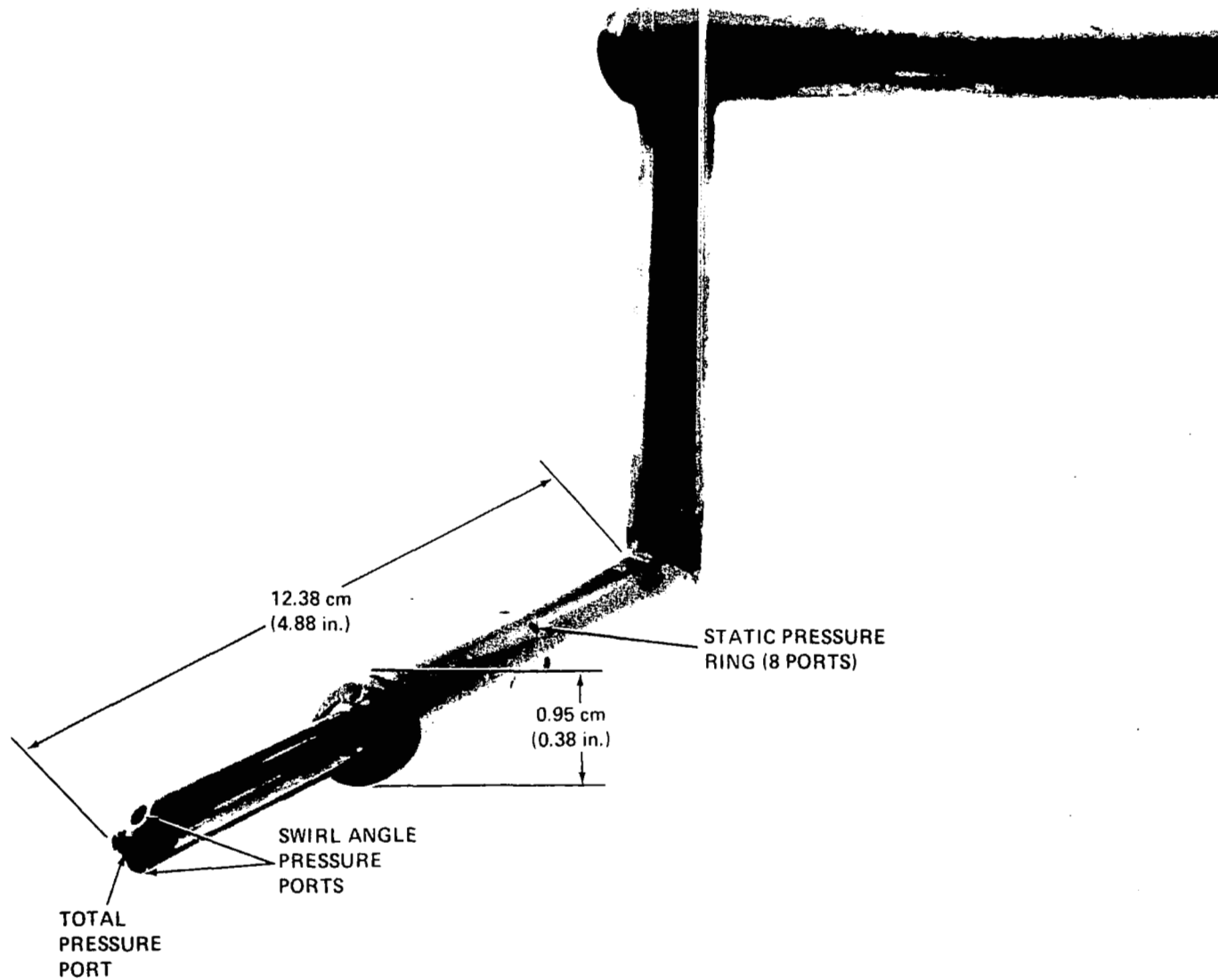
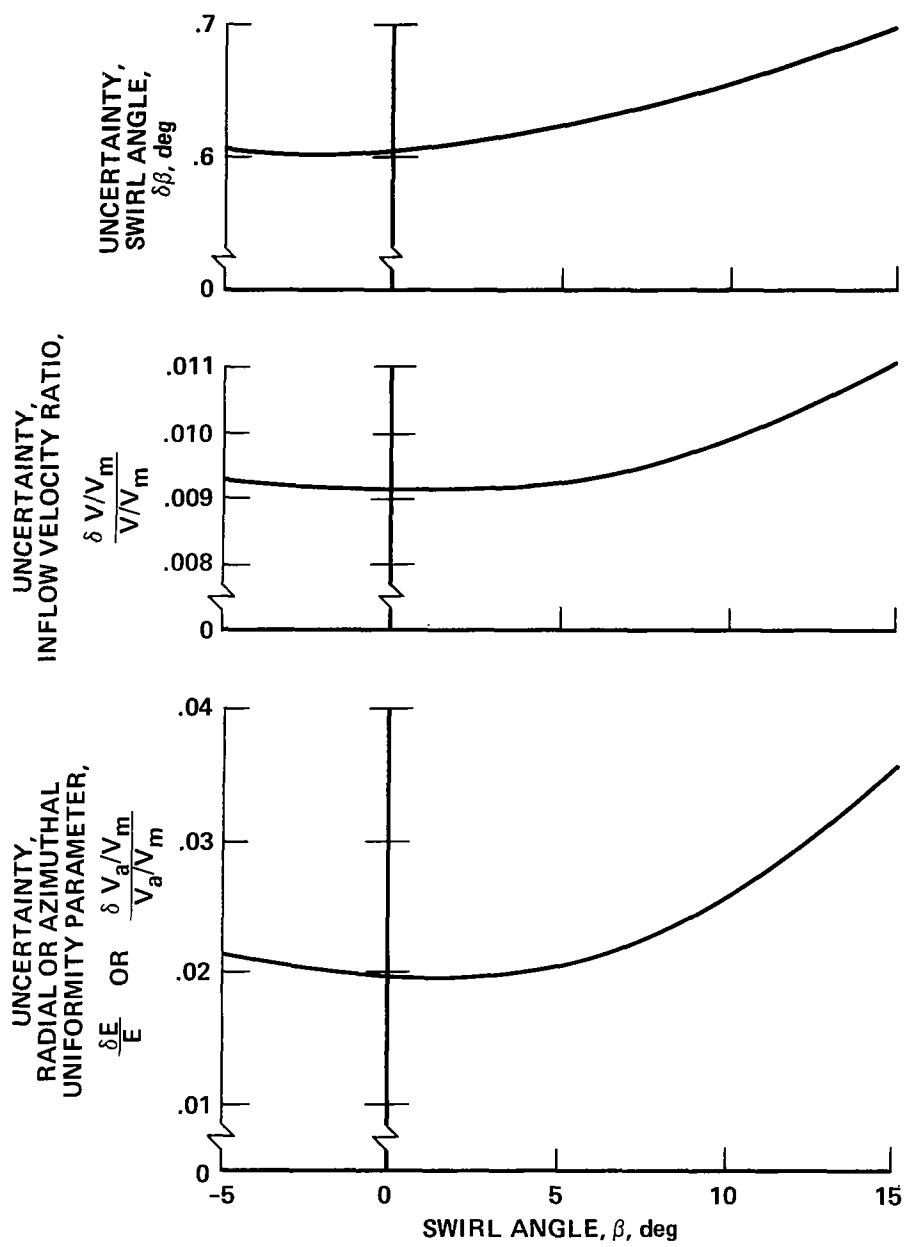
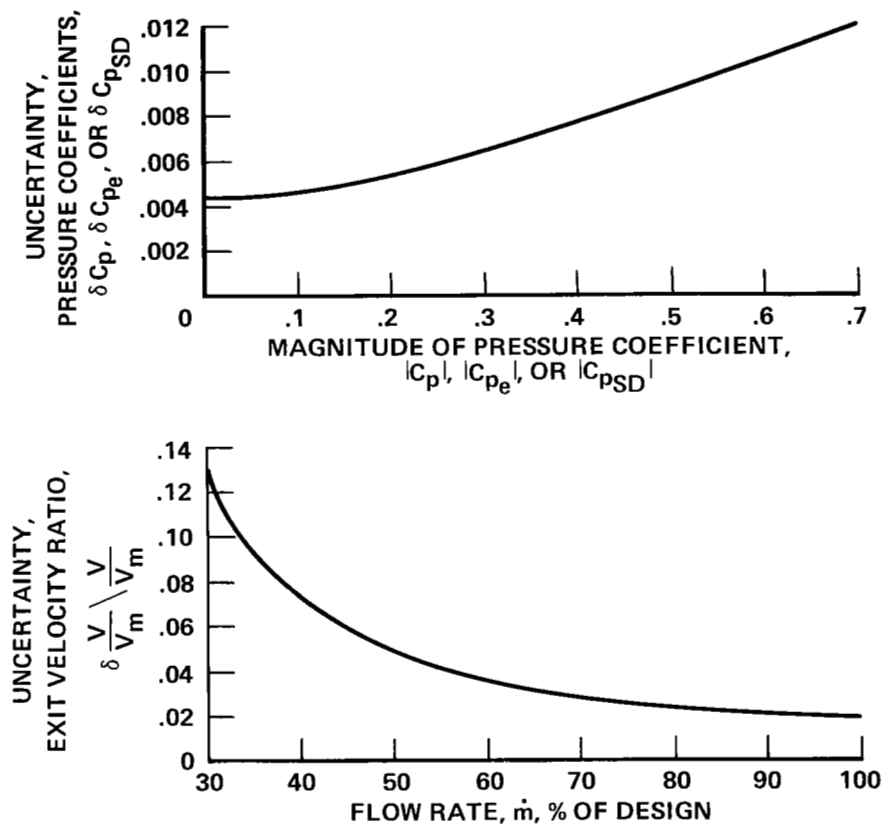


Figure 6.— Traversing six-port survey probe.



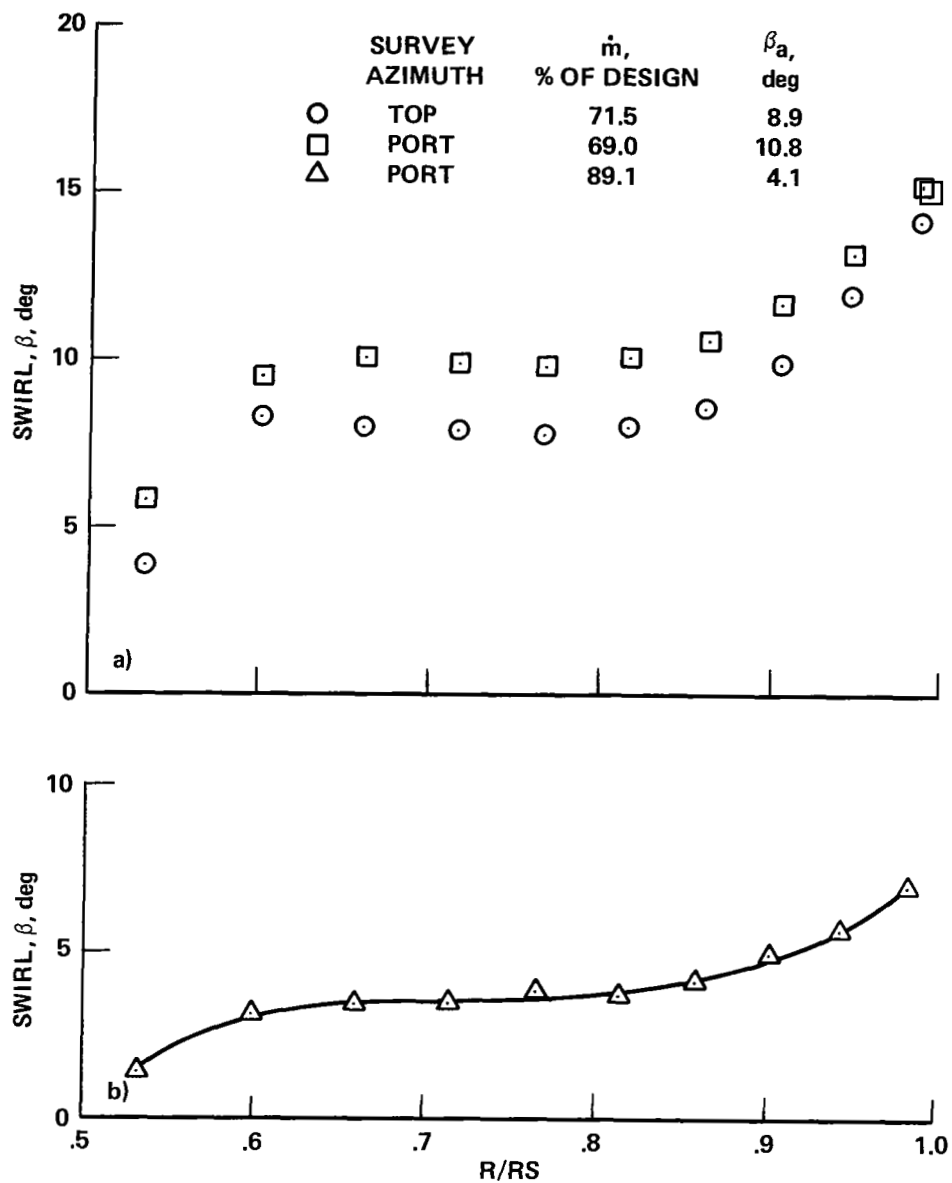
(a) Diffuser inflow data from annulus survey.

Figure 7.—Uncertainties in plotted and tabulated results.



(b) Diffuser internal and exhaust flow and performance data.

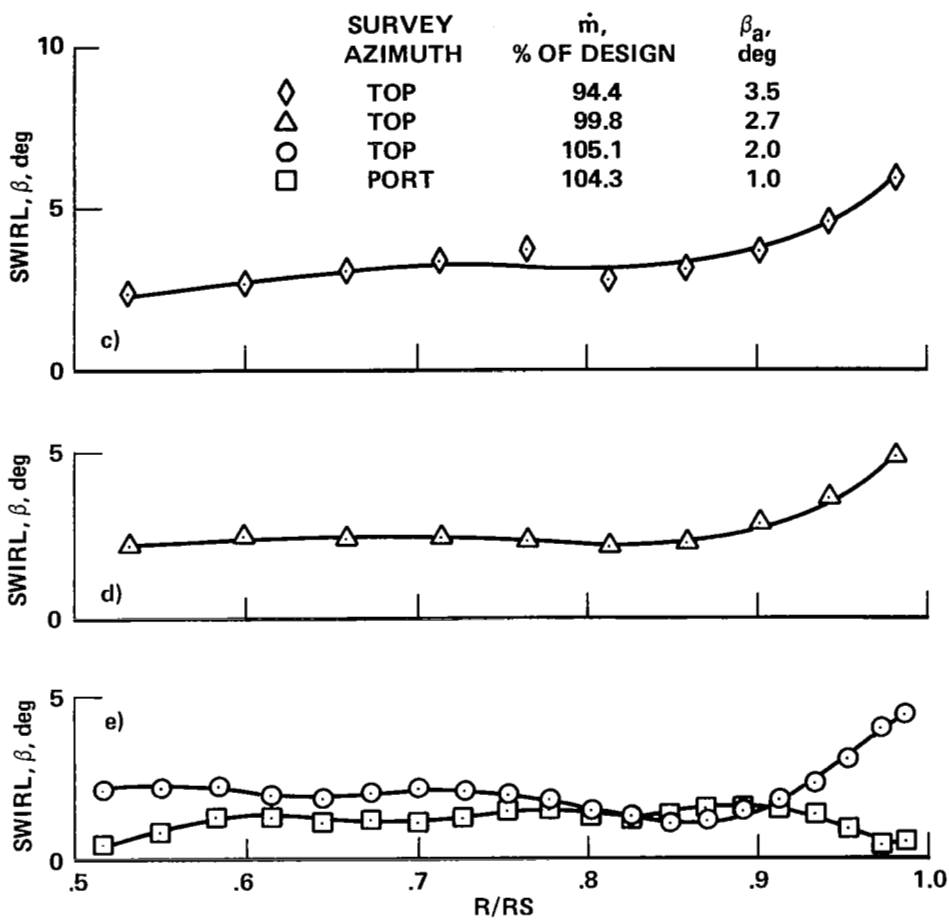
Figure 7.— Concluded.



(a) $\dot{m} \approx 70\%$

(b) $\dot{m} \approx 90\%$

Figure 8.— Annulus swirl-angle distributions for LUL configuration (see Notation and table 6) with $\xi = 40.8^\circ$ and no artificial azimuthal distortion

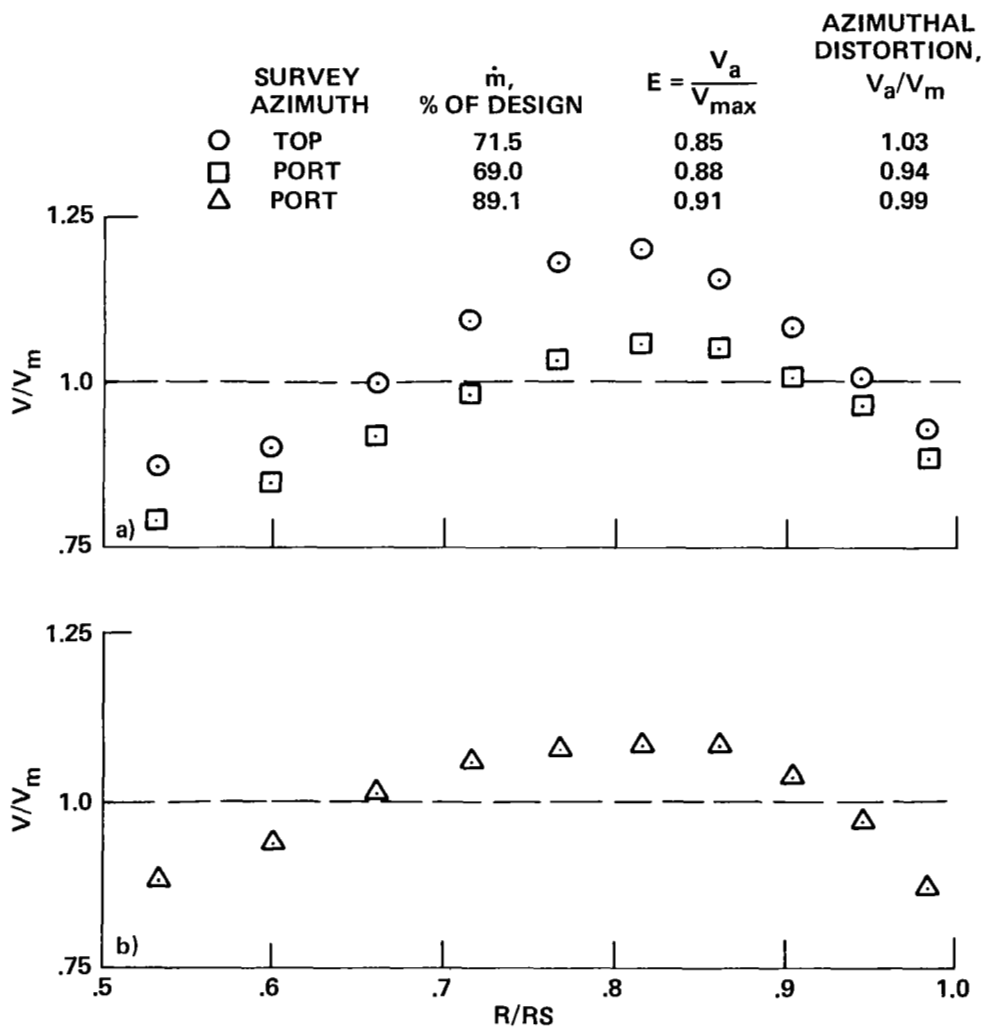


(c) $\dot{m} \approx 95\%$

(d) $\dot{m} \approx 100\%$

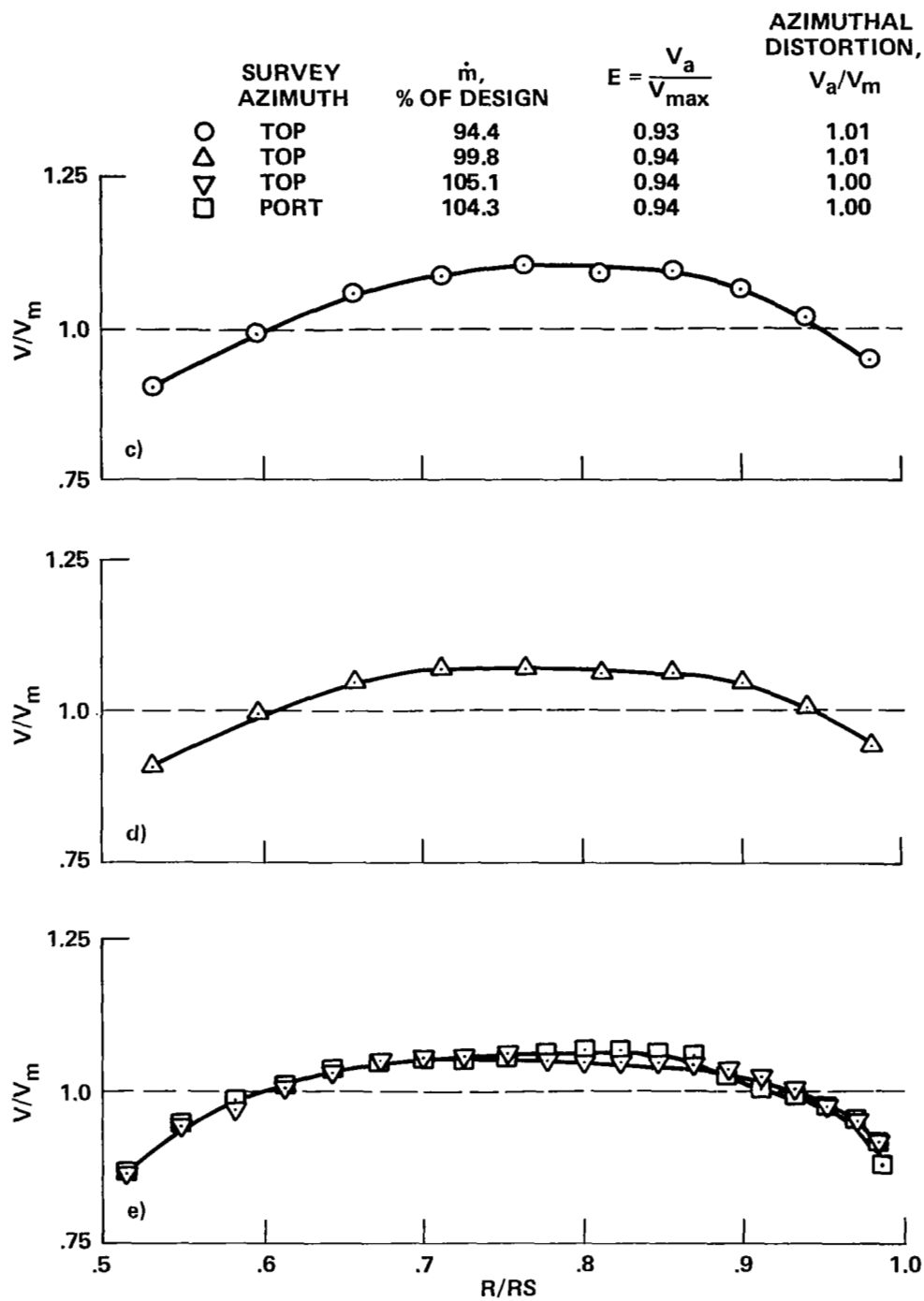
(e) $\dot{m} \approx 105\%$

Figure 8.— Concluded.



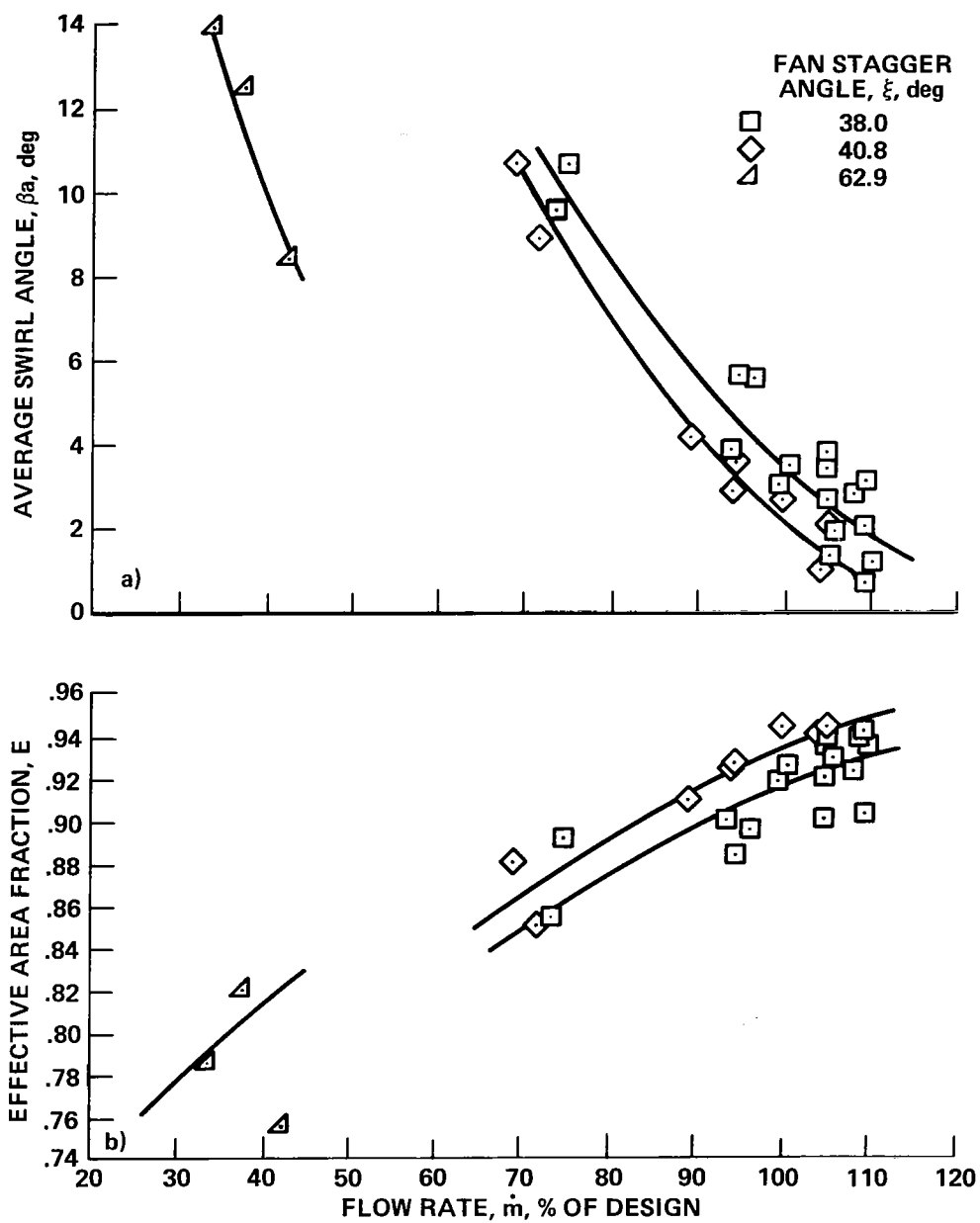
- (a) $\dot{m} \approx 70\%$
 (b) $\dot{m} \approx 90\%$

Figure 9.— Annulus velocity profiles for LUL configuration (see Notation and table 6) with $\xi = 40.8^\circ$ and no artificial azimuthal distortion.



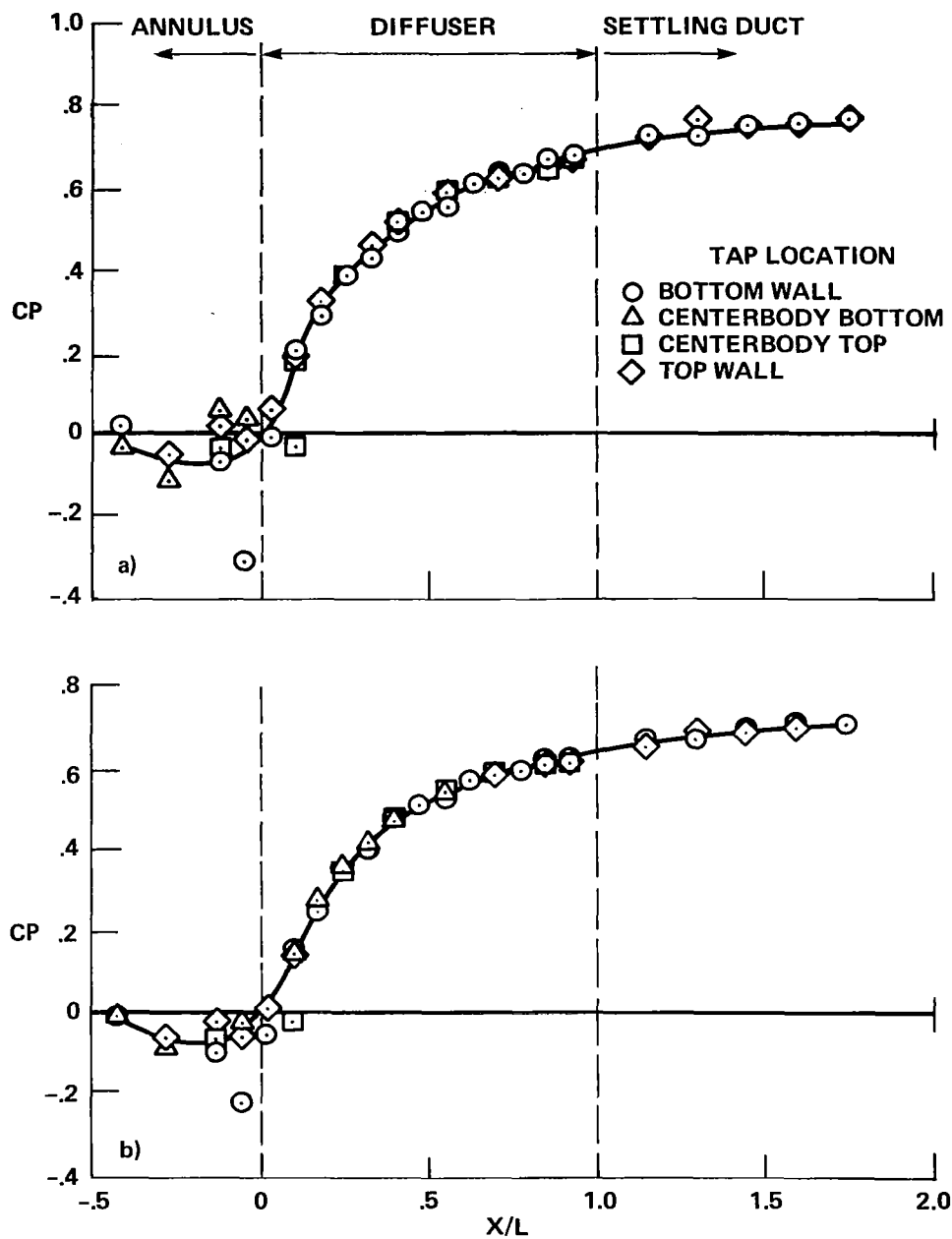
(c) $\dot{m} \approx 95\%$
 (d) $\dot{m} \approx 100\%$
 (e) $\dot{m} \approx 105\%$

Figure 9.— Concluded.



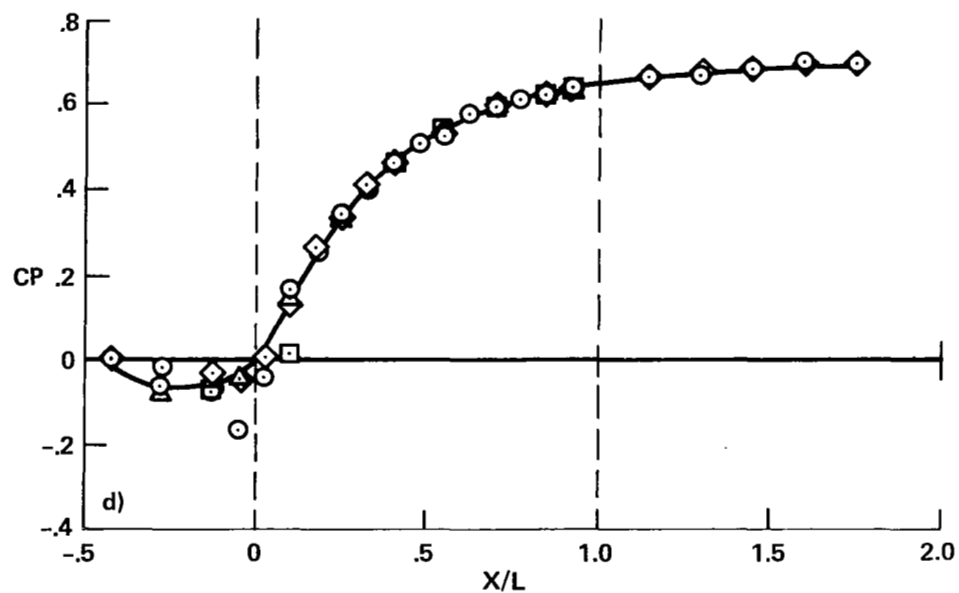
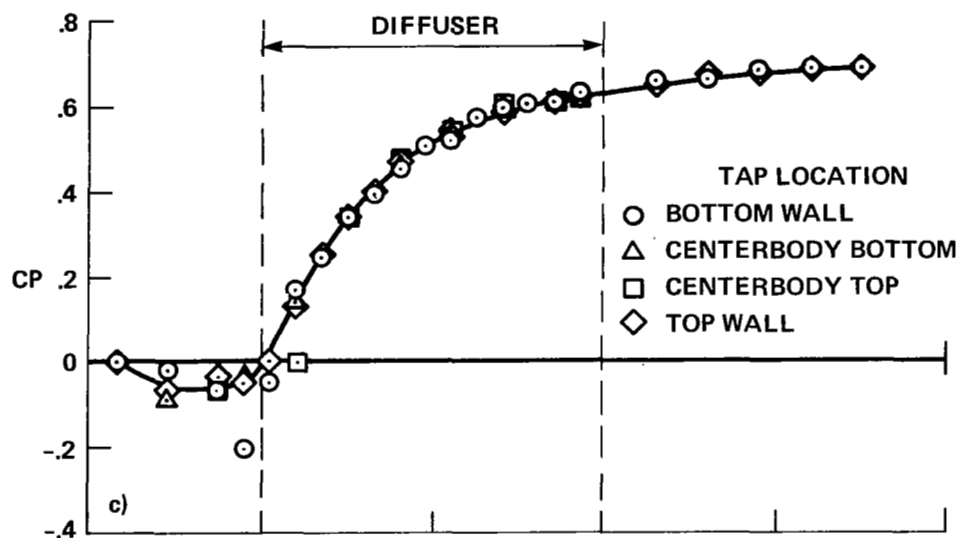
(a) Average swirl angle.
(b) Effective area fraction.

Figure 10.— Annulus flow parameters for LUL configuration (see Notation and table 6) and no artificial azimuthal distortion.



(a) $\dot{m} \approx 70\%$
 (b) $\dot{m} \approx 90\%$

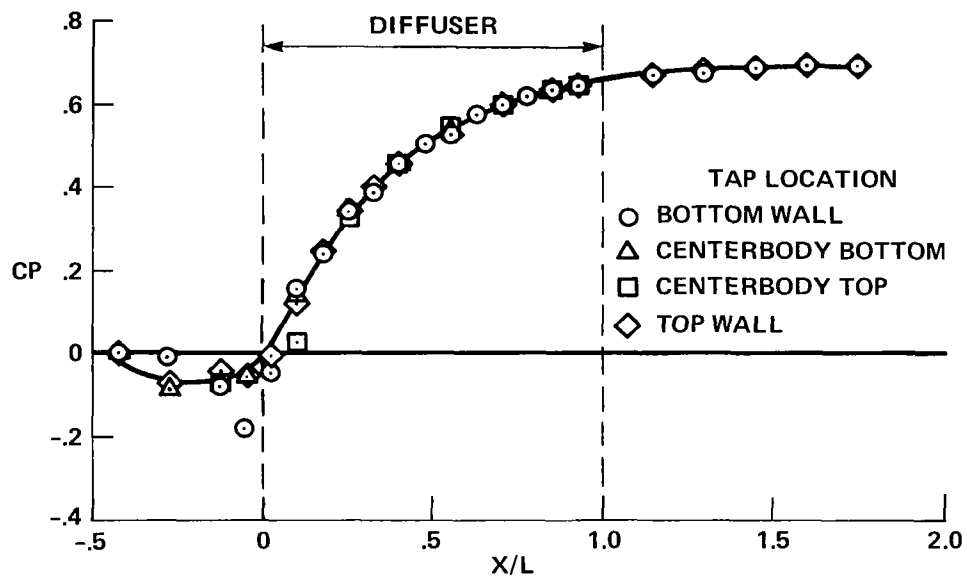
Figure 11.— Longitudinal distribution of static pressure coefficient for LUL configuration (see Notation and table 6) with $\xi = 40.8^\circ$ and no artificial azimuthal distortion.



(c) $\dot{m} \approx 95\%$

(d) $\dot{m} \approx 100\%$

Figure 11.— Continued.



(e) $\dot{m} \approx 105\%$

Figure 11.— Concluded.

		TOP			

PORT	*				
	*	1,303	1,454	1,426	1,620
	*				
	*				
	*	1,356	0,357	0,538	1,627
	*				
	*				
	*	1,129	*****	*****	1,179
	*				
	*	V/VH			
*	1,024	0,357	0,492	1,552	
*					
*					
*	1,329	1,001	0,855	1,616	
*					
*					
*	1,420	1,476	1,155	1,340	
*					

		DECIMAL POINTS SHOW APPROXIMATE PROBE LOCATIONS			
		NOTE: V/VH = ***** DENOTES REVERSE FLOW			

(a) $\dot{m} \approx 70\%$

Figure 12.— Distribution of velocity, looking upstream, near diffuser exit plane for LUL configuration (see Notation and table 6) with $\xi = 40.8^\circ$ and no artificial azimuthal distortion.

TOP				
	1,478	1,602	1,619	1,343
	1,671	0,471	0,656	1,522
	1,478	*****	*****	1,444
PORT	V/VM			
	1,222	*****	*****	1,514
	1,464	0,618	0,286	1,648
	1,088	1,582	1,548	1,175

DECIMAL POINTS SHOW APPROXIMATE PROBE LOCATIONS				
NOTE: V/VM = ***** DENOTES REVERSE FLOW				

(b) $\dot{m} \approx 90\%$

Figure 12.— Continued.

		TOP			
PORT	*	*****			
	*	1,341	1,580	1,483	1,278
	*	-----			
	*	1,632	0,546	0,695	1,557
	*	-----			
	*	1,484	*****	*****	1,481
	*	-----			
	*	V/VH			
	*	1,364	*****	*****	1,600
	*	-----			
	*	1,429	0,775	0,410	1,603
	*	-----			
	*	0,921	1,337	1,599	1,050

		DECIMAL POINTS SHOW APPROXIMATE PROBE LOCATIONS			
		NOTE: V/VH & ***** DENOTES REVERSE FLOW			

(c) $\dot{m} \approx 95\%$

Figure 12.— Continued.

TOP				
PORT	0,995	1,351	1,471	1,005
	1,547	0,752	0,822	1,521
	1,464	*****	*****	1,526
	V/VM			
	1,450	*****	*****	1,499
	1,347	0,780	0,633	1,568
	0,694	1,252	1,380	0,928

	DECIMAL POINTS SHOW APPROXIMATE PROBE LOCATIONS			
	NOTE: V/VM = ***** DENOTES REVERSE FLOW			

(d) $\dot{m} \approx 100\%$

Figure 12.— Continued.



TOP					
PORT	*****				
	*			*	
	*	0,668	1,244	1,181	0,947
	*				
	*	-----			
	*				
	*	1,432	1,012	1,052	1,548
	*				
	*	-----			
	*				
	*	1,462	0,451	0,151	1,533
	*				
	V/V _M				
*	1,393	0,226	0,192	1,472	
*					
*	-----				
*					
*	1,358	1,024	0,977	1,522	
*					
*	-----				
*					
*	0,731	1,163	1,140	0,862	
*					
*	*****				
DECIMAL POINTS SHOW APPROXIMATE PROBE LOCATIONS					

(e) $\dot{m} \approx 105\%$

Figure 12.— Concluded.

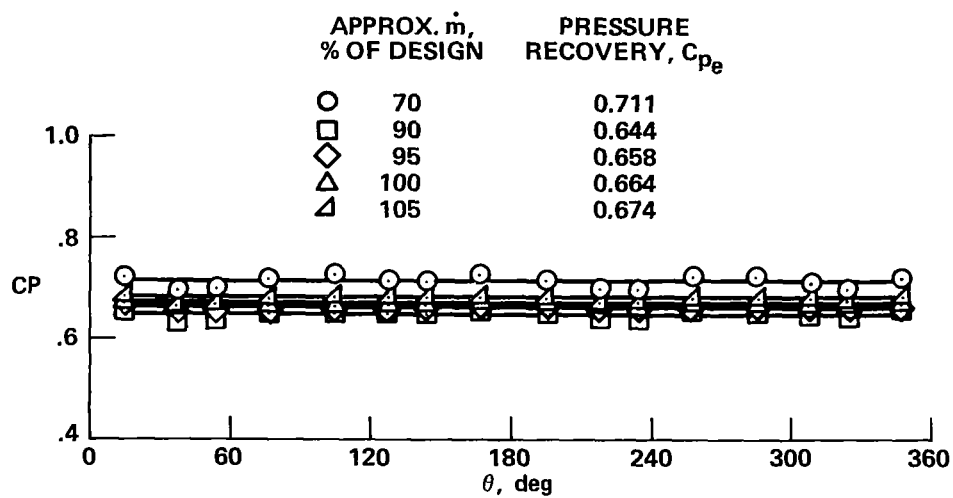
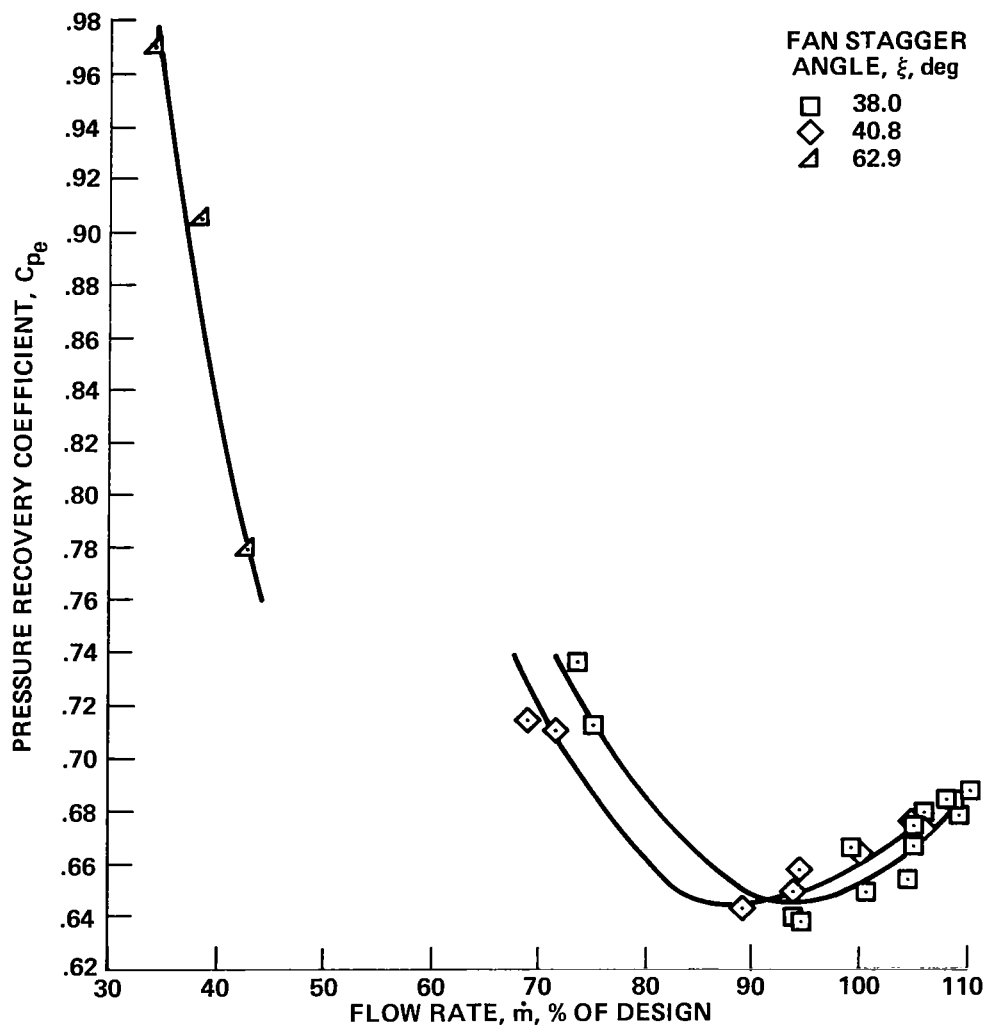
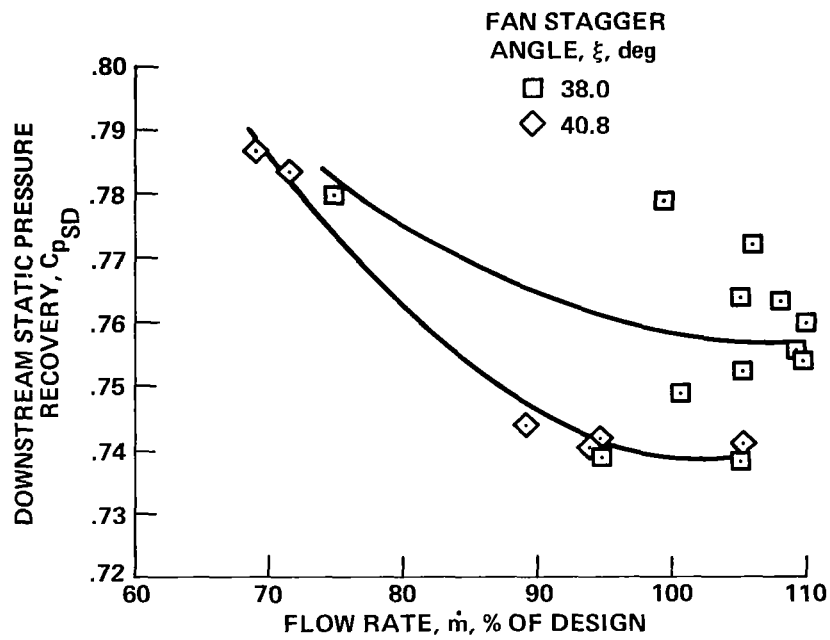


Figure 13.— Distribution of wall static pressure coefficients near diffuser exit plane for LUL configuration (see Notation and table 6) with $\xi = 40.8^\circ$ and no artificial azimuthal distortion.



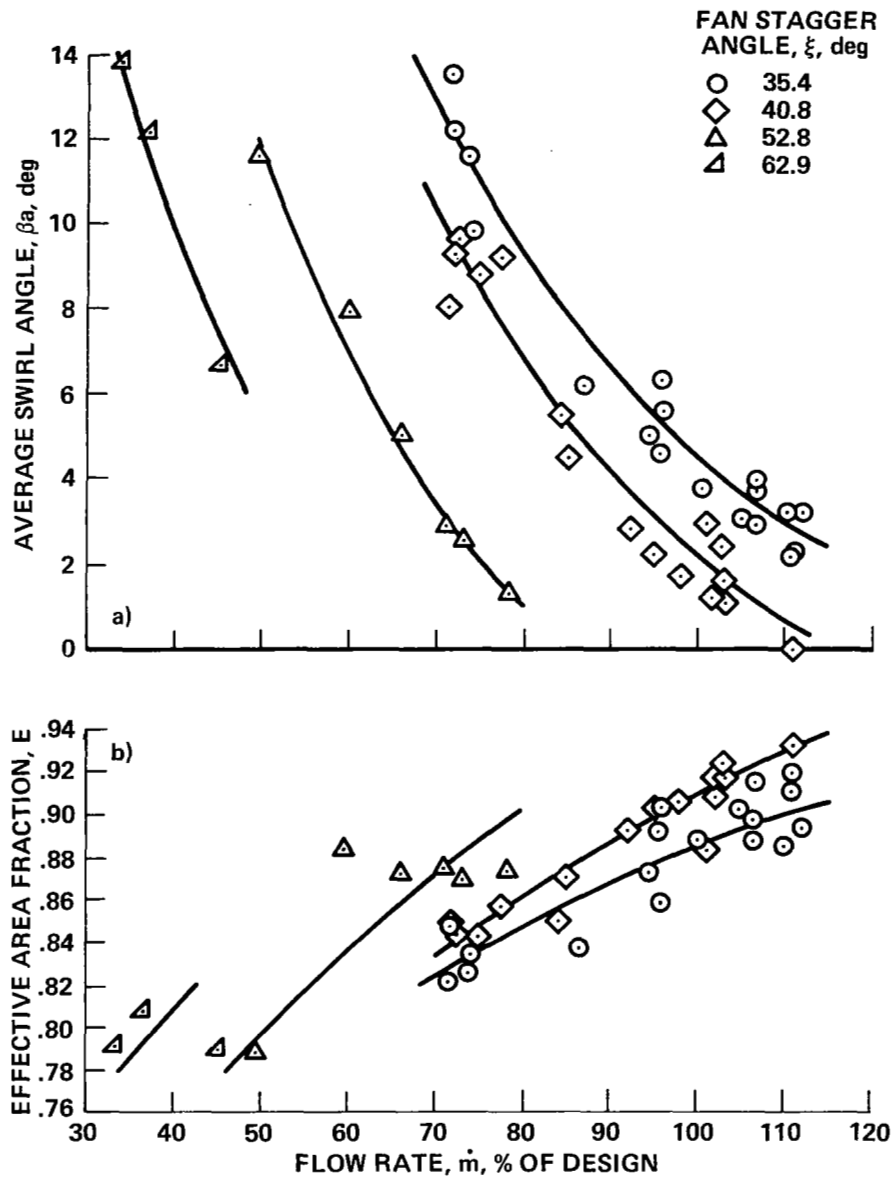
(a) Static pressure recovery coefficient near exit plane.

Figure 14.— Diffuser performance for LUL configuration (see Notation and table 6) with no artificial azimuthal distortion.



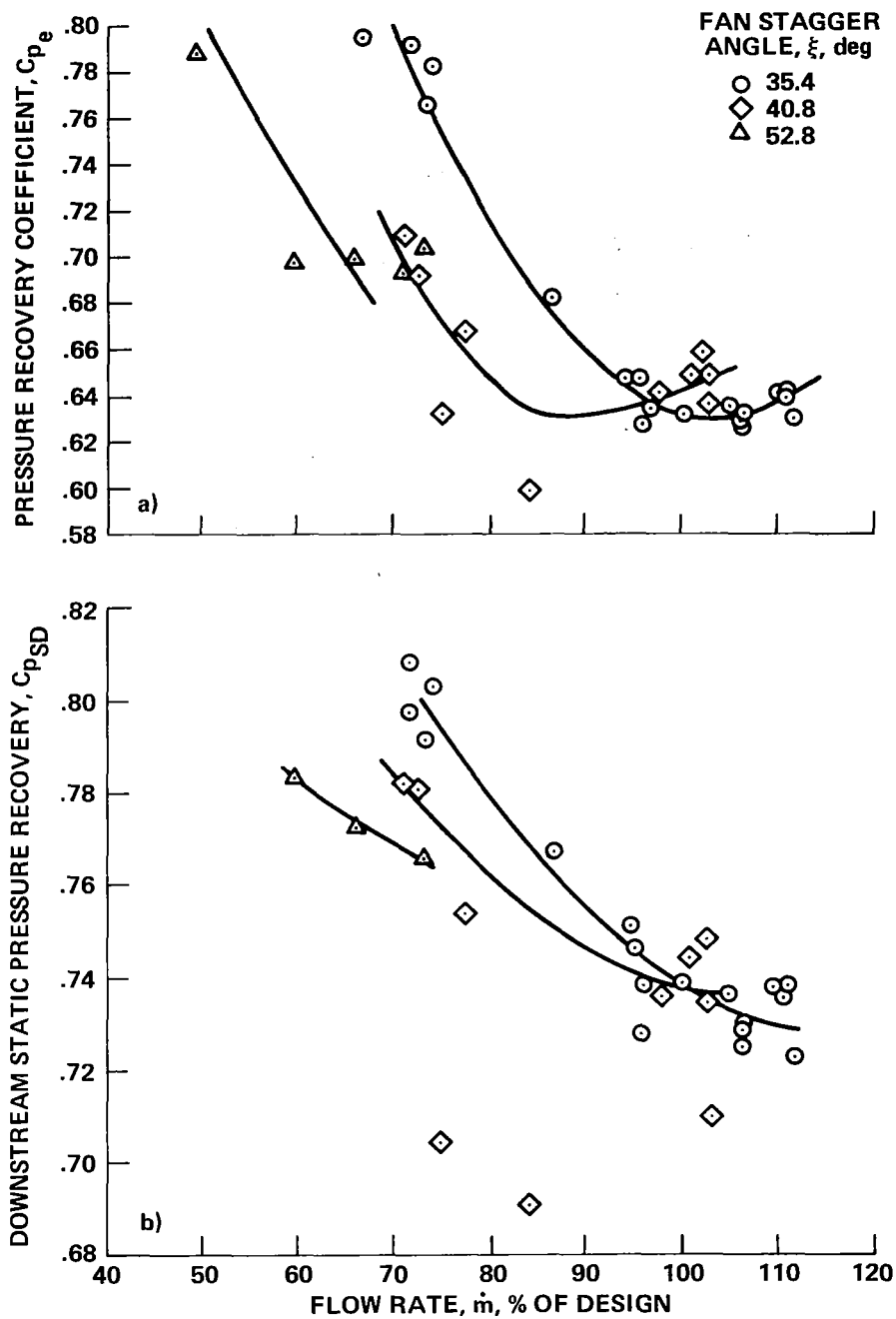
(b) Static pressure recovery in settling duct.

Figure 14.— Concluded.



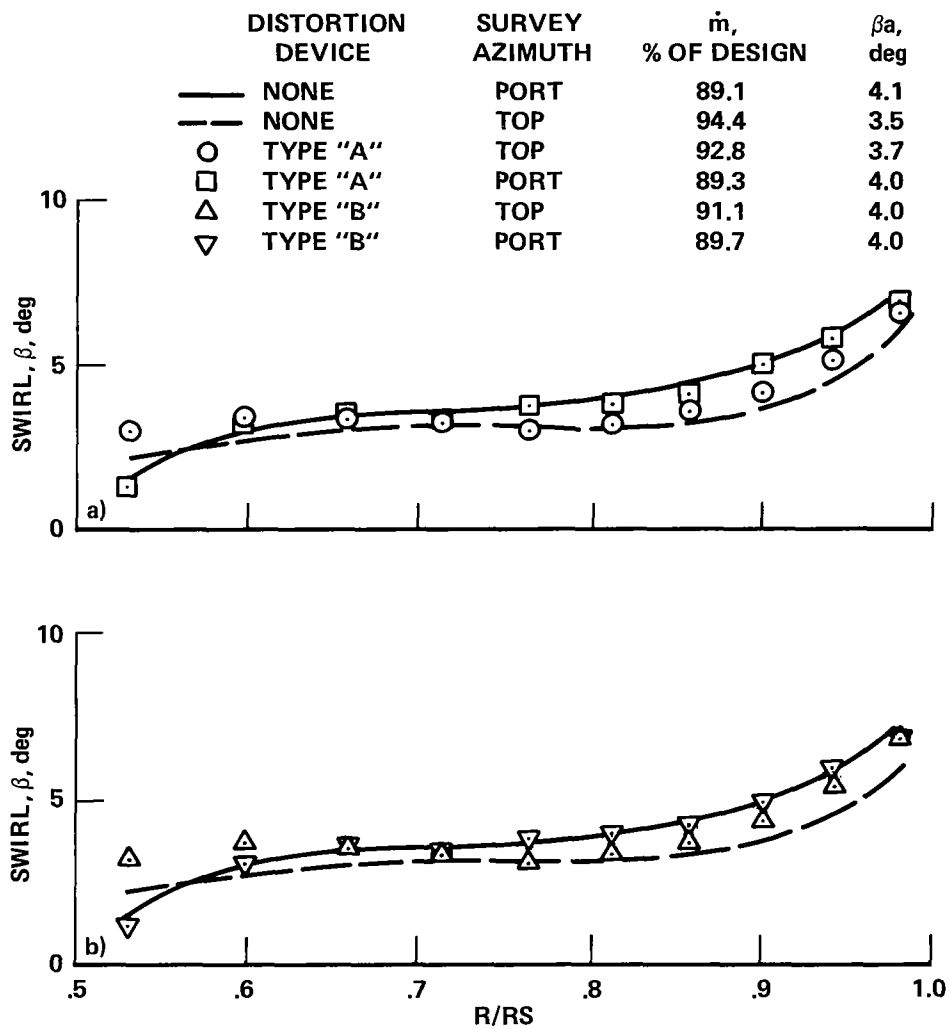
(a) Average swirl angle.
(b) Effective area fraction.

Figure 15.— Annulus flow parameters for SUL configuration (see Notation and table 6) with no artificial azimuthal distortion.



(a) Static pressure recovery coefficient near exit plane.
 (b) Static pressure recovery in settling duct.

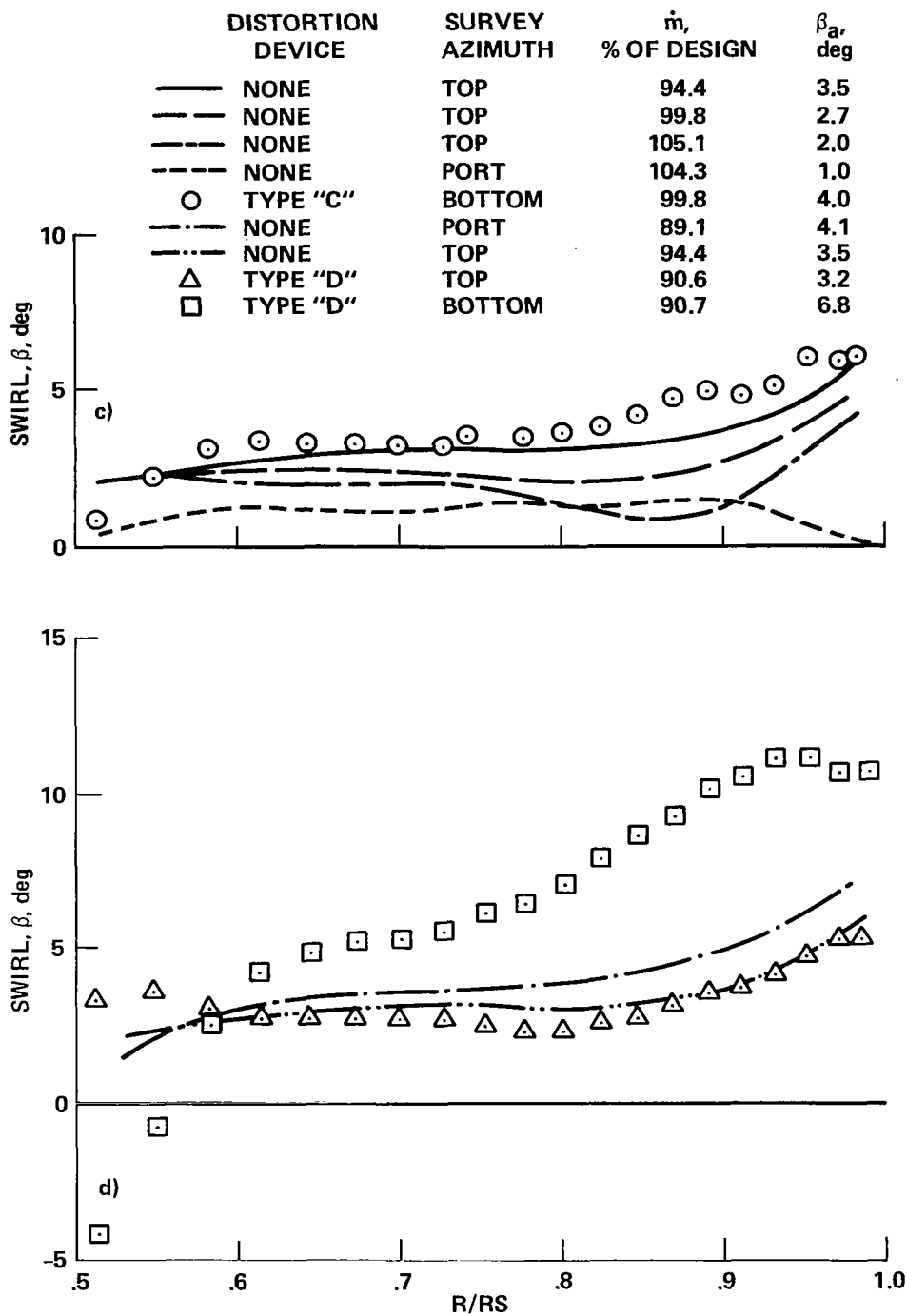
Figure 16.— Diffuser performance for SUL configuration (see Notation and table 6) with no artificial azimuthal distortion.



(a) Type A distortion.

(b) Type B distortion.

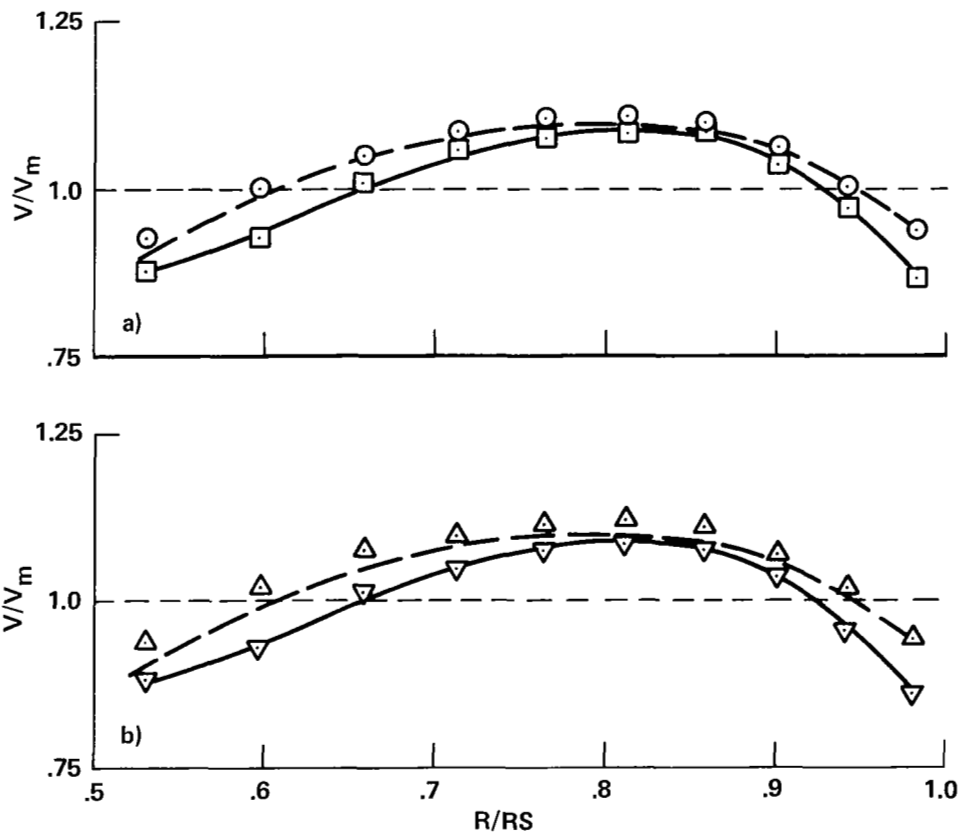
Figure 17.— Effect of distortion on annulus swirl angle for LUL configuration (see Notation and table 6) with $\xi = 40.8^\circ$.



(c) Type C distortion.
(d) Type D distortion.

Figure 17.— Concluded.

	DISTORTION DEVICE	SURVEY AZIMUTH	\dot{m} , % OF DESIGN	$E = \frac{V_a}{V_{max}}$	AZIMUTHAL DISTORTION, V_a/V_m
—	NONE	PORT	89.1	0.91	0.99
—	NONE	TOP	94.4	0.93	1.01
○	TYPE "A"	TOP	92.8	0.92	1.03
□	TYPE "A"	PORT	89.3	0.91	0.99
△	TYPE "B"	TOP	91.1	0.93	1.04
▽	TYPE "B"	PORT	89.7	0.91	0.98

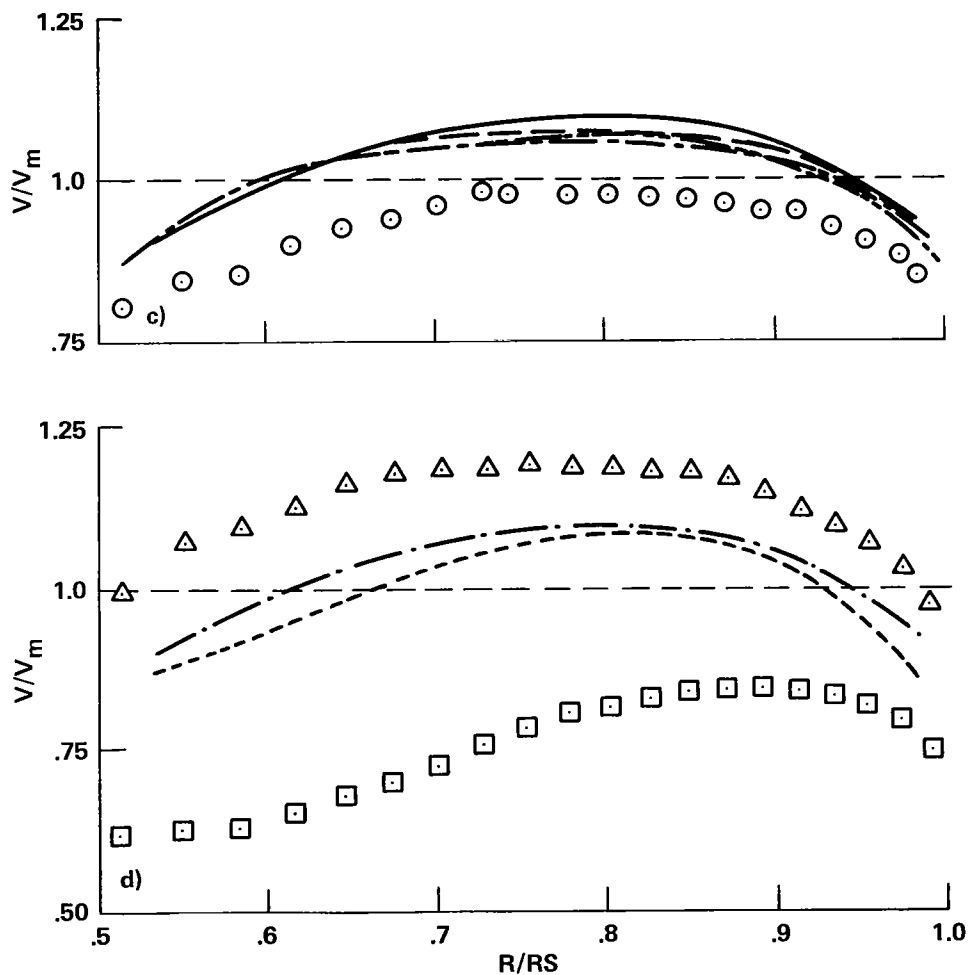


(a) Type A distortion.

(b) Type B distortion.

Figure 18.— Effect of distortion on annulus velocity profiles for LUL configuration (see Notation and table 6) with $\xi = 40.8^\circ$.

	DISTORTION DEVICE	SURVEY AZIMUTH	\dot{m} , % OF DESIGN	$E = \frac{V_a}{V_{max}}$	AZIMUTHAL DISTORTION, V_a/V_m
—	NONE	TOP	94.4	0.93	1.01
- - -	NONE	TOP	99.8	0.94	1.01
- - -	NONE	TOP	105.1	0.94	1.00
- - -	NONE	PORT	104.3	0.94	1.00
○	TYPE "C"	BOTTOM	99.8	0.93	0.91
- - -	NONE	PORT	89.1	0.91	0.99
- - -	NONE	TOP	94.4	0.93	1.01
△	TYPE "D"	TOP	90.6	0.94	1.12
□	TYPE "D"	BOTTOM	90.7	0.88	0.78



(c) Type C distortion.

(d) Type D distortion.

Figure 18.— Concluded.

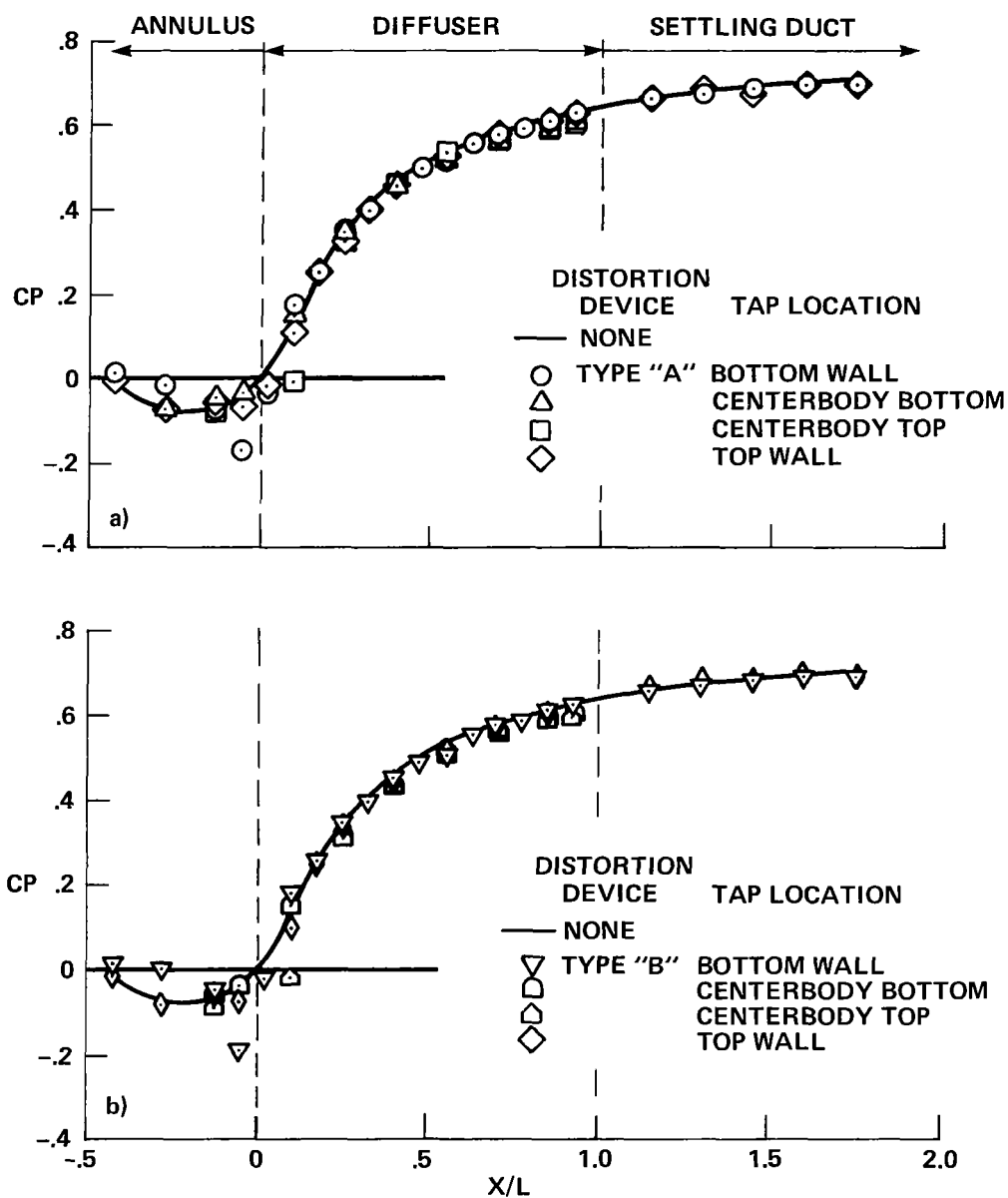
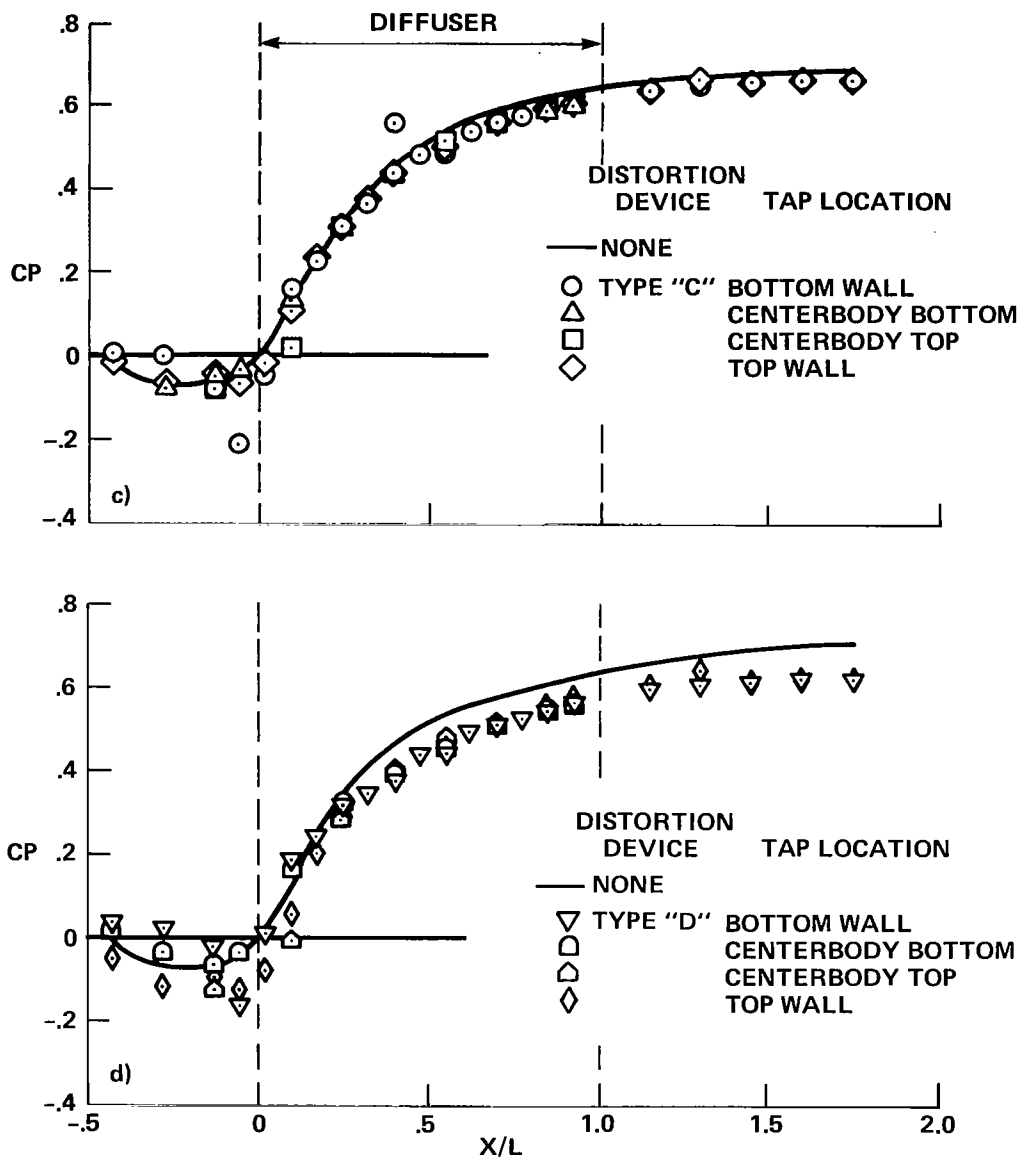
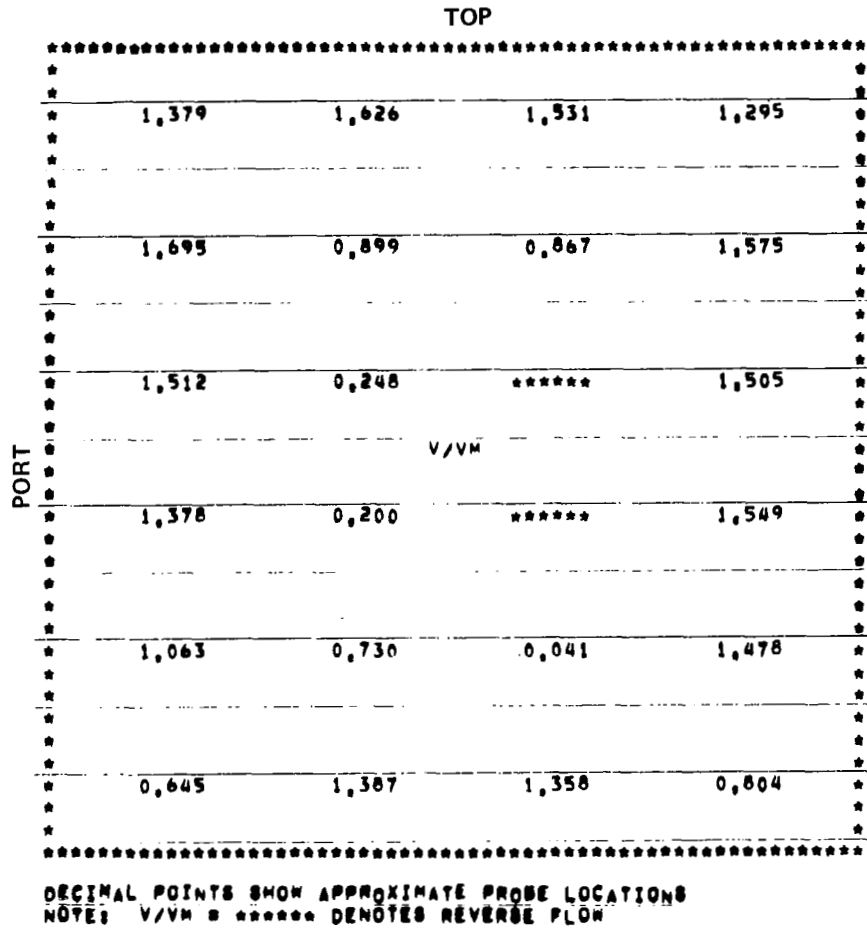


Figure 19.— Effect of distortion on longitudinal distribution of static pressure coefficient for LUL configuration (see Notation and table 6) with $\xi = 40.8^\circ$.



(c) Type C distortion at $\dot{m} \approx 100\%$.
 (d) Type D distortion at $\dot{m} \approx 90\%$.

Figure 19.— Concluded.



(a) Type A distortion at $\dot{m} \approx 90\%$.

Figure 20.— Velocity distribution, looking upstream, near diffuser exit plane for azimuthally distorted inflow to LUL configuration (see Notation and table 6) with $\xi = 40.8^\circ$.

		TOP			
PORT	*****	1,378	1,628	1,579	1,342
		1,677	1,012	0,887	1,621
		1,482	0,434	*****	1,502
		V/VH			
		1,255	0,310	*****	1,555
		0,928	0,751	0,276	1,417
		0,462	1,336	1,282	0,815

		DECIMAL POINTS SHOW APPROXIMATE PROBE LOCATIONS			
		NOTE: V/VH = ***** DENOTES REVERSE FLOW			

(b) Type B distortion at $\dot{m} \approx 90\%$.

Figure 20.— Continued.

	TOP			

	1,165	1,426	1,417	0,920

	1,589	1,028	0,897	1,316

	1,531	0,541	*****	1,437

	V/V _M			
	1,315	0,477	0,108	1,484

	1,204	1,043	0,521	1,232

	0,655	1,129	1,254	0,782

	DECIMAL POINTS SHOW APPROXIMATE PROBE LOCATIONS			
	NOTE: V/V _M = ***** DENOTES REVERSE FLOW			

(c) Type C distortion at $\dot{m} \approx 100\%$.

Figure 20.— Continued.

TOP					
PORT	*****				
		1,492	1,760	1,861	1,330

		1,948	1,624	0,904	1,678

		1,855	0,981	0,236	1,457

	V/VM				

		1,418	0,665	0,236	1,129

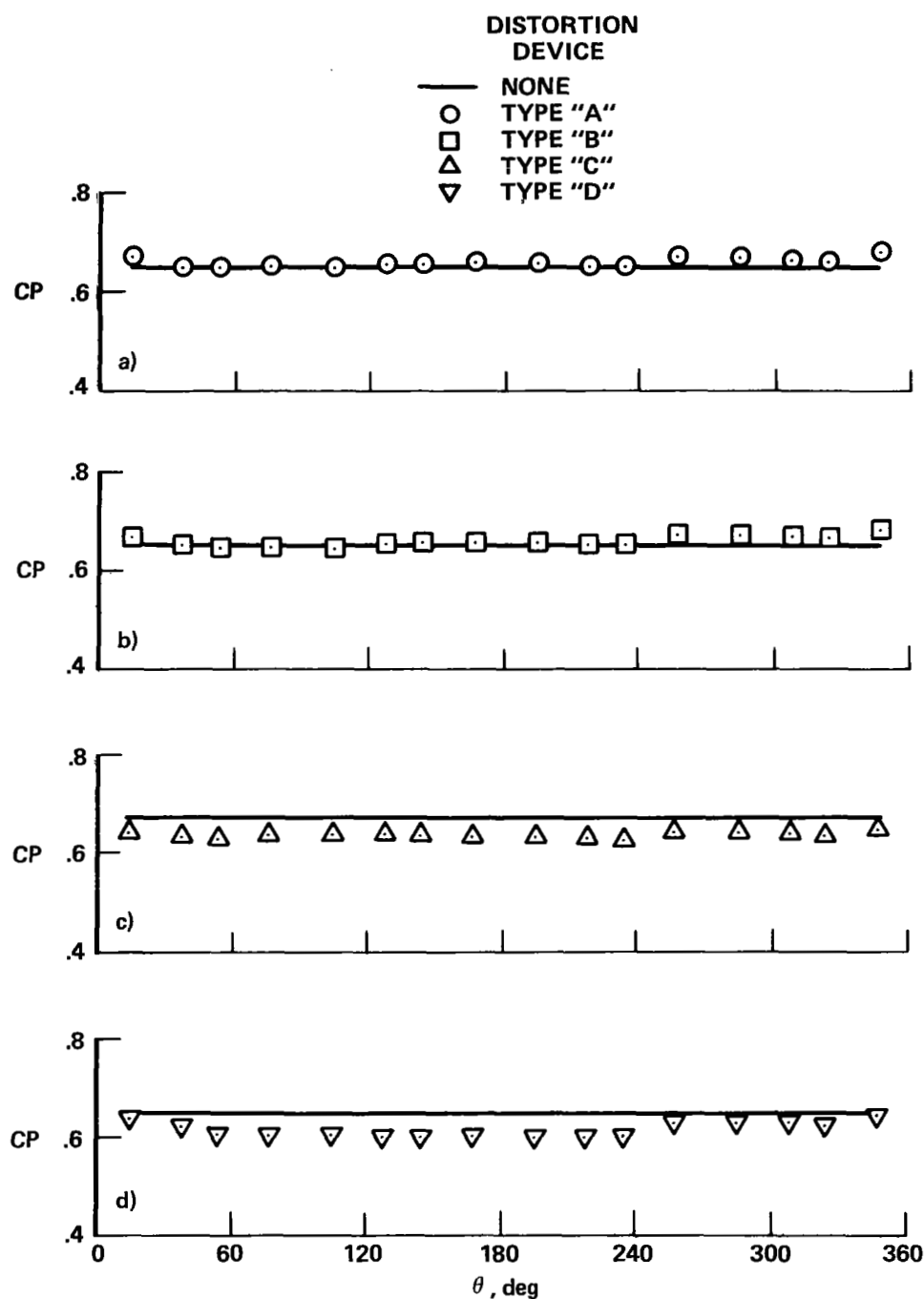
	0,759	0,449	*****	0,740	

	0,622	0,759	0,640	0,583	

DECIMAL POINTS SHOW APPROXIMATE PROBE LOCATIONS					
NOTE: V/VM = ***** DENOTES REVERSE FLOW					

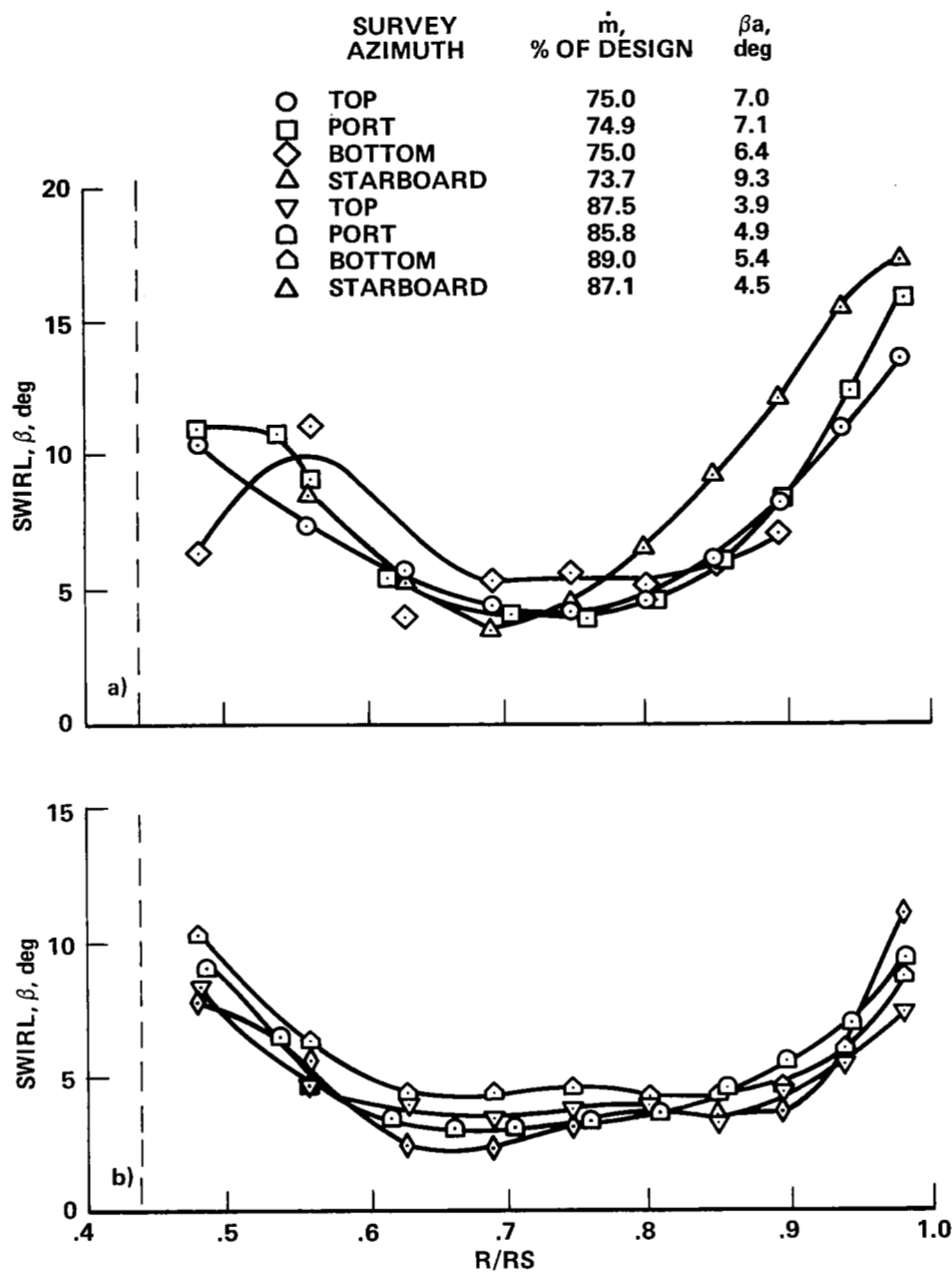
(d) Type D distortion at $\dot{m} \approx 90\%$.

Figure 20.— Concluded.



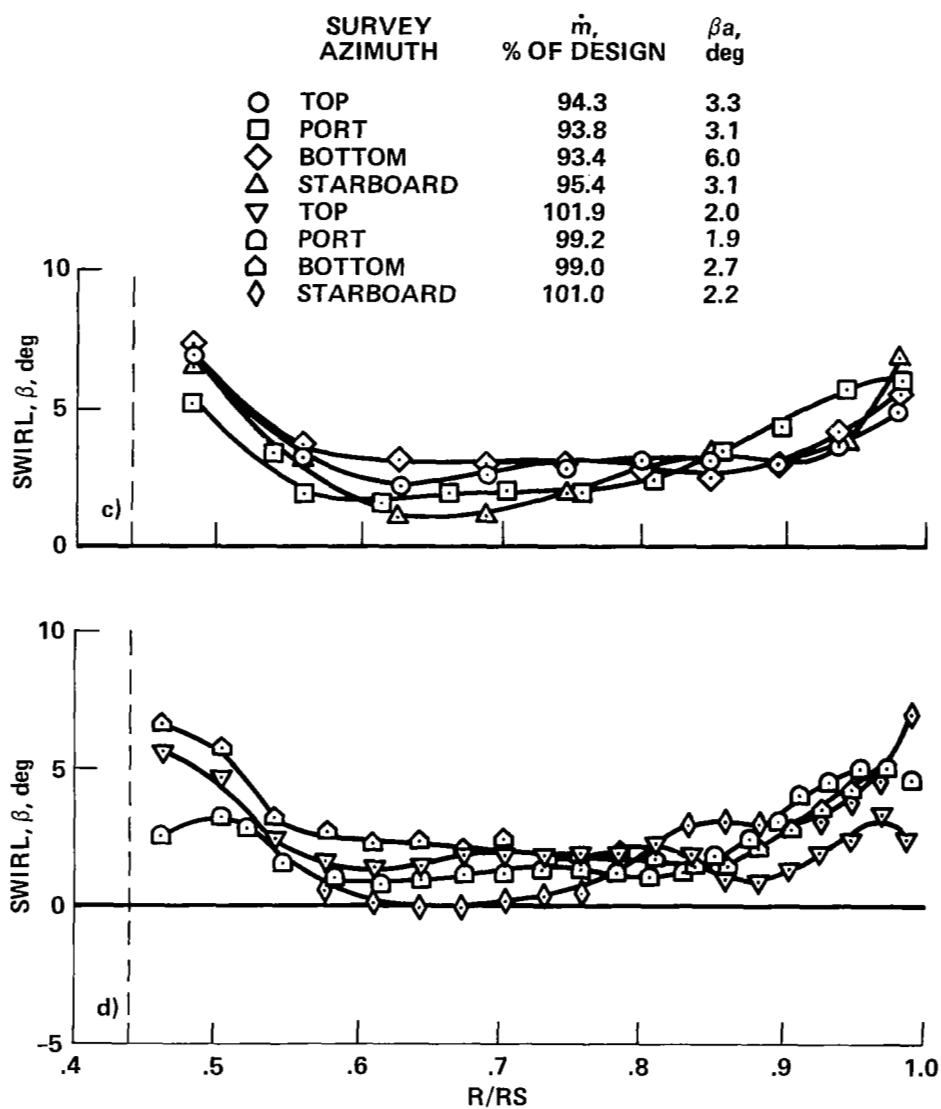
- (a) Type A distortion at $\dot{m} \approx 90\%$.
 (b) Type B distortion at $\dot{m} \approx 90\%$.
 (c) Type C distortion at $\dot{m} \approx 100\%$.
 (d) Type D distortion at $\dot{m} \approx 90\%$.

Figure 21.— Effect of distortion on wall static pressure coefficients near diffuser exit plane for LUL configuration (see Notation and table 6) with $\xi = 40.8^\circ$.



(a) $\dot{m} \approx 75\%$
 (b) $\dot{m} \approx 85\%$

Figure 22.— Annulus swirl-angle distributions for LVL configuration (see Notation and table 6) with $\xi = 43.2^\circ$ and no artificial azimuthal distortion.



(c) $\dot{m} \approx 95\%$
 (d) $\dot{m} \approx 100\%$

Figure 22.— Continued.

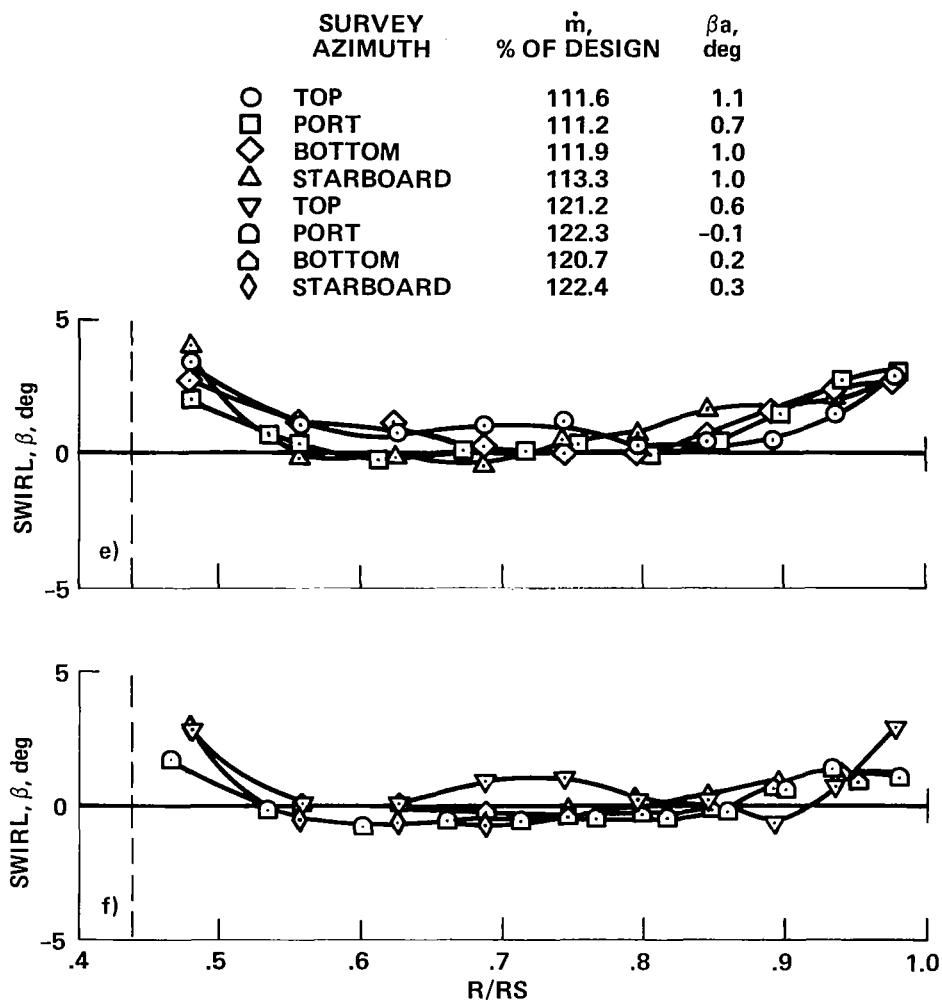
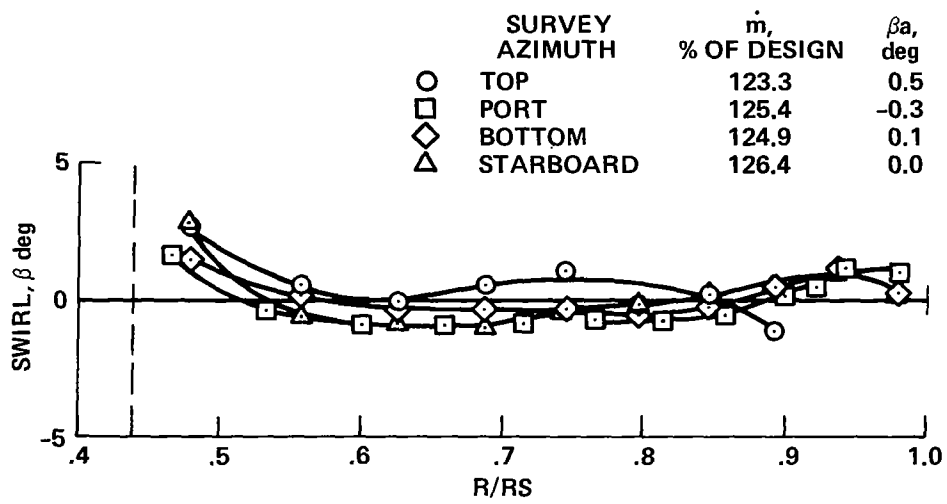


Figure 22.— Continued.



(g) $\dot{m} \approx 125\%$

Figure 22.— Concluded.

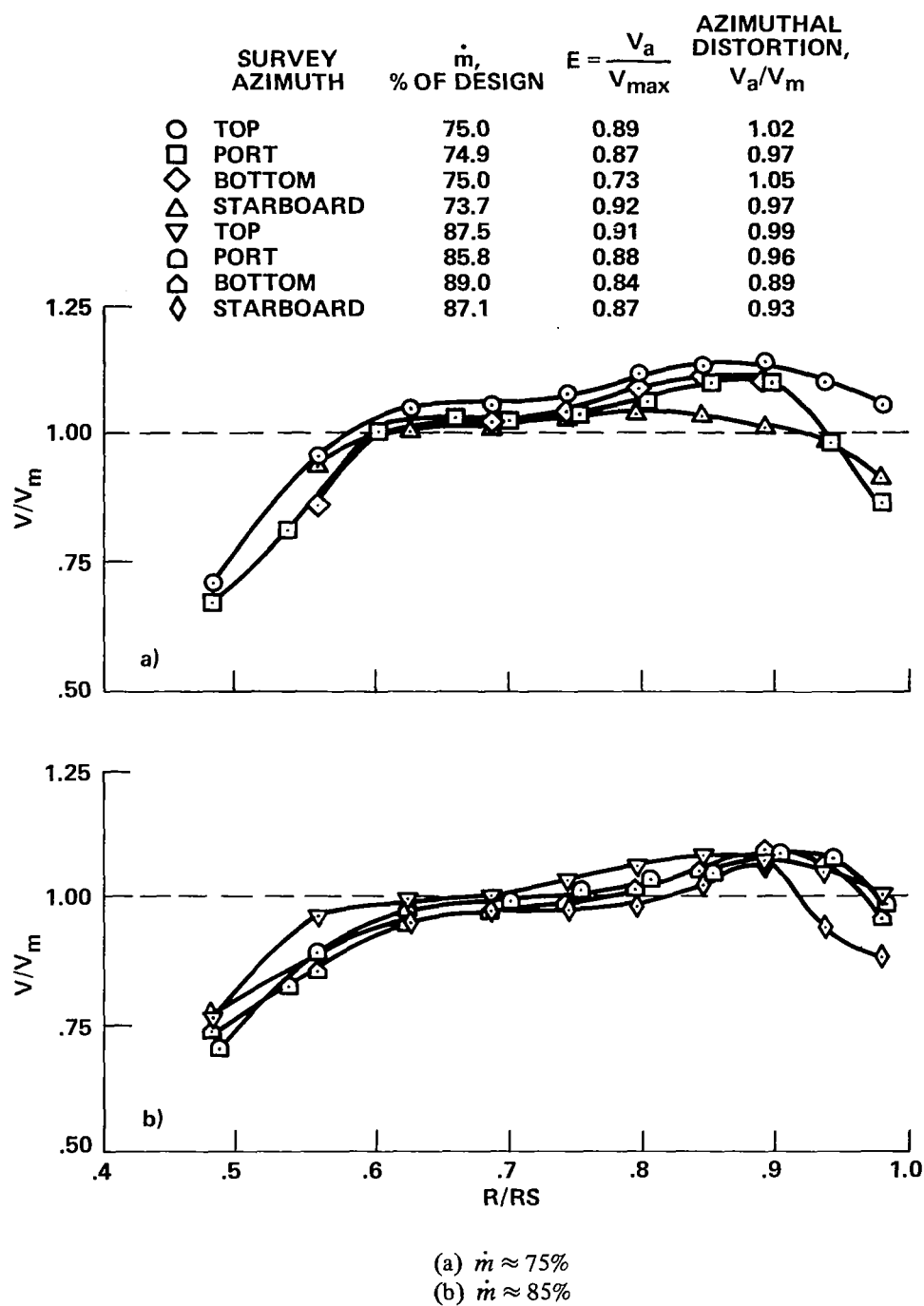


Figure 23.— Annulus velocity profiles for LVL configuration (see Notation and table 6) with $\xi = 43.2^\circ$ and no artificial azimuthal distortion.

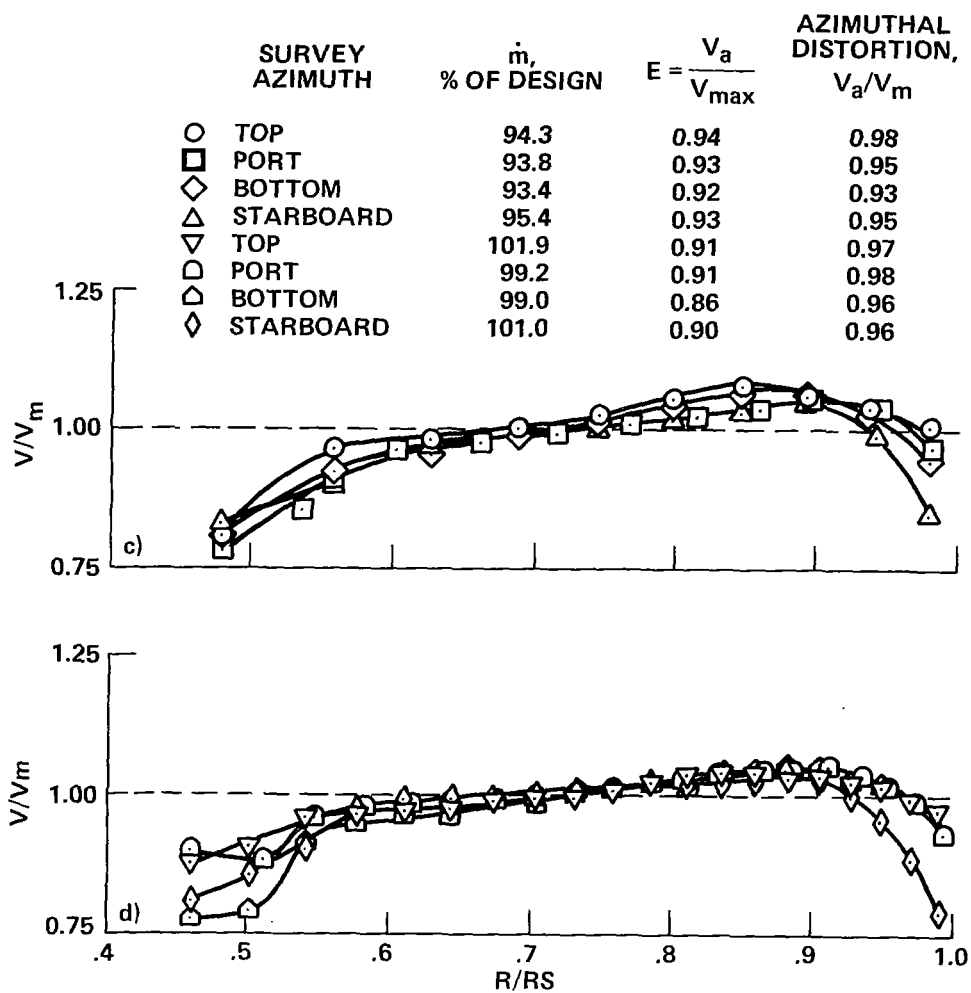
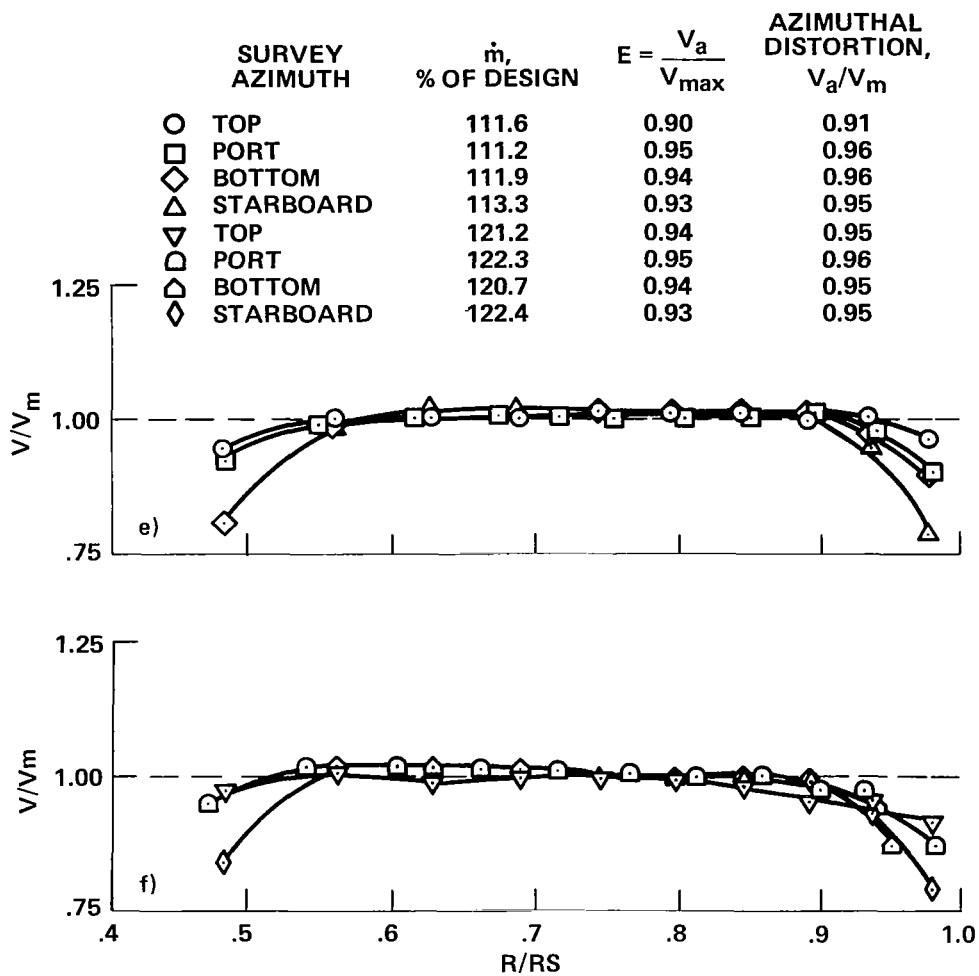


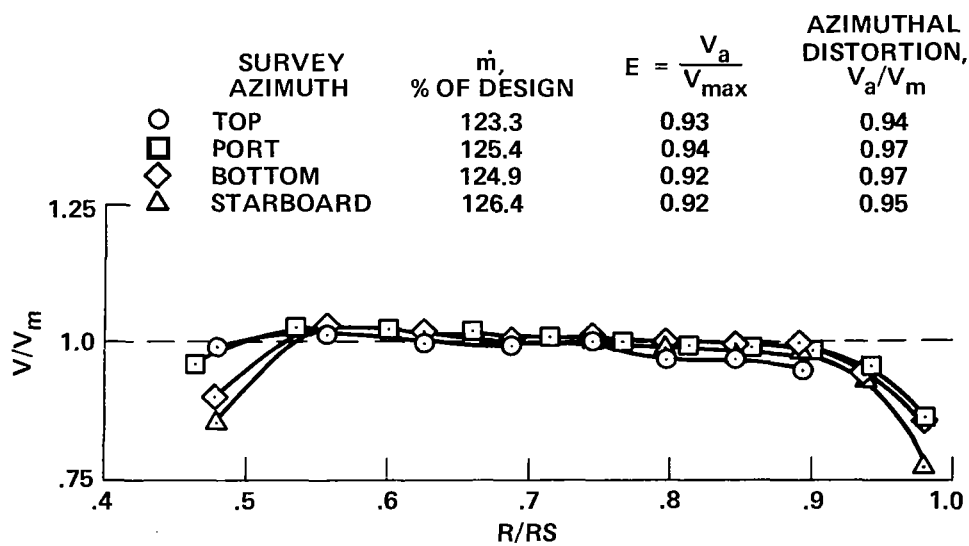
Figure 23.— Continued.



(e) $\dot{m} \approx 110\%$

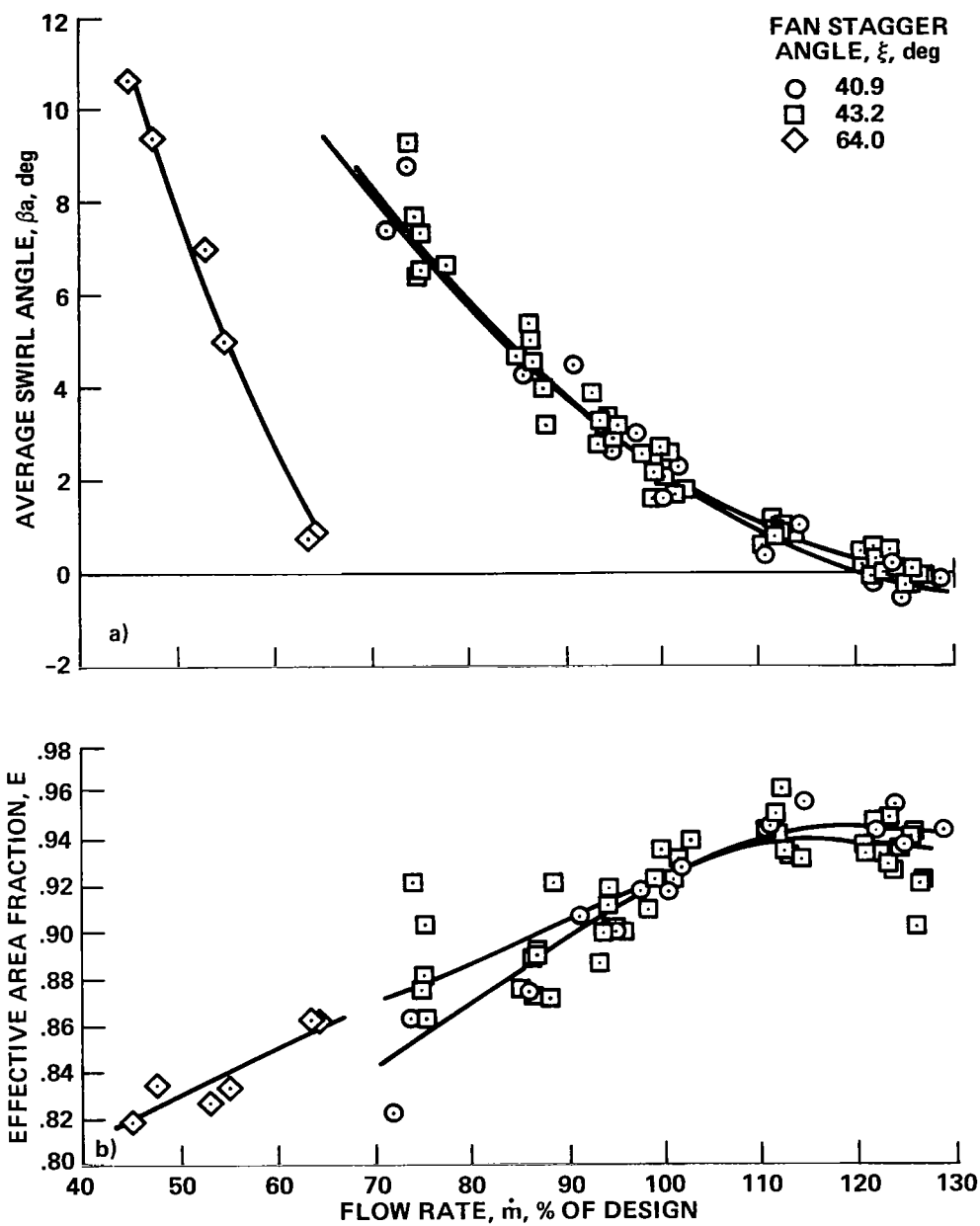
(f) $\dot{m} \approx 120\%$

Figure 23.— Continued.



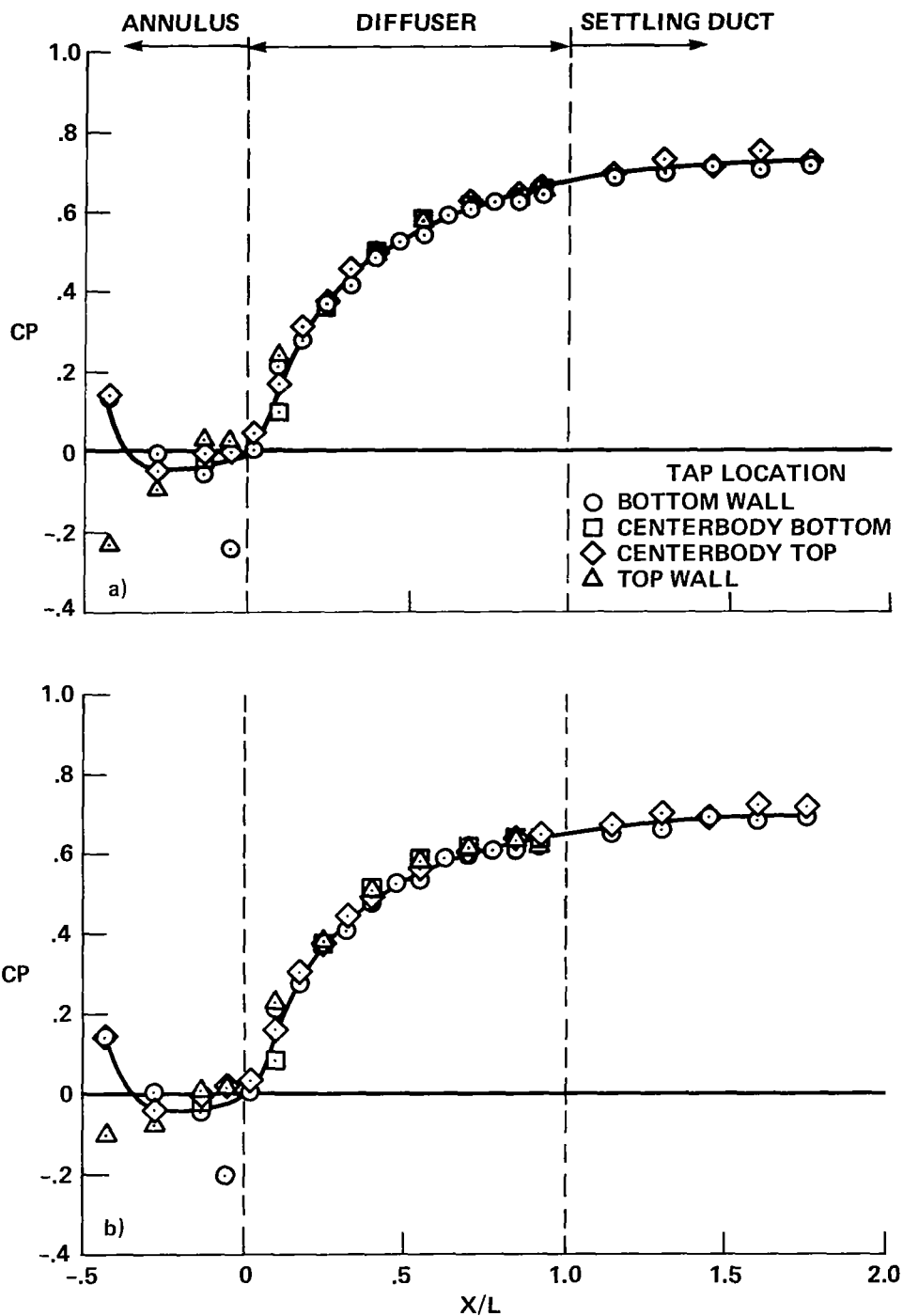
(g) $\dot{m} \approx 125\%$

Figure 23.— Concluded.



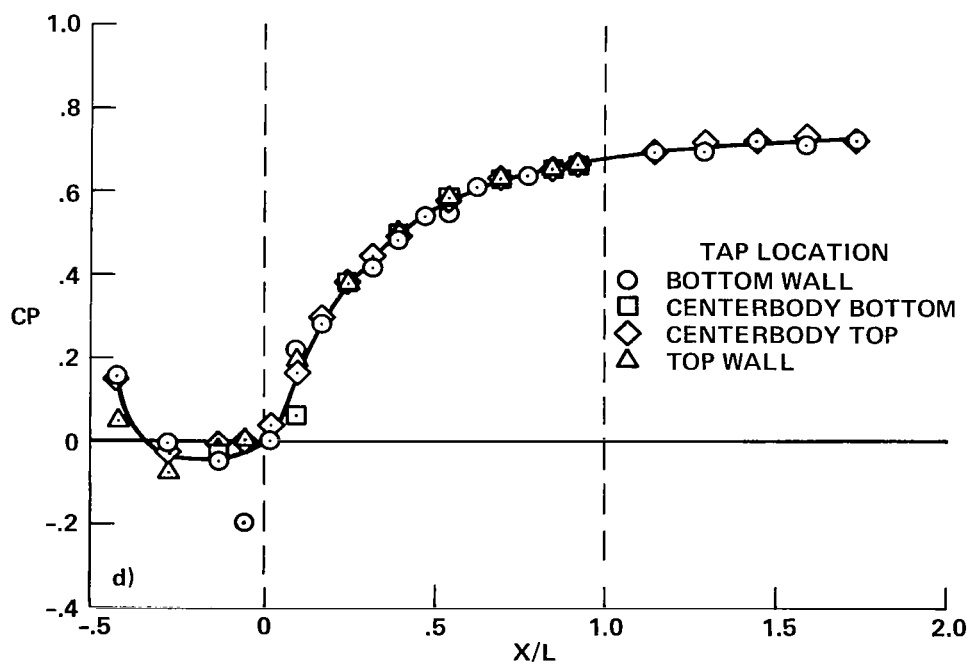
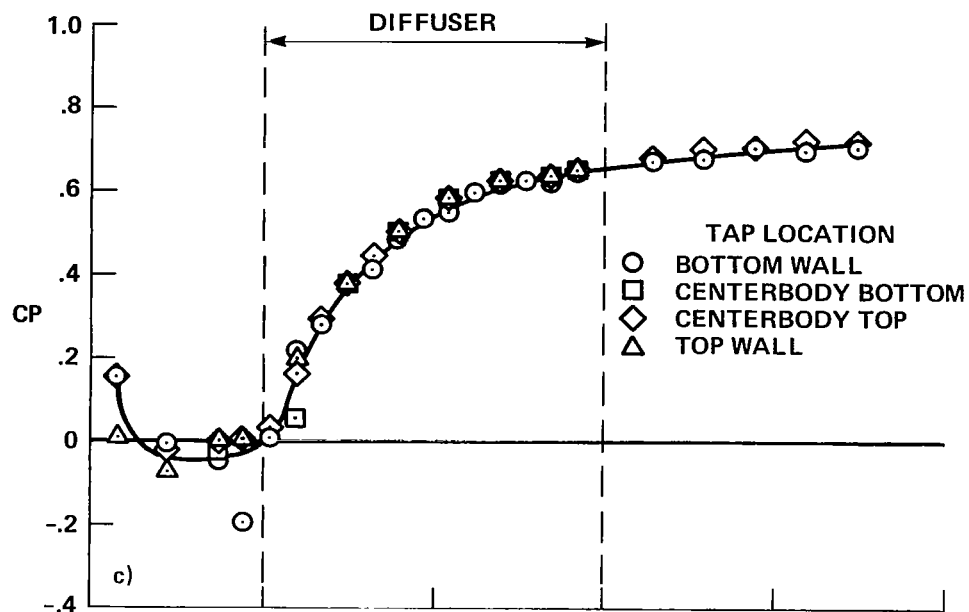
(a) Average swirl angle.
 (b) Effective area fraction.

Figure 24.— Annulus flow parameters for LVL configuration (see Notation and table 6) with no artificial azimuthal distortion.



(a) $\dot{m} \approx 75\%$
 (b) $\dot{m} \approx 85\%$

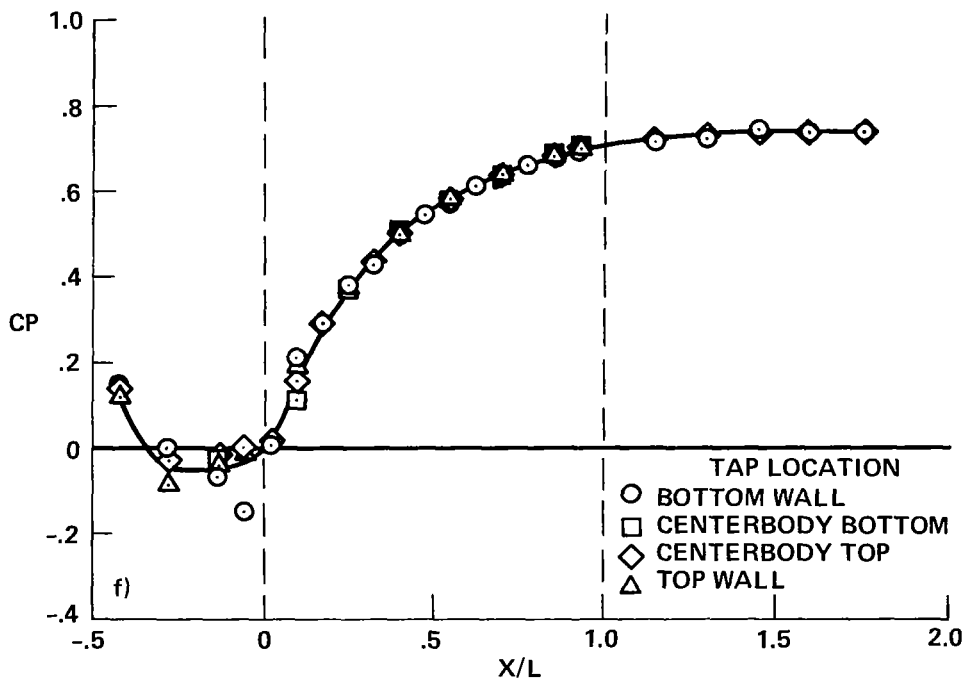
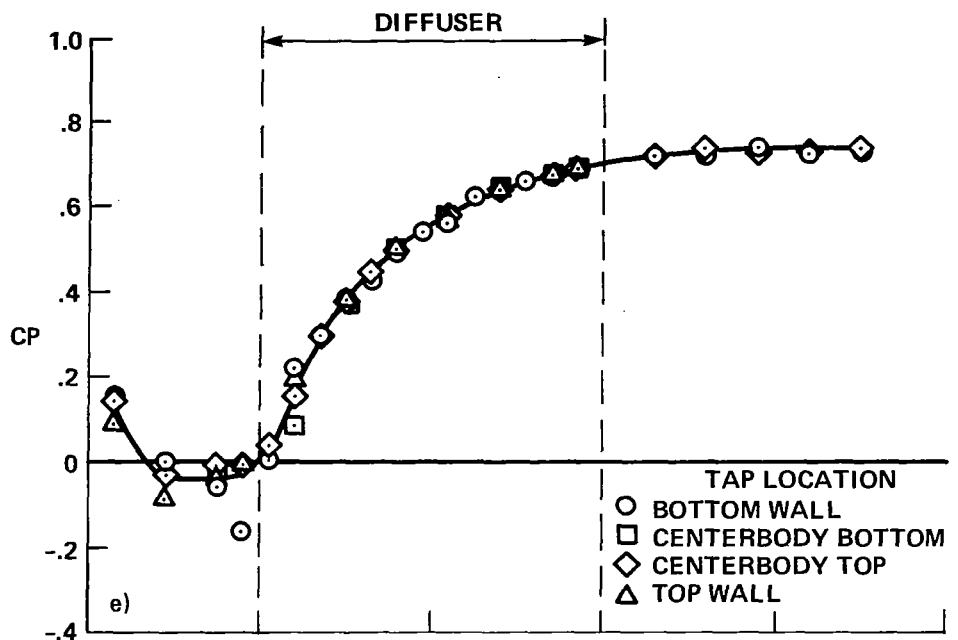
Figure 25.— Longitudinal distribution of static pressure coefficients for LVL configuration (see Notation and table 6) with $\xi = 43.2^\circ$ and no artificial azimuthal distortion.



(c) $\dot{m} \approx 95\%$

(d) $\dot{m} \approx 100\%$

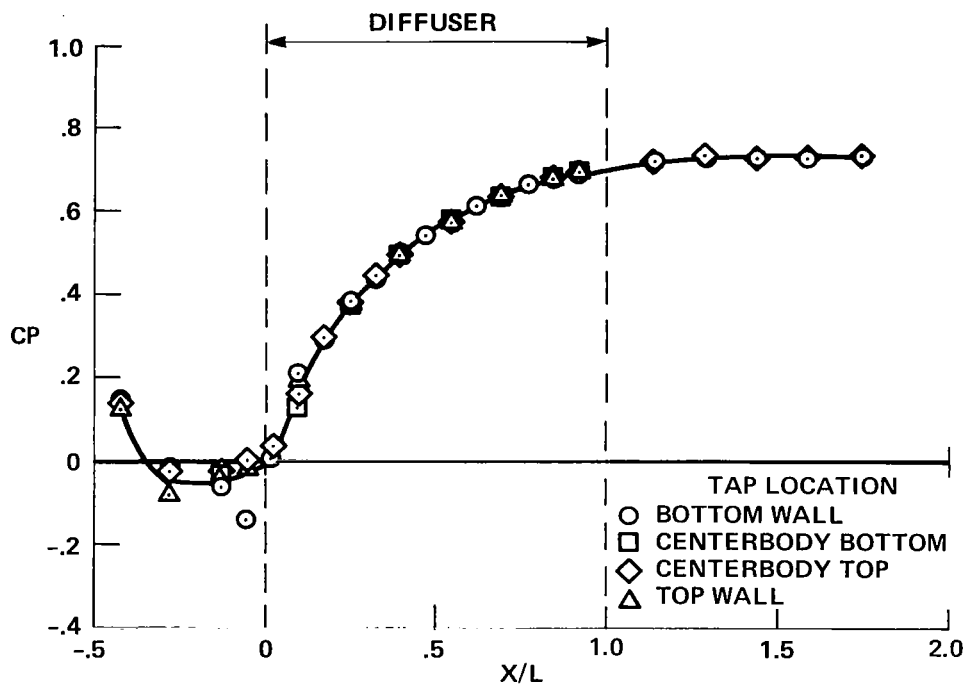
Figure 25.— Continued.



(e) $\dot{m} \approx 110\%$

(f) $\dot{m} \approx 120\%$

Figure 25.— Continued.



(g) $\dot{m} \approx 125\%$

Figure 25.— Concluded.

TOP				
PORT	*****			
	*			*
	*	1.261	1.488	1.363
	*			1.470
	*			*
	*			*
	*			*
	*	1.388	0.537	0.701
	*			1.528
	*			*
	*			*
	*	1.175	*****	*****
	*			1.281
	*			*
	*			*
	V/VM			
*			*	
*	1.172	0.231	0.360	
*			1.457	
*			*	
*			*	
*	1.337	0.944	0.659	
*			1.571	
*			*	
*			*	
*	1.433	1.468	1.513	
*			1.202	
*			*	

DECIMAL POINTS SHOW APPROXIMATE PROBE LOCATIONS				
NOTE: V/VM = ***** DENOTES REVERSE FLOW				

(a) $\dot{m} \approx 75\%$

Figure 26.— Velocity distribution, looking upstream, near diffuser exit plane for LVL configuration (see Notation and table 6) with $\xi = 43.2^\circ$ and no artificial azimuthal distortion.

TOP				
PORT	*	*	*	*
	*	1.300	1.452	1.505
	*			1.548
	*			
	*			
	*	1.515	0.660	0.763
	*			1.387
	*			
	*			
	*	1.104	*****	*****
	*			1.364
	*			
	*		V/VM	
	*	1.231	*****	*****
	*			1.291
	*			
	*	1.274	0.501	0.450
	*			1.481
	*			
	*			
	*	1.352	1.452	1.523
	*			1.394
	*			
	*			

DECIMAL POINTS SHOW APPROXIMATE PROBE LOCATIONS				
NOTE: V/VM = ***** DENOTES REVERSE FLOW				

(b) $\dot{m} \approx 85\%$

Figure 26.— Continued.

TOP				
PORT	*	*	*	*
	*	1.274	1.457	1.450
	*			1.374
	*			
	*			
	*	1.487	0.707	0.952
	*			1.453
	*			
	*			
	*	1.292	*****	*****
	*			1.297
	*			
	*		V/VM	
	*	1.331	*****	*****
	*			1.229
	*			
	*	1.303	0.661	0.811
	*			1.513
	*			
	*	1.205	1.474	1.474
	*			1.354
	*			
	*****	*****	*****	*****
DECIMAL POINTS SHOW APPROXIMATE PROBE LOCATIONS				
NOTE: V/VM = ***** DENOTES REVERSE FLOW				

(c) $\dot{m} \approx 95\%$

Figure 26.— Continued.

TOP				
PORT	*****	*****	*****	*****
	*			*
	*	1.283	1.408	1.395
	*			1.291
	*			*
	*			*
	*			*
	*	1.420	0.667	0.941
	*			1.418
	*			*
	*			*
	*	1.388	*****	*****
	*			1.230
	*			*
	*		V/VM	*
	*	1.355	*****	*****
	*			1.367
	*			*
	*			*
	*	1.334	0.793	0.882
	*			1.443
	*			*
	*			*
	*	1.069	1.443	1.433
	*			1.250
	*			*
	*			*
	*****	*****	*****	*****
DECIMAL POINTS SHOW APPROXIMATE PROBE LOCATIONS				
NOTE: V/VM = ***** DENOTES REVERSE FLOW				

(d) $\dot{m} \approx 100\%$

Figure 26.— Continued.

TOP				
PORT	*****			
	0.889	1.191	1.257	0.998
	1.205	1.094	1.171	1.378
	1.359	0.439	0.280	1.330
	V/VM			
	1.361	0.376	0.365	1.394
	1.235	1.250	1.122	1.387
0.780	1.304	1.127	0.991	

DECIMAL POINTS SHOW APPROXIMATE PROBE LOCATIONS				

(e) $\dot{m} \approx 110\%$

Figure 26.— Continued.

PORT	TOP			
	0.730	1.079	1.066	0.896
	1.173	1.364	1.419	1.365
	1.232	0.972	0.648	1.351
	V/VM			
	1.316	0.777	0.730	1.339
	1.119	1.399	1.366	1.354
	0.637	0.988	1.077	0.825
	DECIMAL POINTS SHOW APPROXIMATE PROBE LOCATIONS			

(f) $\dot{m} \approx 120\%$

Figure 26.— Continued.

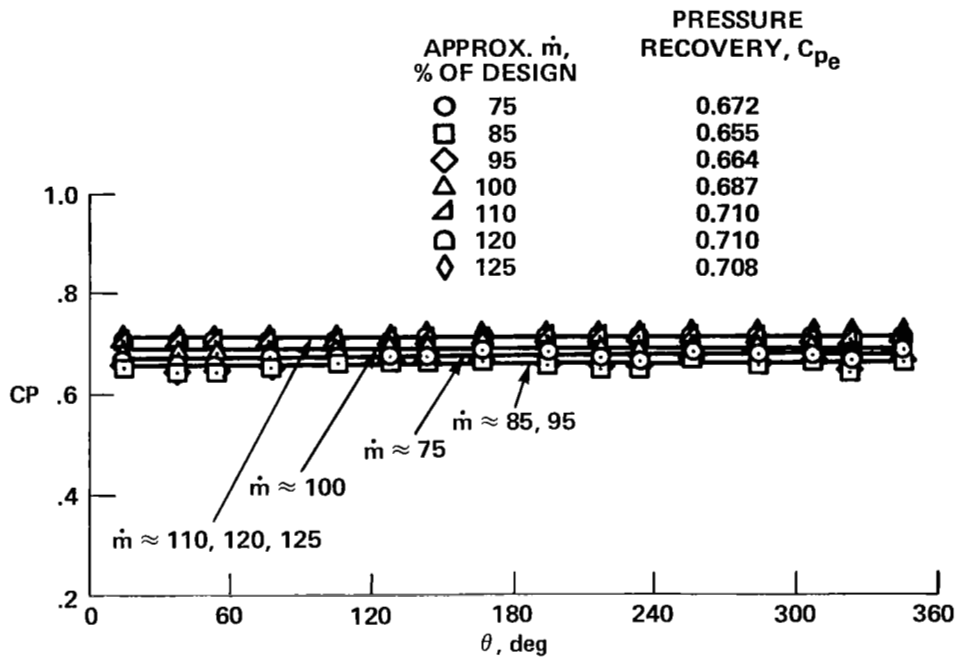
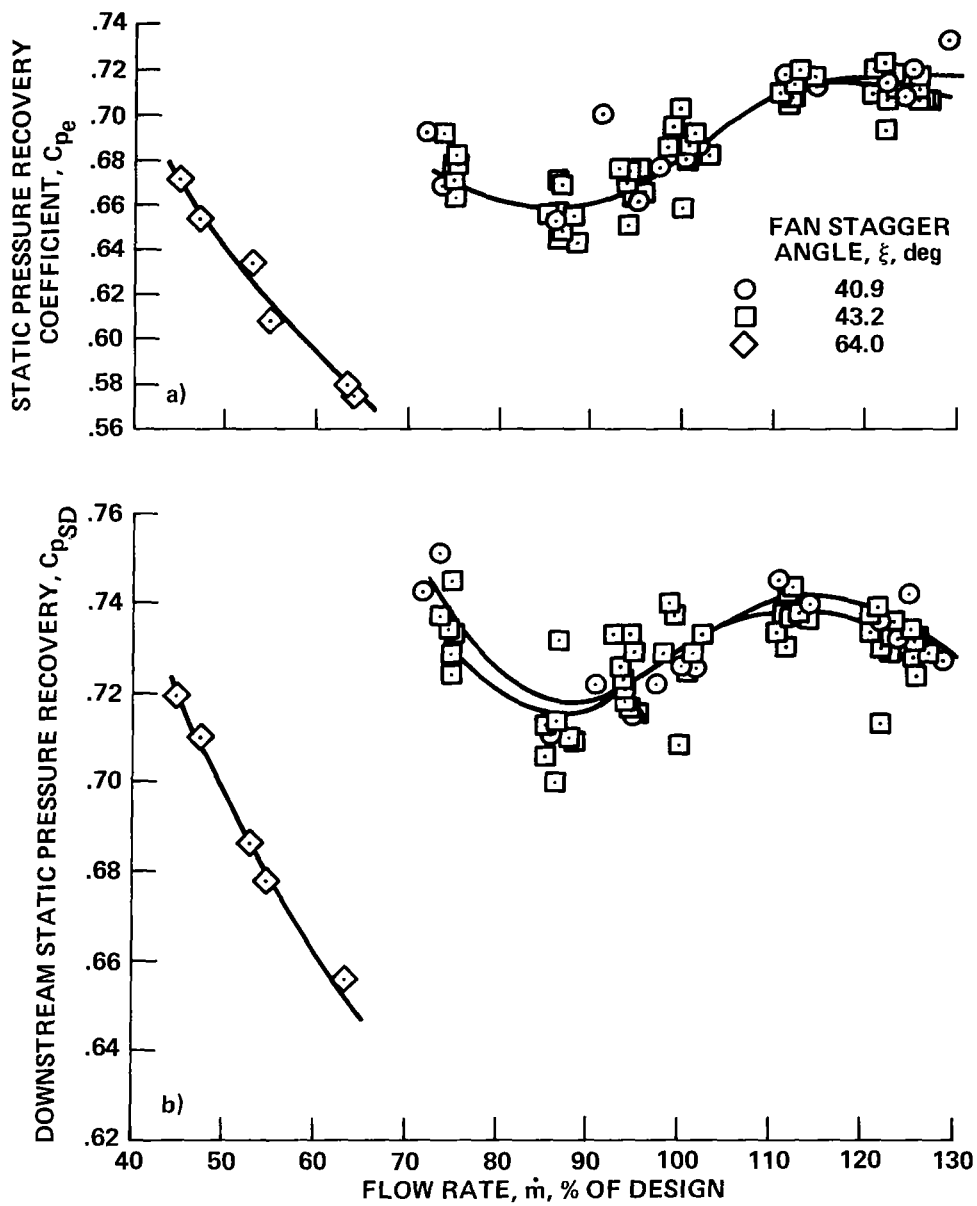
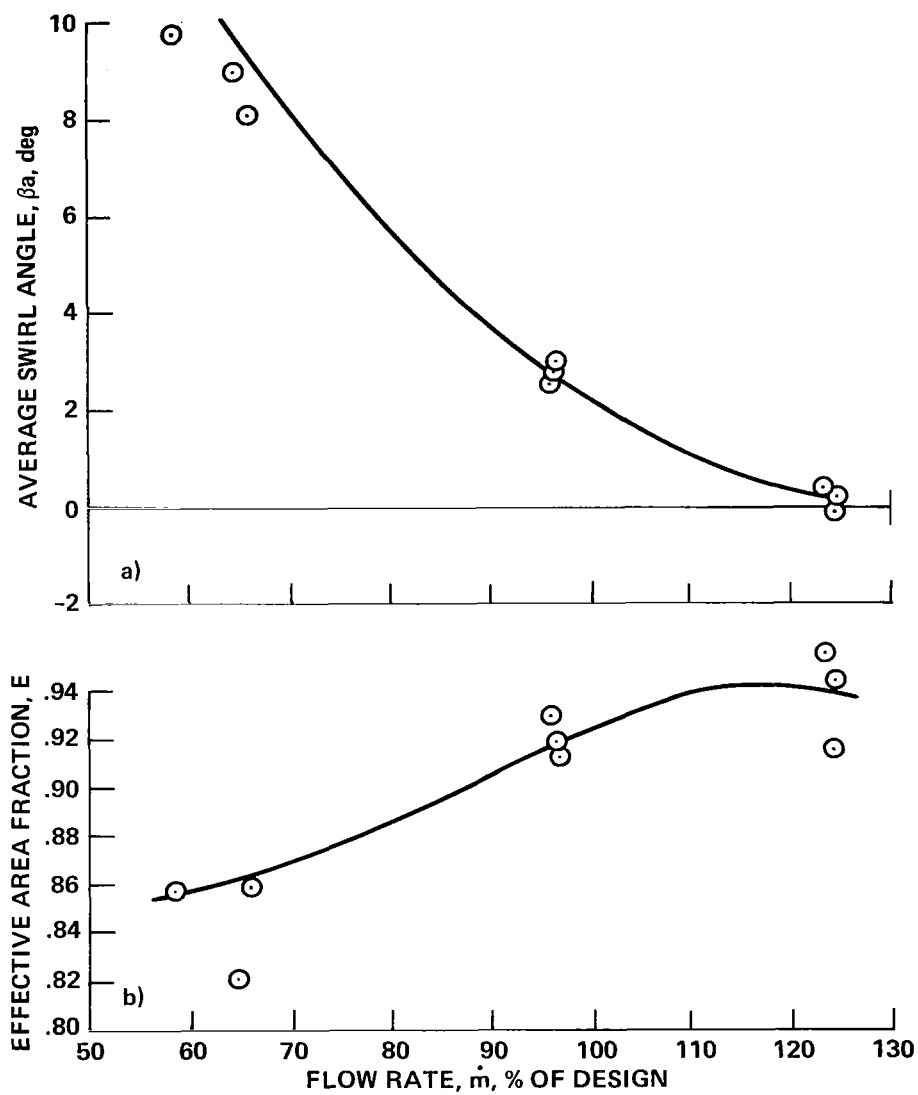


Figure 27.— Distribution of wall static pressure coefficients near diffuser exit plane for LVL configuration (see Notation and table 6) with $\xi = 43.2^\circ$ and no artificial azimuthal distortion.



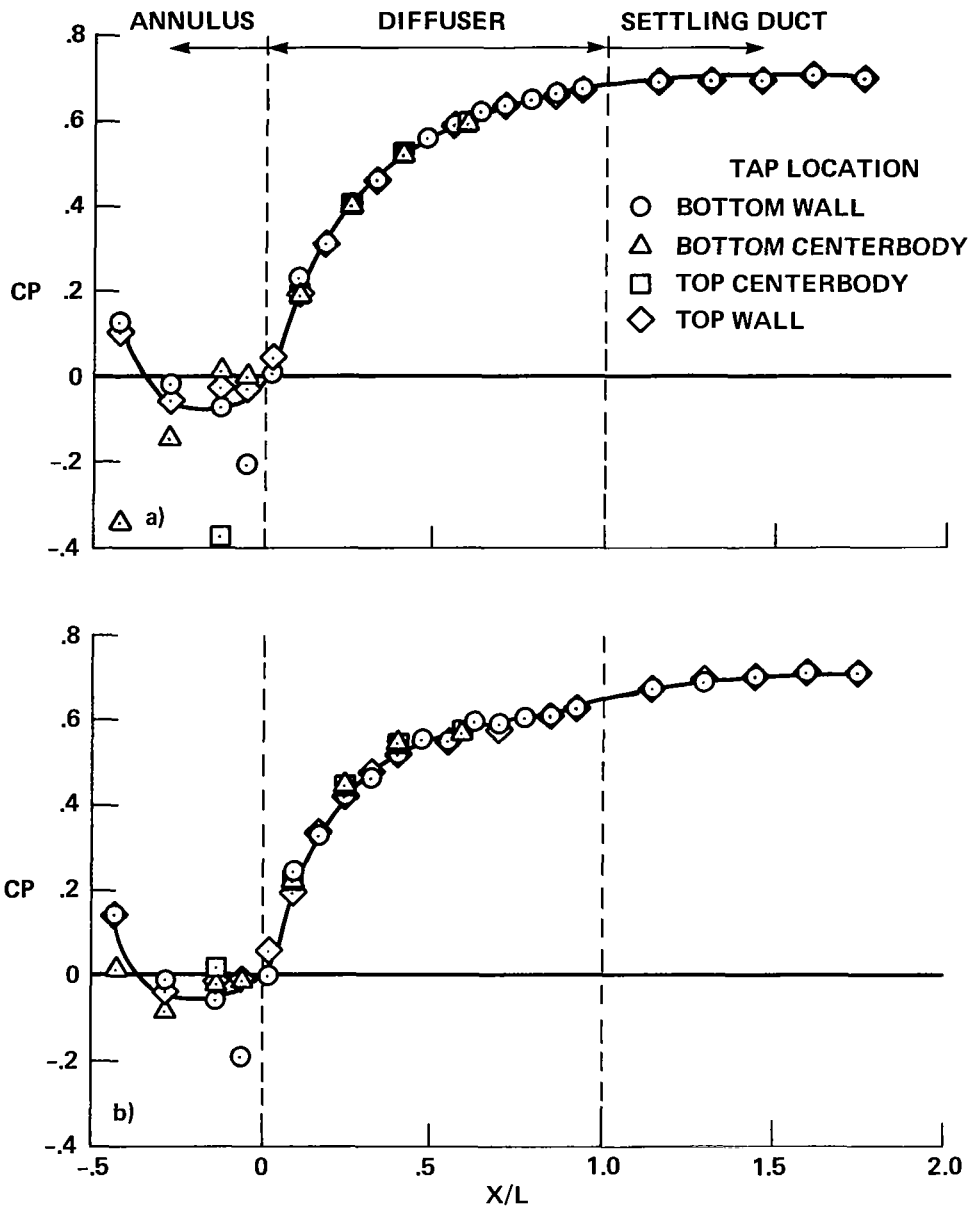
(a) Static pressure recovery coefficient near exit plane.
 (b) Static pressure recovery in settling duct.

Figure 28.— Diffuser performance for LVL configuration (see Notation and table 6) with no artificial azimuthal distortion.



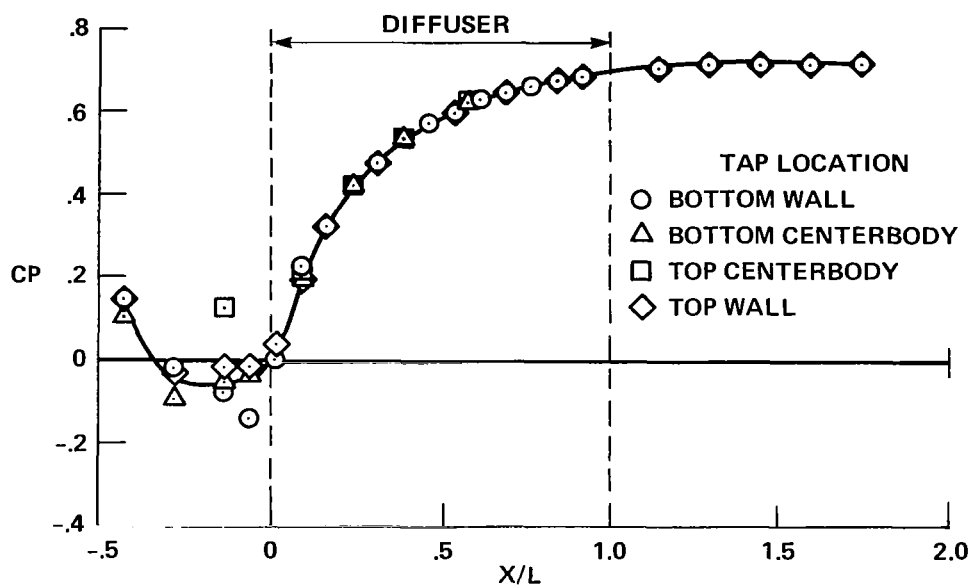
- (a) Average swirl angle.
 (b) Effective area fraction.

Figure 29.— Annulus flow parameters for LVS configuration (see Notation and table 6) with $\xi = 43.1^\circ$ and no artificial azimuthal distortion.



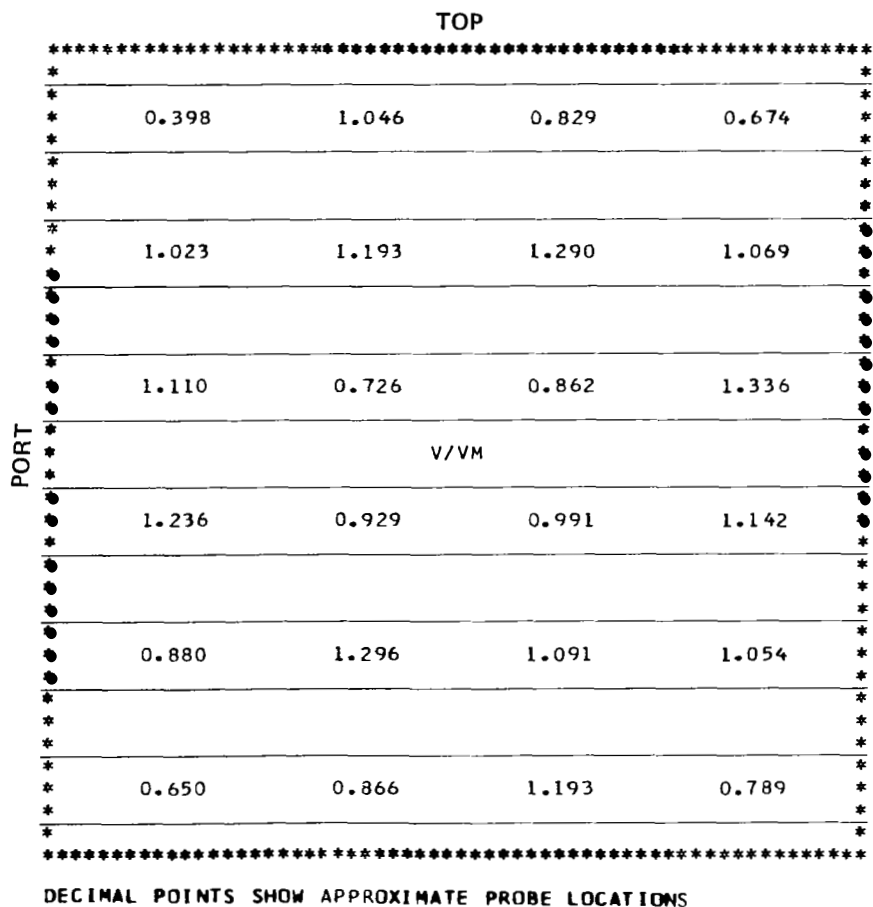
- (a) $\dot{m} \approx 65\%$
(b) $\dot{m} \approx 95\%$

Figure 30.— Longitudinal distribution of static pressure coefficient for LVS configuration (see Notation and table 6) with $\xi = 43.1^\circ$ and no artificial azimuthal distortion.



(c) $\dot{m} \approx 125\%$

Figure 30.— Concluded.



(a) $\dot{m} \approx 65\%$

Figure 31.— Velocity distribution, looking upstream, near diffuser exit plane for LVS configuration (see Notation and table 6) with $\xi = 43.1^\circ$ and no artificial azimuthal distortion.

		TOP			

PORT	*	*****			
	*	1.327	1.454	1.440	1.339
	*	*****			
	*	*****			
	*	1.496	0.620	0.928	1.474
	*	*****			
	*	1.323	0.110	*****	1.281
	*	*****			
	*	V/VM			
	*	1.346	*****	*****	1.381
	*	*****			
	*	1.261	0.598	0.661	1.473
	*	*****			
	*	1.015	1.441	1.453	1.276
	*	*****			

DECIMAL POINTS SHOW APPROXIMATE PROBE LOCATIONS
 NOTE: V/VM = ***** DENOTES REVERSE FLOW

(b) $\dot{m} \approx 95\%$

Figure 31.— Continued.

TOP				
PORT	0.632	0.984	1.003	0.797
	1.013	1.393	1.417	1.281
	1.123	1.085	0.829	1.272
	V/VM			
	1.053	0.658	0.720	1.293
	1.121	1.397	1.371	1.301
	0.478	0.807	1.026	0.580
	DECIMAL POINTS SHOW APPROXIMATE PROBE LOCATIONS			

(c) $\dot{m} \approx 125\%$

Figure 31.— Concluded.

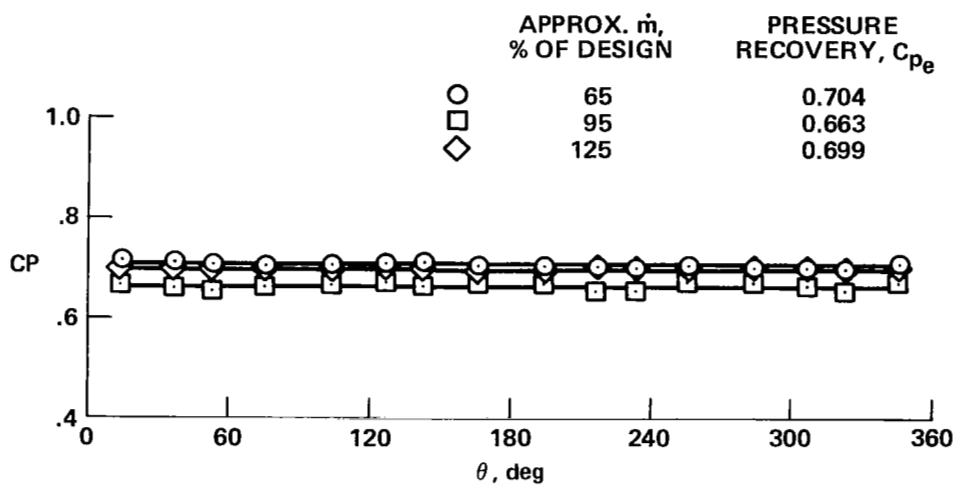
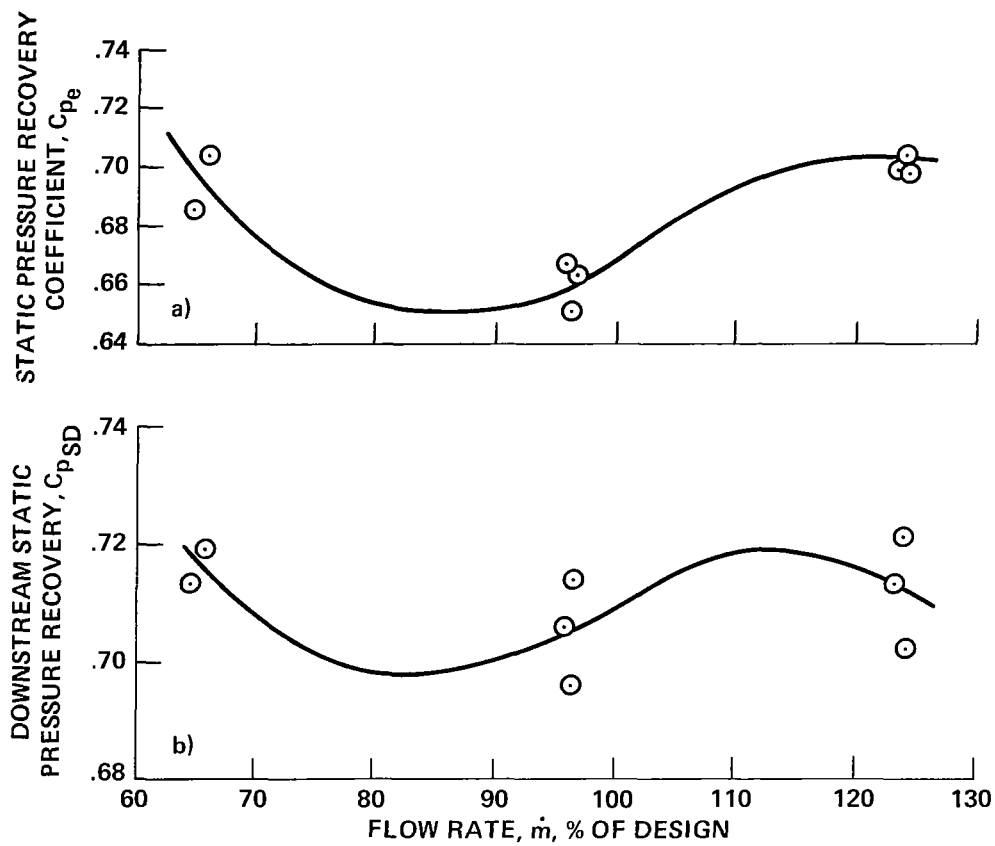
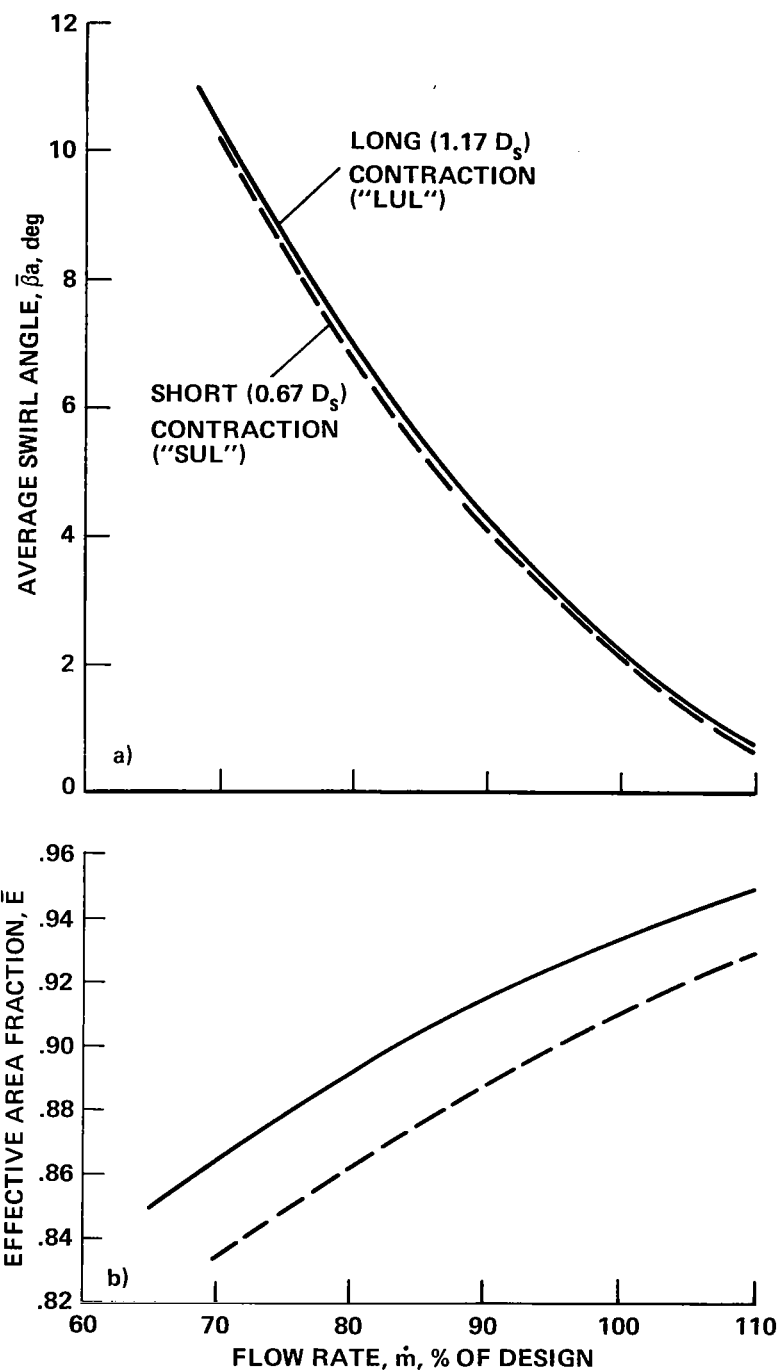


Figure 32.— Distribution of wall static pressure coefficients near diffuser exit plane for LVS configuration (see Notation and table 6) with $\xi = 43.1^\circ$ and no artificial azimuthal distortion.



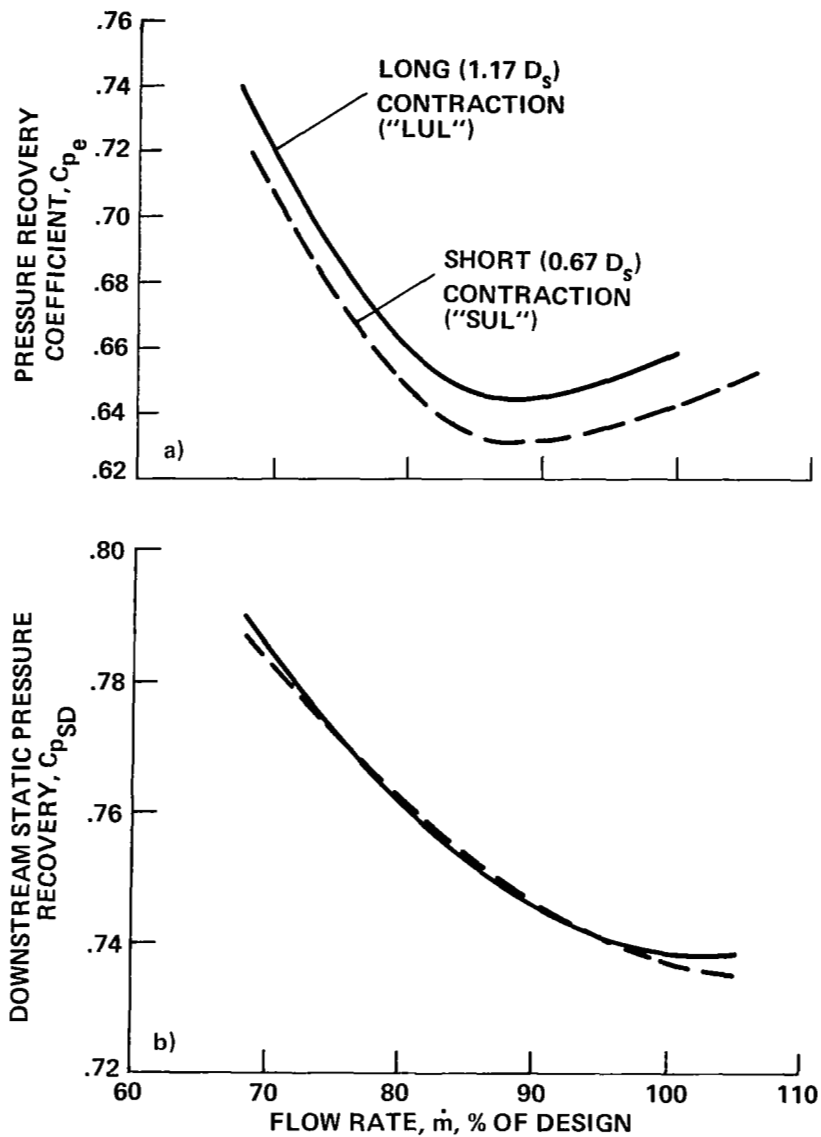
- (a) Static pressure recovery coefficient near exit plane.
 (b) Static pressure recovery in settling duct.

Figure 33.— Diffuser performance for LVS configuration (see Notation and table 6) with $\xi = 43.1^\circ$ and no artificial azimuthal distortion.



- (a) Average inflow swirl angle.
 (b) Average inflow effective area fraction.

Figure 34.— Effect of contraction geometry on annulus flow parameters for $\xi = 40.8^\circ$ and no artificial azimuthal distortion.



- (a) Static pressure recovery coefficient near exit plane.
 (b) Static pressure recovery in settling duct.

Figure 35.— Effect of contraction geometry on diffuser performance for $\xi = 40.8^\circ$ and no artificial azimuthal distortion.

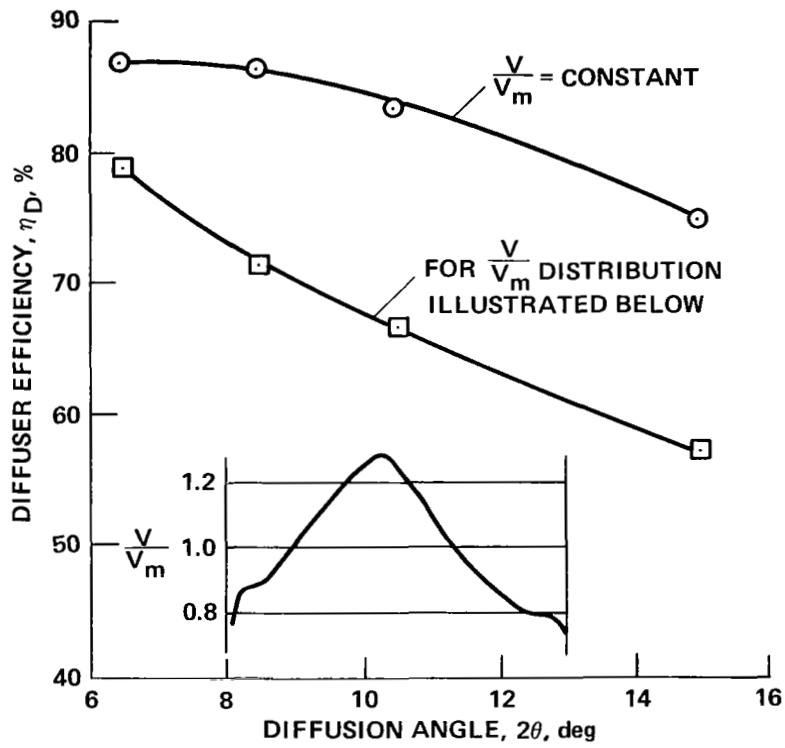


Figure 36.— Effect of radial distortion of inflow on annular diffuser efficiency (taken from fig. 2 of ref. 13).

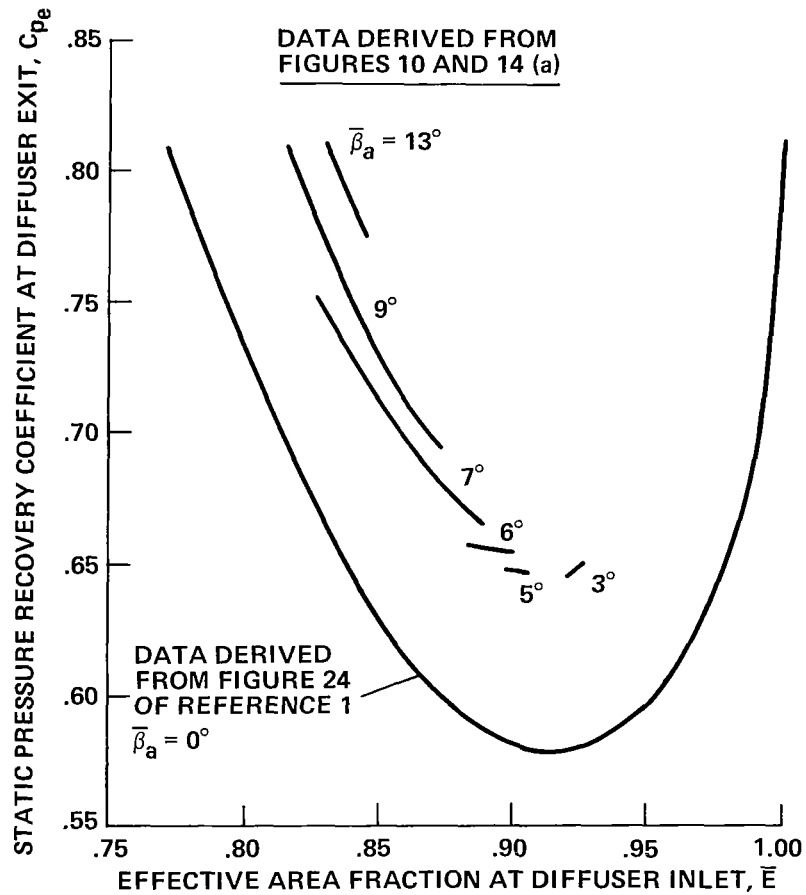


Figure 37.— Variation of static pressure recovery with area fraction at constant swirl angles for current LUL configuration (see Notation and table 7) with no artificial azimuthal distortion (from fig. 24 of ref. 1).

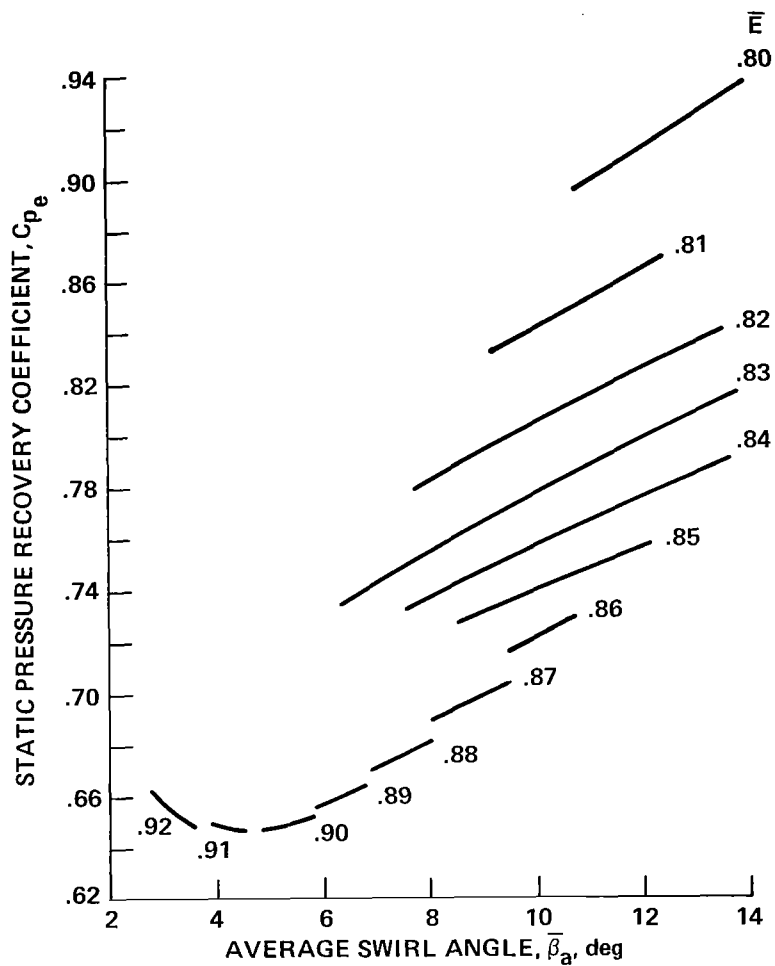
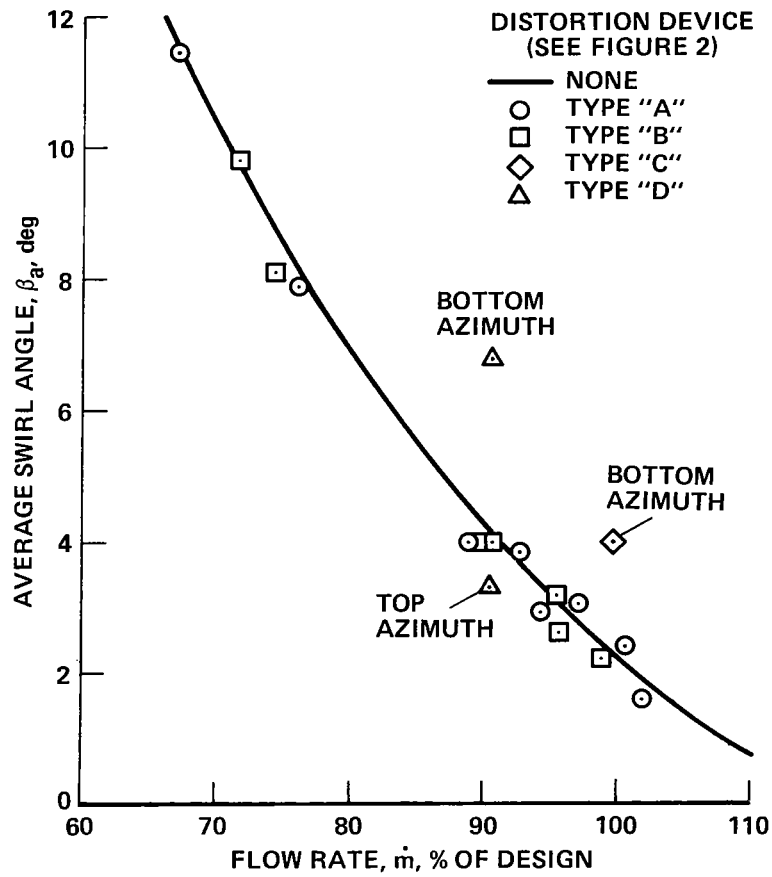
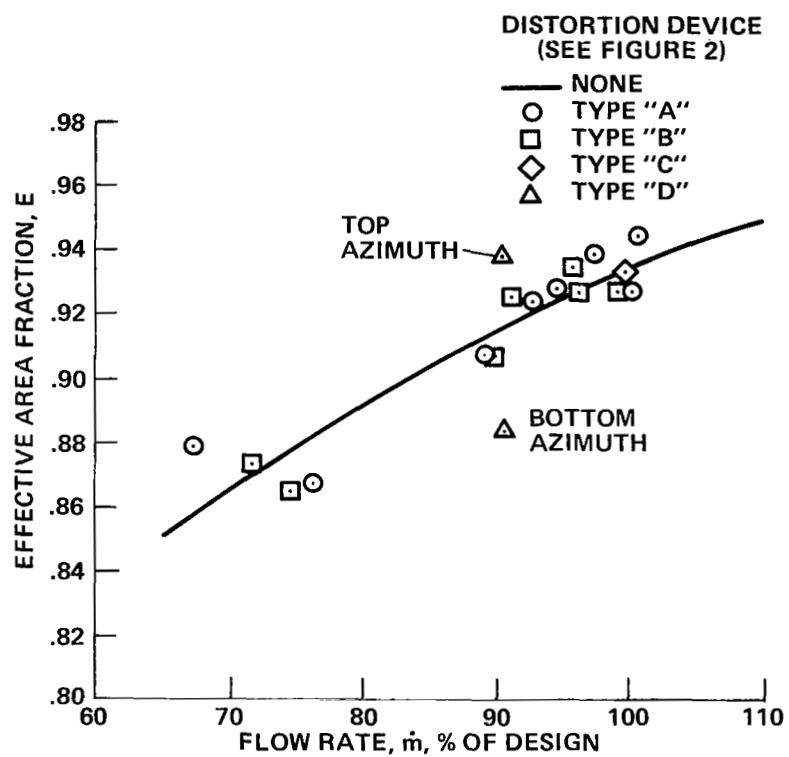


Figure 38.— Variation of static pressure recovery with swirl angle at constant area fraction for LUL configuration (see Notation and table 7) with no artificial azimuthal distortion.



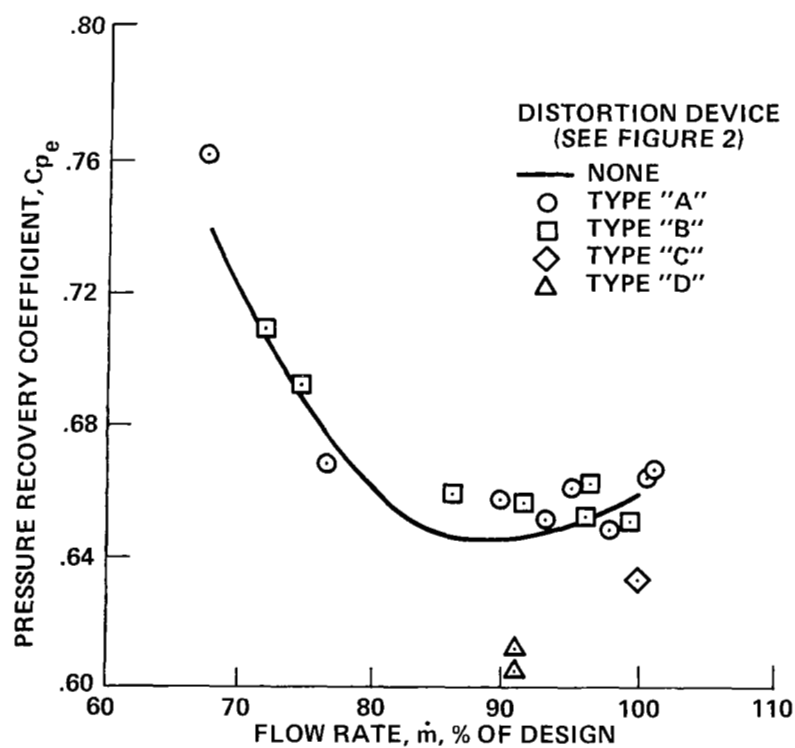
(a) Average swirl angle.

Figure 39.— Effect of distortion on annulus flow parameters for LUL configuration (see Notation and table 7) with $\xi = 40.8^\circ$.



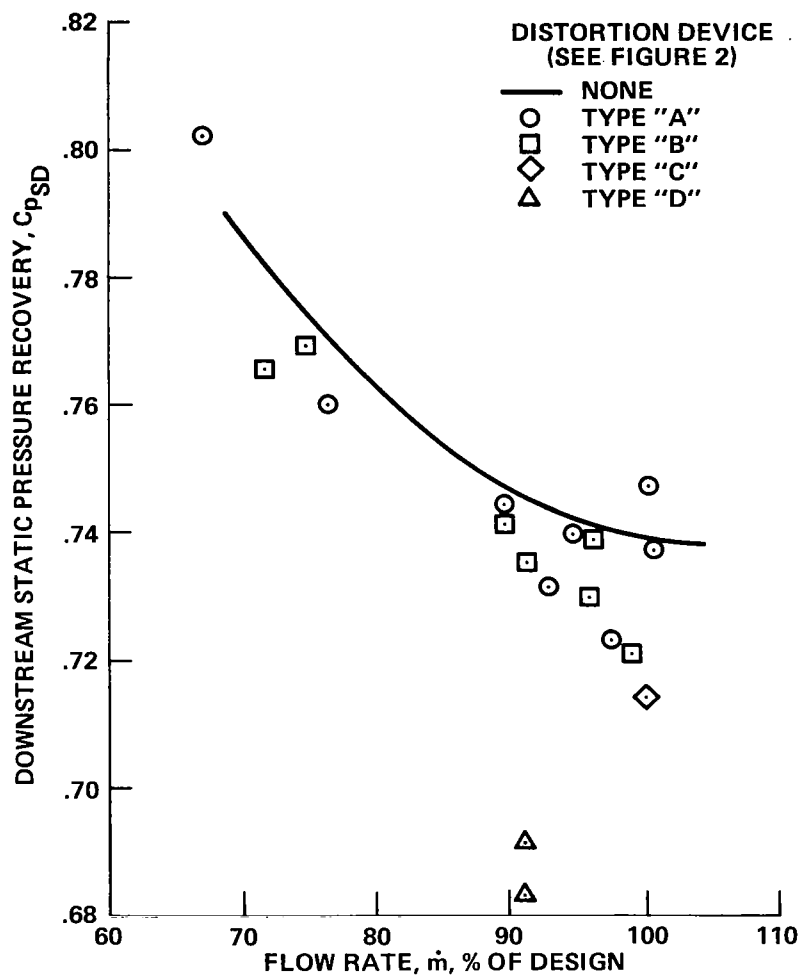
(b) Average inflow effective area fraction.

Figure 39.— Concluded.



(a) Static pressure recovery coefficient near exit plane.

Figure 40.— Effect of distortion on diffuser performance for LUL configuration (see Notation and table 7) with $\xi = 40.8^\circ$.



(b) Static pressure recovery in settling duct.

Figure 40.— Concluded.

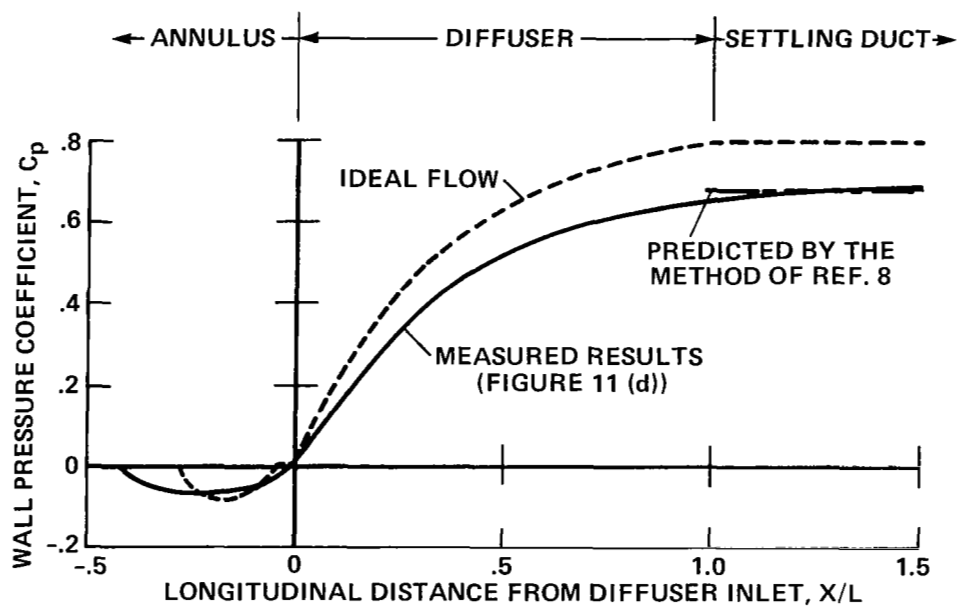
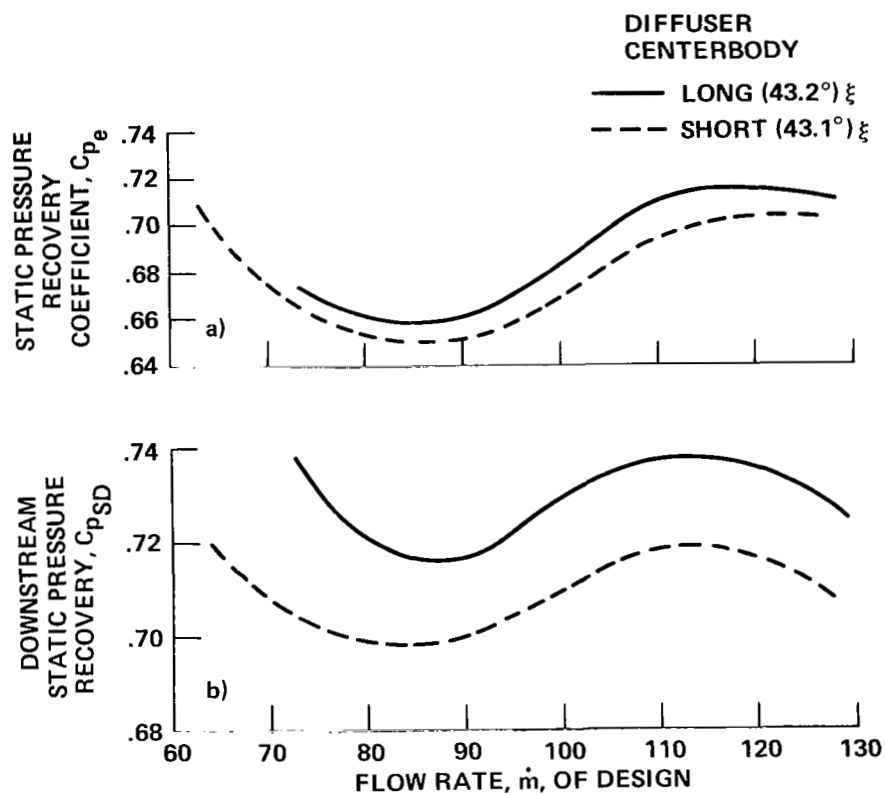


Figure 41.— Comparison of simple theories with experimentally achieved longitudinal distribution of wall static pressure coefficient.



- (a) Static pressure recovery coefficient near exit plane.
 (b) Static pressure recovery in settling duct.

Figure 42.— Effect of diffuser centerbody length on diffuser performance for LVX configurations (see Notation and table 7) with no artificial azimuthal distortion.

1. Report No. NASA TP-1628 AVRADCOM Tech. Rep. 79-40		2. Government Accession No.		3. Recipient's Catalog No.	
4. Title and Subtitle AN EXPERIMENTAL INVESTIGATION OF TWO LARGE ANNULAR DIFFUSERS WITH SWIRLING AND DISTORTED INFLOW				5. Report Date February 1980	
				6. Performing Organization Code	
7. Author(s) William T. Eckert,* James P. Johnston,† Tad D. Simons,† Kenneth W. Mort,‡ and V. Robert Page‡				8. Performing Organization Report No. A-7436	
				10. Work Unit No. 505-31-3	
9. Performing Organization Name and Address *AVRADCOM Research and Technology Laboratories, Moffett Field, CA 94035 †Mechanical Engineering Dept., Stanford University, Stanford, CA 94305 ‡NASA Ames Research Center, Moffett Field, CA 94035				11. Contract or Grant No.	
				13. Type of Report and Period Covered Technical Paper	
12. Sponsoring Agency Name and Address National Aeronautics and Space Administration, Washington, D.C. 20546 and U.S. Army Aviation Research and Development Command St. Louis, Missouri 93166				14. Sponsoring Agency Code	
15. Supplementary Notes					
16. Abstract <p>Two annular diffusers downstream of a nacelle-mounted fan were tested for aerodynamic performance, measured in terms of two static pressure recovery parameters (one near the diffuser exit plane and one about three diameters downstream in the settling duct) in the presence of several inflow conditions. The two diffusers each had an inlet diameter of 1.84 m, an area ratio of 2.3, and an equivalent cone angle of 11.5°, but were distinguished by centerbodies of different lengths. The dependence of diffuser performance on various combinations of swirling, radially distorted, and/or azimuthally distorted inflow was examined. Swirling flow and distortions in the axial velocity profile in the annulus upstream of the diffuser inlet were caused by the intrinsic flow patterns downstream of a fan in a duct and by artificial intensification of the distortions. Azimuthal distortions or defects were generated by the addition of four artificial devices (screens and fences).</p> <p>Pressure recovery data indicated beneficial effects of both radial distortion (for a limited range of distortion levels) and inflow swirl. Small amounts of azimuthal distortion created by the artificial devices produced only small effects on diffuser performance. A large artificial distortion device was required to produce enough azimuthal flow distortion to significantly degrade the diffuser static pressure recovery.</p>					
17. Key Words (Suggested by Author(s)) Diffuser Swirl Distortion Annulus Nacelle			18. Distribution Statement Unlimited STAR Category - 02		
19. Security Classif. (of this report) Unclassified		20. Security Classif. (of this page) Unclassified		21. No. of Pages 104	
				22. Price* \$6.50	

National Aeronautics and
Space Administration

THIRD-CLASS BULK RATE

Postage and Fees Paid
National Aeronautics and
Space Administration
NASA-451



Washington, D.C.
20546

Official Business

Penalty for Private Use, \$300

8 1 10, A, 020880 S00903DS
DEPT OF THE AIR FORCE
AF WEAPONS LABORATORY
ATTN: TECHNICAL LIBRARY (SUL)
KIRTLAND AFB NM 87117

S

NASA

POSTMASTER: If Undeliverable (Section 158
Postal Manual) Do Not Return